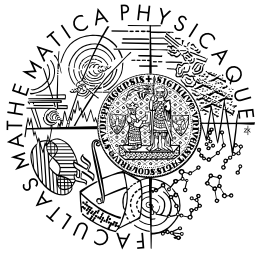

FACULTY
OF MATHEMATICS
AND PHYSICS
Charles University

MASTER THESIS

Jan Jerhot

Search for Axion-Like Particles at the NA62 experiment

Institute of Particle and Nuclear Physics

Supervisor of the master thesis: doc. RNDr. Karol Kampf, Ph.D.
Co-supervisor: Mgr. Michal Zamkovský
Study programme: Physics
Study branch: Nuclear and Subnuclear Physics

Prague 2019

I declare that I carried out this master thesis independently, and only with the cited sources, literature and other professional sources.

I understand that my work relates to the rights and obligations under the Act No. 121/2000 Sb., the Copyright Act, as amended, in particular the fact that the Charles University has the right to conclude a license agreement on the use of this work as a school work pursuant to Section 60 subsection 1 of the Copyright Act.

In ..... date ..... signature of the author

At the first place I would like to thank here my family and friends for their immense support as without them none of this was ever possible.

My sincere gratitude goes to Karol Kampf and Michal Zamkovský for giving me the opportunity to join the NA62 Collaboration and to study this particular topic and especially I would like thank Babette Döbrich and Tommaso Spadaro for guiding me through the work with beam-dump data. I also want to thank my colleagues at NA62 for the huge amount of work they have done and many helpful recommendations.

Last but not least I want to thank my colleagues at IPNP for sharing their positive drive as well as for inspiring discussions over a cup of coffee.

Title: Search for Axion-Like Particles at the NA62 experiment

Author: Jan Jerhot

Institute: Institute of Particle and Nuclear Physics

Supervisor: doc. RNDr. Karol Kampf, Ph.D., Institute of Particle and Nuclear Physics

Co-supervisor: Mgr. Michal Zamkovský, Institute of Particle and Nuclear Physics

Abstract: The thesis instructively presents axions and axion-like particles as a plausible extension of the Standard Model of particle physics and discusses also the cosmological implications in the case of their existence as they present one of the most favourable dark matter candidates at given circumstances. The main part of the thesis is concerned with a search for axion-like particles at the NA62 experiment at CERN and a study of the gathered data and its impact on the data analysis.

Keywords: SM QCD Axion ALP NA62

Contents

Introduction

Axion-like particles appear in many theories beyond the Standard Model of particle physics as a consequence of a spontaneous symmetry breaking of an axial $U(1)$ symmetry. They are pseudoscalar particles sharing common properties with axions, which were originally predicted in 1977 in order to explain the Strong CP problem of quantum chromodynamics but as of yet have not been observed. Thanks to their theoretical properties axion-like particles present a serious candidate for the dark matter particle in a case they are very weakly coupled to the observed matter, which gives a rise to a plenitude of techniques how to measure the impacts of their possible existence.

Current technologies allow to search for axion-like particles with an exceptional sensitivity in a cost-effective manner and hence many new experiments are proposed in the near-future. Another option to search for axion-like particles is to use existing experiments like is the case of collider beam-dump facilities, which can access regions of masses of potential axion-like particles inaccessible by other techniques. In most of the cases the beam-dump measurements can take place complementary to a differently motivated physics programme as is the case of the NA62 experiment at CERN.

While the NA62 experiment serves primarily as a 'kaon factory' for a test of the Standard Model, estimations show that already with one day of the data-taking in the beam-dump mode, it accesses unexplored areas in the axion-like particle parameter space. A sufficient statistics of data in the beam-dump mode was gathered during the 2016-2018 data-taking period, which has to be analyzed and also studied in terms of data quality in order to allow even more efficient research in the future data-taking.

0. Outline

The thesis consists of three main parts, presenting the theoretical and experimental motivation and a study of real data. An undergraduate level of knowledge of quantum field theory is expected from the reader, but any other reader is welcome as most of the topics discussed are at least briefly introduced either in the text or in the appendices. A more detailed description or an exhaustive literature is usually referenced throughout the text.

0.1 Theory

The theoretical part is found in chapters 1 and 2, where the first one introduces the Standard Model of particle physics as a gauge field theory and heads towards the quantum chromodynamics (QCD). The axial $U(1)$ problem of QCD is presented and eliminated by the forced axial symmetry breaking due to a non-trivial theta-vacuum topology, which however elevates the Strong-CP problem.

A solution of the Strong-CP problem using the Peccei-Quinn mechanism and an introduction of axions is presented in the second chapter. A phenomenological section with a generalization to Axion-Like Particles (ALPs), which presents the central motivation for the thesis, follows together with a brief summary of ALP models, ALP couplings to the SM and implications for the cosmology.

0.2 Experiment

The experimental part is concerned with a summary of distinct experimental searches and current limits on ALP invariant masses, couplings and current coverage of the parameter space with an emphasis on beam-dump (BD) experiments provided in the chapter 3.

Further the experimental layout of the fixed-target NA62 experiment at CERN is discussed[1] in the chapter 4. The trigger setup described in the chapter 5 contains slightly more technical details. This is necessary in order to explain technical difficulties found in the analysis.

0.3 Data analysis

The last part of the thesis discusses the event reconstruction within the NA62 Framework (NA62FW) and necessary corrections in the chapter 6. The possibility of running the experiment under special data taking conditions (beam-dump mode) and review of gathered data are described in the chapter 7 together with the estimated sensitivity by Monte Carlo (MC) simulations. The study of gathered data (trigger efficiency) in BD mode in the chapter 8 is followed by a test

[1] Chapters 4 and 5 present an extended and updated version of chapters [2] and [3] of the bachelor thesis [1].

of the data quality with a 'known physics' in the standard data-taking mode in the chapter 9. Finally. the last chapter 10 deals with a $ALP \to \gamma\gamma$ analysis of the beam-dump data samples taken during runs from years 2016-2018.

The analysis is performed using ROOT (object-oriented data analysis framework) [2] together with NA62 Framework libraries [3] which have been in development since 2014. Since a lot of parameters from various detectors in the experiment have to be taken into account, machine learning techniques are used e.g. for particle identification. The machine learning is implemented using the Toolkit for Multivariate Data Analysis (TMVA) for ROOT [4].

1. Gauge field theories

Since the thesis aims at physics beyond the Standard Model (SM) of particle physics, it is convenient to briefly present the SM together with its technical base before dealing with some of the issues regarding the SM by its extension.

1.1 Standard Model

The Standard Model is a quantum field theory with a local gauge symmetry[1] $SU(3)_C \times SU(2)_L \times U(1)_Y$ and describes elementary particles and interactions among them (except for gravity). Thanks to its immense predictive precision, it has stayed in the center of attention throughout the scientific community for more than forty years. The organisation of the SM in terms of physical observables (particles) can be shown in a popular periodic table of elementary particles. Particles corresponding to spinor fields, (carrying spin 1/2) are subdivided to quarks and leptons (see table 1.1) depending on the corresponding gauge symmetry group.

	1^{st}gen	2^{nd}gen	3^{rd}gen	e
quarks	u	c	t	$2/3$
	d	s	b	$-1/3$
leptons	e	μ	τ	-1
	ν_e	ν_μ	ν_τ	0

Table 1.1: Fermions and corresponding electric charges.

Elementary particles in the SM corresponding to the vector fields (carrying spin 1) are called gauge bosons and present force carriers. Gluon g for the strong interaction, photon γ for the electromagnetic interaction and Z and W bosons for the weak interaction. The last elementary particle of the SM is a scalar boson (with spin 0) H, also called the Higgs boson.

In terms of quantum fields, the SM is composed of gluon fields $G_a, a = 1, .., 8$ (transforming under the $SU(3)_C$ gauge group), electroweak boson fields $W_i, i = 1, 2, 3$ and B (transforming under $SU(2)_L$ and $U(1)_Y$), Higgs-Goldstone field Φ (transforming under $SU(2)_L \times U(1)_Y$) and spinor fields ψ, which can be subsequently divided into leptons transforming under electroweak $SU(2)_L \times U(1)_Y$ and quarks which unlike leptons are also $SU(3)_C$ triplets.

The electroweak sector can be further treated via the Higgs mechanism. Where through the global $SU(2)_L \times U(1)_Y$ spontaneous symmetry breaking (SSB) and further rearrangements, three massive vector bosons $W^{\pm}$, Z, one massless vector boson γ and one massive scalar boson H are obtained in the physical spectrum from the Φ field. For more details consult e.g. [6] or a more exhaustive description [7].

[1] For a recapitulation of the use of symmetries in particle physics from a group theory point of view consult e.g. [5].

1.2 Gauge theories

As mentioned before, Standard Model is a gauge field theory. More light will be shed on this term as it will be used in the rest of this chapter[2]. The approach of [8] or [9] is used (sometimes together with a notation of [5]).

A gauge theory is a theory in which the action is invariant under some specific continuous group symmetry. Note that the symmetry being global (meaning unlocalized) implies a conservation of currents related to this symmetry as is given by the Noether's theorem [10]. By promoting the theory to be also invariant locally, so-called *gauge fields*[3] have to be introduced into the action. The obtained local symmetry with a continuous symmetry group (gauge group) under which the gauge theory is invariant is usually called the *gauge symmetry*.

The gauge theory carries the properties given by its gauge group which also can give an intuition of how the theory will act. The Lagrangian formalism will be used in the following[4], where the action is expressed as

$$S = \int d^4x \mathcal{L}. \tag{1.1}$$

1.2.1 $U(1)$ gauge theory

The simplest example of a gauge theory is an Abelian gauge theory, i.e. a theory with a commutative gauge group: $U(1)$, the prototype of which is the quantum electrodynamics (QED), e.g.

The starting point for the derivation of the complete $U(1)$ theory is a free-field theory with a (massive) fermionic field ψ and a Lagrangian

$$\mathcal{L} = i\bar{\psi}\gamma^\mu\partial_\mu\psi \ (-m\bar{\psi}\psi), \tag{1.2}$$

which is clearly invariant under a global $U(1)$ transformation of ψ:

$$\psi(x) \to \psi'(x) = e^{-i\theta}\psi(x), \tag{1.3}$$

where θ is a phase angle. One can also express θ as $e\alpha$, where e can be identified with the electric charge in the Maxwell's theory. The corresponding conserved current (as given by the Noether's theorem) is then

$$j_\mu(x) = e\bar{\psi}(x)\gamma_\mu\psi(x). \tag{1.4}$$

However, when the transformation is local ($\alpha \to \alpha(x)$), our Lagrangian (1.2) is not invariant under it anymore as the newly appeared $\partial_\mu\alpha(x)$ term is not compensated. In general, this compensation occurs naturally when the original

[2]Even if not always explicitly mentioned.

[3]The description of quantum field theories using the gauge fields as force mediators has led to remarkable discoveries in the last seventy years and the search for symmetries and related conserved currents became the driving force in the particle physics.

[4]As is an usual convention, by Lagrangian it will be referred to the Lagrangian density in the rest of the text.

Lagrangian (1.2) posses a derivative, which transforms the same way as the field itself (it then merits a label *covariant derivative*), instead of the ∂_μ. In the Abelian case, the covariant derivative takes the form

$$D_\mu \psi = \partial_\mu \psi - ieA_\mu \psi, \tag{1.5}$$

where a vector gauge field A_μ, transforming as $A_\mu(x) \to A'_\mu(x) = A_\mu(x) + \partial_\mu \alpha(x)$, is introduced. Thanks to the construction, any object made by repeated application of D_μ is also gauge invariant. For instance, in the $U(1)$ gauge theory one gets

$$[D_\mu, D_\nu] = ie[\partial_\mu A_\nu(x) - \partial_\nu A_\mu(x)], \tag{1.6}$$

where can be recognized the definition of the electromagnetic field strength tensor from the Maxwell's theory

$$F_{\mu\nu} = \partial_\mu A_\nu - \partial_\nu A_\mu. \tag{1.7}$$

Hence, by adding the kinetic term for the gauge field in a form $\mathcal{L}_{kin} = -\frac{1}{4} F_{\mu\nu} F^{\mu\nu}$, the Lagrangian of the $U(1)$ gauge theory can be completed as [8]

$$\mathcal{L} = -\frac{1}{4} F_{\mu\nu} F^{\mu\nu} + \bar{\psi}(i\gamma^\mu D_\mu - m)\psi. \tag{1.8}$$

It is apparent that there is a whole equivalence class of fields $\{A^{(\alpha)}, \psi^{(\alpha)}\}$ leaving the Lagrangian invariant. This property is convenient for solving specific problems by choosing a specific $A \in \{A^{(\alpha)}\}$ and yet leaving the physics 'untouched'. This constraint for extra degrees of freedom is called *gauge fixing*. An example of a gauge condition[5] is $n \cdot A = n_\mu A^\mu = 0$, where specific choice of n_μ gives then:

- axial gauge $n^2 = -1$: $n = (0, 0, 0, 1) \Rightarrow A_3 = 0$;
- light-cone gauge $n^2 = 0$: $n = (1, 0, 0, 1) \Rightarrow A_0 - A_3 = 0$;
- temporal gauge $n^2 = 1$: $n = (1, 0, 0, 0) \Rightarrow A_0 = 0$.

1.2.2 Yang-Mills theory

The concept used in the previous section can be generalized from the $U(1)$ to an n-dimensional simple Lie group G with the irreducible representation D. The generators $G^a, a = 1, .., n$ of the group G form a Lie algebra with a Lie bracket $[G^a, G^b] = f^{abc} G^c$, where factors $f^{abc} = -f^{bac}$ are called *structure constants* of the group G and the generators G^a satisfy the *Jacobi identity*[6]

$$[G^a, [G^b, G^c]] + [G^c, [G^a, G^b]] + [G^b, [G^c, G^a]] = 0. \tag{1.9}$$

Now, one would like to build a transformation of Dirac fields similarly to (1.3) but according to our Lie group G:

$$\psi(x) \to \psi'(x) = e^{-i\alpha^a T^a} \psi(x). \tag{1.10}$$

[5] Probably the most famous example of gauge fixing is the Coulomb gauge: $\mathrm{div}\vec{A} = 0, A_0 = \Phi$. A different example is presented here as the temporal gauge will be needed later in the text.

[6] A similar identity as (1.9) holds also for f^{abc}, then it can be proved that f^{abc} is antisymmetric in all three indices.

So, if one has a (global) unitary transformation $U(\alpha)$ (with exponential parameters α^a), then the linear map $D(g), g \in G$ (representation) can be equivalently expressed as

$$D(g) = \exp(\alpha^a D(G^a)) \equiv \exp(-i\alpha^a T^a) = U(\alpha). \tag{1.11}$$

The $T^a = iD(G^a)$ is then a representation of G^a on some representational space V and in terms of matrices one can define $[T^a]^{bc} \equiv -if^{abc}$. Thus, the structure constants themselves produce a representation, also called the *adjoint representation*, and in terms of the commutator of the matrices it does hold: $[T^a, T^b] = if^{abc}T^c$[7]. By choosing a suitable basis of G, it holds $\eta^{ab} = -\delta^{ab}$ and hence for any irreducible representation D one can obtain a normalization

$$\mathrm{Tr}(T^a T^b) = K_D \delta^{ab}. \tag{1.12}$$

Further, the transformation built above (1.11) will be promoted to be local $\alpha \to \alpha(x)$ and from now the corresponding group will be taken as a gauge group. The corresponding gauge fields undergo the following gauge transformation leaving the Lagrangian invariant

$$A_\mu(x) \to A'_\mu(x) = A^{(\alpha)}_\mu(x) = U(\alpha)A_\mu U(\alpha)^{-1} - \frac{i}{g}U(\alpha)\partial_\mu U(\alpha)^{-1}, \tag{1.13}$$

where g is a general *coupling constant*[8]. It is apparent that by different choices of $U(\alpha)$ one gets specific configurations of A_μ leaving the observables the same. Thus formally, from the whole configuration space $\{A_\mu(x)\}$, one can select the equivalence classes $\{A^{(\alpha)}_\mu(x)\}$ usually called *orbits*[9].

For the infinitesimal transformations can be written

$$U(x) = 1 - ig\alpha^a(x)T^a + \mathcal{O}(g^2). \tag{1.14}$$

Then, using the covariant derivative $D_\mu = \mathbb{1}\partial_\mu + igA_\mu$, one can derive the transformation of the gauge field A_μ as

$$A'_\mu = A_\mu + \partial_\mu \alpha - ig[\alpha, A_\mu], \tag{1.15}$$

where $\alpha \equiv \alpha^a T^a$. It is also consistent to want $A_\mu \equiv A^a_\mu T^a$ as everything is then a linear combination of T^a.

Similarly to the $U(1)$ case, one knows that by a repeated application of D_μ the gauge invariance is not broken. Furthermore, in an analogy with (1.6), can be constructed

$$[D_\mu, D_\nu] = ig(\partial_\mu A_\nu(x) - \partial_\nu A_\mu(x) + ig[A_\mu, A_\nu]). \tag{1.16}$$

[7] One can see that for a case, where T^a would commute, the $U(1)$ transformation (1.3) would be restored.

[8] In the case of $U(1)$ the coupling constant was labeled as e.

[9] There is a special class of equivalence giving $A'_\mu(x) = -\frac{i}{g}U(\alpha)\partial_\mu U(\alpha)^{-1}$, which is called the *pure gauge*.

The gauge field strength tensor for this more general case then takes form

$$F_{\mu\nu} = \partial_\mu A_\nu - \partial_\nu A_\mu + ig[A_\mu, A_\nu]. \tag{1.17}$$

Thanks to the non-commutativity of the gauge fields, one gets new special terms when constructing a Lagrangian using F^2, corresponding to cubic and quartic self-interactions of the gauge fields, which has been found to manifest in the nature for specific Lie algebras. One case has already been discussed: the Abelian $U(1)$, which, for example, represents the electromagnetism. Now, a more general non-Abelian $SU(n)$ algebra, representing so-called *Yang-Mills theories*, can be presented. As one already has all the necessary puzzles, the full Yang-Mills Lagrangian can be presented

$$\mathcal{L}_{YM} = -\frac{1}{4K_D}\mathrm{Tr}[F_{\mu\nu}F^{\mu\nu}] + \bar{\psi}(i\gamma^\mu D_\mu - m)\psi, \tag{1.18}$$

where $F^a_{\mu\nu} = \partial_\mu A^a_\nu - \partial_\nu A^a_\mu - g f^{abc} A^b_\mu A^c_\nu$.

One might also built another term using $F^a_{\mu\nu}$ and yet keep the gauge invariance of (1.18) and the renormalizability of the theory[10]

$$\sim F^a_{\mu\nu}\tilde{F}^{a\mu\nu} = \epsilon^{\mu\nu\rho\sigma} F^a_{\mu\nu} F^a_{\rho\sigma}. \tag{1.19}$$

However, one can show that this term corresponds to a surface integral when evaluating the action (1.1) using the Wick rotation:

$$\begin{aligned} S &= \int d^4x \epsilon^{\mu\nu\rho\sigma} F^a_{\mu\nu} F^a_{\rho\sigma} = \int d^4x 4\epsilon^{\mu\nu\rho\sigma} \partial_\mu (A^a_\nu \partial_\rho A^a_\sigma - \frac{2ig}{3} f^{abc} A^a_\nu A^b_\rho A^c_\sigma) = \\ &= 4i\epsilon^{\mu\nu\rho\sigma} \int d^4x_E \partial_\mu (A^a_\nu \partial_\rho A^a_\sigma - \frac{2ig}{3} f^{abc} A^a_\nu A^b_\rho A^c_\sigma) = \\ &= 4i\epsilon^{\mu\nu\rho\sigma} \int_{S_3} d\Sigma_\mu (A^a_\nu \partial_\rho A^a_\sigma - \frac{2ig}{3} f^{abc} A^a_\nu A^b_\rho A^c_\sigma) \xrightarrow{A_\mu(x\to\infty)\to 0} 0. \end{aligned} \tag{1.20}$$

The assumption that the potential vanishes in the infinity seems natural and was taken for granted for many years. Nevertheless, later with the discovery of *instantons* it has been found how non-trivial this assumption is. This topic will be recalled in the section 1.3.3.

1.2.3 Quantization of Yang-Mills fields

The path integral method will be used here as it also allows a more efficient treatment of problems in the following sections. This formalism is also very convenient for both qualitative and quantitative description of the behaviour of perturbative theories. The general properties of divergences coming from higher order contributions to transition amplitudes will be, however, discussed in the next section 1.2.4.

[10]The renormalization will be discussed more in the section 1.2.4

In the context of the perturbation theory most of the calculations go down to a generating functional, in general given as

$$Z_E[J] = \int \mathcal{D}\Phi \exp\Big(\frac{i}{\hbar}\int d^4x[\mathcal{L} + \hbar J(x)\Psi(x)]\Big) \tag{1.21}$$

with general external sources J. The latter is usually referring to specific Feynman diagrams for a given action and field operators in a given order of coupling constant g. Many theories share the same properties of n-point correlation functions. They can be expressed as the n-th functional derivative of the generating functional over the external sources

$$\begin{aligned} G^{(n)}(x_1,\ldots,x_n) &= \left(\frac{1}{i}\right)^n \frac{\delta^n}{\delta J(x_1)\ldots J(x_n)} Z_E[J] = \\ &= \langle 0|T\Phi(x_1)\ldots\Phi(x_n)|0\rangle = \int \mathcal{D}\Phi \exp\Big[\frac{i}{\hbar}S[\Phi]\Big]. \end{aligned} \tag{1.22}$$

For the quantization of a gauge field theory, one may use the general generating functional as presented above and only take the path integral over the gauge field A_μ in hopes of obtaining a measurable quantity as

$$Z[J] = \int \mathcal{D}A_\mu e^{iS[A_\mu]}. \tag{1.23}$$

However, this will not happen as one would in fact run over all possible configurations and hence multiple-count physically equivalent configurations. It has already been discussed in the previous section that there is an option of splitting the configuration space $\{A_\mu(x)\}$ into orbits $\{A_\mu^{(\alpha)}(x)\}$. Consequently, the corresponding integrands will be constant along the orbit giving an infinite constant proportional to the volume of the gauge group G. This is in principle not a problem as this constant can be absorbed into the definition of the measure of the integral. The problem arises when one wants to treat the path integral perturbatively (which is usually always) as already in the second order of the action appear zero modes. This presents an issue when one wants to derive the Feynman rules as e.g. the corresponding Green functions (1.22) cannot be defined (respectively their defining integral is divergent).

In order to overcome this problem one can use the Faddeev–Popov method, which means to factorize out the integration over gauge group members first and apply the perturbation expansion afterwards. This can be achieved by insertion of the following identity defining the Faddeev–Popov determinant $\Delta[A_\mu]$

$$1 = \Delta[A_\mu]\int \mathcal{D}\alpha\,\delta[f[A_\mu^{(\alpha)}]] \tag{1.24}$$

into the generating functional $Z[J]$, where a function $f[A_\mu^{(\alpha)}] = 0$ is assumed and that the equation has one solution for any A_μ. This means that $f[A_\mu^{(\alpha)}] = 0$ defines a hypersurface crossing each orbit exactly once, but that in other words means that the gauge has just been fixed. By insertion of (1.24) and further rearrangements one gets

$$Z[J] = \Big(\int \mathcal{D}\alpha\Big)\int \mathcal{D}A_\mu \delta[f[A_\mu]]\Delta[A_\mu]e^{iS[A_\mu]} \tag{1.25}$$

as the quantities are independent of α. By doing several practical choices, the Faddeev–Popov determinant can be evaluated as a functional derivative

$$\Delta[A_\mu] = \det \left. \frac{\delta f[A_\mu^{(\beta)}]}{\delta \beta} \right|_{\beta=0} \tag{1.26}$$

and when omitting the prefactor one will get the Faddeev–Popov formula as

$$Z_f[J] = \int \mathcal{D}A_\mu \delta(f[A]) \exp\Big(i \int d^4x [\mathcal{L} + J_\alpha^\mu A_\mu^{(\alpha)}] \Big) \det \left. \frac{\delta f[A_\mu^{(\beta)}]}{\delta \beta} \right|_{\beta=0} . \tag{1.27}$$

In the case of gauge field theories one has to be cautious when evaluating the transition amplitudes as for given gauges some unphysical gauge-dependent contributions can appear, so-called Faddeev–Popov ghosts, which has to be, however, taken into account to keep the information complete. Their nature is nowadays well-understood and can be nicely treated using the BRST quantization[11].

During the evolution of quantum field theory, it was very early realized that from some given order of g the Feynman amplitudes become divergent even if their contributions should be more and more suppressed. This phenomenon challenging the whole idea behind the perturbation theory is more discussed in the following section.

1.2.4 Renormalization

As mentioned earlier, during the evaluation of contributions in higher orders of perturbation expansion one may encounter divergences in the amplitudes which would bring infinities to the results. This typically occurs at the loop level but in general a (superficial) degree of divergence can be evaluated for the specific configuration of any Feynman diagram. When evaluating an amplitude with such singularity, one may isolate it using some type of the regularization. The Λ parameter presenting an energy cutoff will be used here as a regulator. Then in order to get a finite result with a clear physical interpretation a series of renormalization techniques has been developed for the subtraction of infinite contributions (techinque of counterterms).

This leads to a definition of the *renormalizability* of the quantum field theory, which means that only a finite number of counterterms is needed for an elimination of all divergences. This is an elegant and useful property of the theory, however, not compulsory as at each order of the perturbation expansion there is a finite number of divergent contributions which need to be renormalized. Thus, even a non-renormalizable theory can offer a very good description of the physics only the computational demands increase drastically when one requires more precise predictions[12].

[11] Even if this topic is essential in the context of gauge field theories, the thesis aims into a different corner of Yang-Mills theory. A detailed discussion on the latter can be found e.g. in [11]

[12] This led to a renaissance for many effective field theories in the 21st century thanks to both the technological progress and a higher manpower in physics.

The procedure of renormalization usually requires a redefinition of the original (commonly called *bare*) coupling constant g_{bare} and mass m_{bare} but frequently also of the field operators themselves[13]. Its root is in the subtraction of the divergent part in some sense, where the exact form is given by the choice of the renormalization scheme and a renormalization scale μ, at which the presented result is valid. The redefinition of field operators can be then thought of as

$$\Phi_{bare} = \sqrt{Z}\Phi_{ren}, \text{ where } Z = Z\Big(\frac{\Lambda}{\mu}, g_{bare}\Big). \tag{1.28}$$

The scaling Z of the field operators can be determined by a direct calculation of corresponding Feynman diagrams. If one performs a Fourier transform on the Green function (1.22)

$$G^{(n)}(p_1, \dots, p_n) = \int d^4x_1 \cdots d^4x_n G^{(n)}(x_1, \dots, x_n) e^{i(p_1 x_1 \cdots p_n x_n)}, \tag{1.29}$$

its renormalization can be then presented as

$$G^{(n)}_{bare}(p_1, \dots, p_n, g_{bare}, \Lambda) = Z^{n/2} G^{(n)}_{ren}(p_1, \dots, p_n, g_{ren}, \mu). \tag{1.30}$$

As $G^{(n)}_{bare}$ does not depend on the renormalization scale μ, one can straightforwardly derive the following relation

$$\Big[\mu\frac{\partial}{\partial\mu} + \beta(g_{ren})\frac{\partial}{\partial g_{ren}} + n\gamma(g_{ren})\Big] G^{(n)}_{ren}(p_1, \dots, p_n, g_{ren}, \mu) = 0, \tag{1.31}$$

also being called the homogeneous Callan-Symanzik equation[14] [12]. The presented β-function and the 'anomalous dimension' γ are defined as follows

$$\beta(g) \equiv \mu\frac{\partial g}{\partial\mu}\bigg|_{g_{bare},\Lambda \text{ fixed}}; \gamma(g) \equiv \frac{1}{2}Z^{-1}\mu\frac{\partial Z}{\partial\mu}\bigg|_{g_{bare},\Lambda \text{ fixed}}. \tag{1.32}$$

The anomalous dimension presents a quantum correction to the mass-dimension of field operators, giving some effective mass-dimension to the renormalized operators due to interactions among particles. The β-function describes the scaling of the renormalized coupling constant with the energy scale, a phenomenon also called the *running coupling*.

This behaviour is closely related to whichever energy region the physics can still be well-described by the given quantum field theory and when a new effective field theory is necessary. This point, where $\beta(g) \to 0$ and hence $g \to \infty$, is called the *Landau pole*. For example QED has a positive β-funtion, at low energies its coupling constant goes to a well-known electric charge constant and its Landau pole lies at energies far beyond what we are able to achieve. However, it is expected that beyond this point a new theory is necessary. In fact, the electroweak

[13] In the case of Yang-Mills theory the ghost fields has to be renormalized as well, while the counterterms for the gauge-fixing part are not needed. In order to remove all the divergences in the Yang-Mills theory a renormalization scheme respecting the BRST symmetry has to be chosen.

[14] Also a name renormalization group equation is frequently used.

theory incorporates the QED, but it also has a Landau pole and provides a motivation for searches for another unifying theory beyond these. This brings a wide spectrum of possible effective theories for various scenarios of a behaviour with changes of the energy scale. One such remarkable scenario was the finding out that non-Abelian theories may have a negative β-function with the Landau pole in the low-energy limit[15]. The QCD is one such example and the confinement of quarks in hadrons and so-called asymptotic freedom are the consequences, which will be discussed more in the following section.

1.3 Quantum chromodynamics

The quantum chromodynamics (QCD) is a prototype of a Yang-Mills theory with an $SU(3)$ gauge group. The $SU(3)$ Lie algebra has eight generators conventionally defined by the Gell-Mann matrices λ^a [13]

$$T^a \equiv \frac{\lambda^a}{2};\ \mathrm{Tr}(T^a T^b) = \frac{1}{2}\delta^{ab}. \tag{1.33}$$

Hence together with eight vector gauge potentials A^a_μ, called gluons, one can define a gluon field strength tensor $G_{\mu\nu} \equiv \frac{\lambda^a}{2} G^a_{\mu\nu}$ invariant under $SU(3)$. As already mentioned in the first recapitulation of the Standard Model 1.1, gluon gauge fields are acting on triplets of N_f fermion fields called quarks

$$q_f = \begin{pmatrix} q_{f,1} \\ q_{f,2} \\ q_{f,3} \end{pmatrix}. \tag{1.34}$$

The $SU(3)$ is usually being referred as a colour gauge group as colour was originally a new quantum number allowing quarks, yielding the Pauli principle, being bound into hadrons. For this study, however, a different quantum number will be in the center of attention, the flavour f. As already stated in the table 1.1, six flavours of quark fields has been found up to now and hence one could take $N_f = 6$ in the following. If one suppresses the colour indices and emphasize the flavour ones, the QCD Lagrangian can be simply expressed as

$$\mathcal{L}_{QCD} = -\frac{1}{2}\mathrm{Tr}_c[G_{\mu\nu}G^{\mu\nu}] + \sum_{f=1}^{N_f} \bar{q}_f (i\gamma^\mu D_\mu - m_f) q_f, \tag{1.35}$$

where the approximate quark masses m_f can be found in the following table 1.2.

q_f	u	d	c	s	t	b
m_f	2.2 MeV	4.7 MeV	1.28 GeV	96 MeV	4.18 GeV	173.1 GeV

Table 1.2: Quark masses [14].

One can see quite a big gap between the masses of the first two u and d (and potentially of s) and the rest of quarks. This gap acquires even more importance when also compared to the energy at which QCD becomes non-perturbative, which will be more analyzed in the forthcoming sections.

[15]For this theoretical prediction were D. J. Gross, H. D. Politzer and F. Wilczek awarded by the Nobel prize in 2004 after experimental confirmation.

1.3.1 Running coupling

An exhaustive summary on the strong coupling constant can be found in [15] and general results on the transition area, where QCD becomes non-perturbative, will be briefly presented here. In the following, the strong coupling constant will be taken as

$$\alpha_s(Q^2) \equiv \frac{g_s^2(Q^2)}{4\pi}, \tag{1.36}$$

where the momentum transfer scale Q^2 is given by a change of the sign of the momentum of the process $Q^2 = -q^2$ and the renormalization scale will be taken equal to the physical momentum transfer $\mu \equiv Q$. When working in the dimensional regularization and in the MS (or $\overline{\text{MS}}$[16]) renormalization scheme, the β-function can be evaluated as a series

$$\beta(\alpha_s) = Q^2 \frac{\partial \alpha_s}{\partial Q^2} = -\left(\frac{\alpha_s}{4\pi}\right)^2 \sum_{n=0} \left(\frac{\alpha_s}{4\pi}\right)^n \beta_n, \tag{1.37}$$

where the coefficients β_n are given by contributions of diagrams of the given order as:

$$\begin{aligned} \beta_0 &= 11 - \frac{2}{3} N_f \\ \beta_1 &= 102 - \frac{38}{3} N_f \\ &\vdots \end{aligned} \tag{1.38}$$

By a simple substitution one can show that in the high-energy limit the dependence of the coupling is logarithmic. Specifically, at the 1-*loop* level

$$\alpha_s(Q^2) = \frac{4\pi}{\beta_0 \ln\left(\frac{Q^2}{\Lambda^2}\right)}. \tag{1.39}$$

This, however, does not apply in the low-energy region and it has been proven that at energy under 1 GeV, the theory cannot be treated perturbatively. It was experimentally demonstrated that below this energy the particles cannot act as free and become confined within a state, which is colour charge neutral on the outside. These states are called *hadrons* and the process is called *hadronization.*

It has been demonstrated that the character of the coupling constant changes at $Q \sim 1$ GeV $= Q_0$, see figure 1.1, and to study the physics under this scale a new perturbative effective theory describing the physics of hadrons is needed. An example of such theory is the chiral perturbation theory (χPT), which inherits the symmetries of QCD we will describe further.

[16] The minimal subtraction scheme clears away only the regulator arisen from the dimensional regularization, while the MS-bar clears away also the accompanying constants. Both leave the coupling constant gauge invariant.

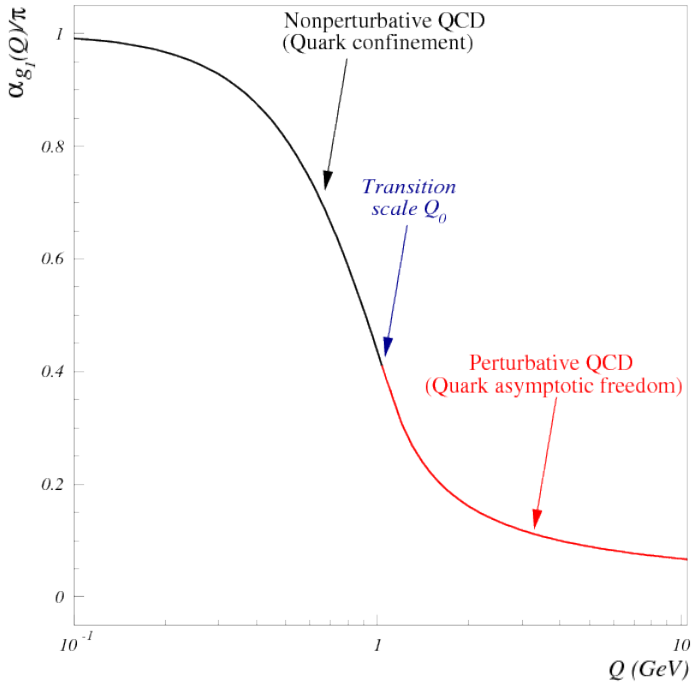

Figure 1.1: A transition between coupling as given by the perturbative QCD and as predicted (and measured) in the low-energy region [15].

1.3.2 Chiral symmetry

Only a few useful results will be presented in this section, for more comprehensive explanation see [16].

When introducing the projection operators

$$P_R = \frac{1+\gamma_5}{2}, P_L = \frac{1-\gamma_5}{2} \tag{1.40}$$

the fields q can be projected into right-handed and left-handed components

$$q_R = P_R q, q_L = P_L q. \tag{1.41}$$

The QCD Lagrangian (1.35) can be then rewritten in the following form

$$\begin{aligned}\mathcal{L}_{QCD} = -\frac{1}{2}\mathrm{Tr}_c[G_{\mu\nu}G^{\mu\nu}] + \sum_{f=1}^{N_f}(i\bar{q}_{R,f}\gamma^\mu D_\mu q_{R,f} + i\bar{q}_{L,f}\gamma^\mu D_\mu q_{L,f}) \\ - \sum_{f=1}^{N_f}(\bar{q}_{R,f}\mathcal{M}q_{R,f} + \bar{q}_{L,f}\mathcal{M}q_{L,f}),\end{aligned} \tag{1.42}$$

where $\mathcal{M}$ is the general mass matrix. One can also perform a limit $m_f \to 0$ in the former Lagrangian (1.35) and then obtain a variant of (1.42) with a large global symmetry $U(N_f)_R \times U(N_f)_L$. This is of course not a physical case as one knows from the table 1.2. However, from the previous section 1.3.1 one has an information that something new could appear at energies below Q_0. By

comparison it can be seen that $m_u, m_d \ll Q_0$ and thus at least an approximate global $U(2)_R \times U(2)_L$ symmetry (as expressed in the Wigner-Weyl realization) can be assumed. This symmetry is not manifest explicitly in the spectrum of hadrons, but one can rewrite it in a Nambu-Goldstone realization, i.e. $U(2)_R \times U(2)_L = U(2)_V \times U(2)_A$, in order to study it in more details.

As for the $U(2)$ transformation a factor $e^{-i\theta}$ can be extracted from the transformation matrix U

$$q_{R,L} \to U_{R,L} q_{R,L} = \exp\left(-i \sum_{a=1}^{3} \alpha_{R,L}^a \frac{\tau^a}{2}\right) e^{-i\theta} q_{R,L}, \tag{1.43}$$

one can decompose $U(2) \times U(2) = SU(2) \times SU(2) \times U(1) \times U(1)$. The part $SU(2) \times SU(2)$ will be referred in the following as the chiral symmetry.

By studying the physical spectrum of QCD, some pattern corresponding to the vectorial ($V = R+L$) part $U(2)_V \subset U(2)_R \times U(2)_L$ can be actually observed. The $U(1)_V \subset U(2)_V$ symmetry corresponding to the vectorial baryon number is an exact symmetry of QCD irrespective to the value m_f, while $SU(2)_V \subset U(2)_V$ corresponding to the isospin quantum number would be exact in a case that $m_u = m_d$, which does not hold. Nevertheless, the values are very close and the symmetry is only slightly violated and one can observe approximately degenerate multiplets of hadrons (e.g. the pion triplet or the nucleon doublet).

An axial ($A = R - L$) symmetry $U(2)_A \subset U(2)_R \times U(2)_L$ is not preserved by the QCD vacuum $< \bar{u}u > = < \bar{d}d > \neq 0$, which in a case it was an exact global symmetry would imply the spontaneous symmetry breaking and hence the appearance of four Nambu-Goldstone bosons[17] in the physical spectrum [17]. Remarkably, the spectrum of hadrons contain a triplet of pions corresponding to the $SU(2)_A$ whose mass $m_\pi \to 0$ for $m_u, m_d \to 0$. These are called *pseudo-Goldstone bosons* as they are not massless but yet possess only a small mass as the symmetry is only slightly violated. However, no fourth (pseudo-)Goldstone corresponding to the remaining $U(1)_A$ axial symmetry has been observed.

The situation with $U(1)_A$ is, in fact, more complicated as the corresponding current $J_5^\mu = \frac{1}{2}\bar{q}\gamma^\mu\gamma_5 q$ is not conserved due to the presence of the chiral anomaly $\partial_\mu J_5^\mu = \frac{\alpha_s}{4\pi} G_a^{\mu\nu} \tilde{G}_{a\mu\nu}$. The right-hand side has been encountered earlier, in the section 1.2.2, where has been shown that it is a total divergence $\partial_\mu K^\mu = G_a^{\mu\nu}\tilde{G}_{a\mu\nu}$, where K^μ is defined

$$K^\mu \equiv 4\epsilon^{\mu\nu\rho\sigma}\left(A_\nu^a \partial_\rho A_\sigma^a - \frac{2ig}{3} f^{abc} A_\nu^a A_\rho^b A_\sigma^c\right). \tag{1.44}$$

Thus, by incorporating this term it would be possible to construct a conserved current $\tilde{J}_5^\mu = J_5^\mu - \frac{\alpha_s}{4\pi} K^\mu$. Nevertheless, this does not manifest in the physical spectrum of hadrons even as there was not seemingly any reason for it, which became known as the $U(1)_A$ *problem*.

[17] One Nambu-Goldstone boson for each generator.

1.3.3 $U(1)$ problem

The resolution of the problem presented above came from a better understanding of the QCD vacuum. For gauge fields one can take the vacuum state to be the state where the vector potential is either zero or in a gauge configuration equivalent to zero. However, proper study of these configurations reveals that the structure of the vacuum is for non-Abelian gauge theories richer than expected.

Further will be proceeded in the $SU(2)$ subgroup[18] homeomorphic to the S^3, which is much more natural topological space to work in. It is also convenient to study the latter in the temporal gauge $A_0^a = 0$ presented in the section 1.2.1 as then the spatial gauge fields are time-independent and transform as

$$A^i(\vec{r}) \equiv \frac{\tau^a}{2} A_a^i \to U A^i(\vec{r}) U^{-1} + \frac{i}{g} U \partial^i U^{-1}, \tag{1.45}$$

where τ^a are Pauli matrices. Thanks to the equivalence between different gauge field configurations, one can work in the pure gauge[19]. It will be required that the gauge transformation matrices satisfy a boundary condition $U(\vec{r}) \xrightarrow{r\to\infty} 1$. Than the instanton configuration gives $A^i \xrightarrow{r\to\infty} \frac{i}{g} U \partial^i U^{-1} + \mathcal{O}(1/r^2)$, which maps the physical space onto the group space. Thus, one get an $S^3 \to S^3$ map, which splits $U(\vec{r})$ into different homotopy classes $U_n(\vec{r})$ characterized by a winding number n, causing $U_n \xrightarrow{r\to\infty} e^{i2\pi n}$. The winding number is given by the Jacobian of $S^3 \to S^3$ transformation

$$n \equiv \int d^3 r \epsilon^{ijk} \mathrm{Tr}[U^{-1} \partial^i U U^{-1} \partial^j U U^{-1} \partial^k U], \tag{1.46}$$

which is equivalent to the Chern-Simons functional as the A^i is the pure gauge

$$n \approx N[\vec{A}] = \frac{i g^3}{24\pi^2} \int d^3 r \epsilon^{ijk} \mathrm{Tr}[A_n^i(\vec{r}) A_n^j(\vec{r}) A_n^k(\vec{r})]. \tag{1.47}$$

Obviously, one can construct the n-th gauge transformation matrix U_n by compounding $(U_1)^n$, from which follows that the vacuum state corresponding to $A_n^i(\vec{r})$ is not really gauge invariant because $U_1 |n\rangle = |n+1\rangle$.

Nevertheless, one can construct a gauge invariant vacuum state by a superposition

$$|\theta\rangle = \sum_n e^{-in\theta} |n\rangle , \tag{1.48}$$

so-called θ-vacuum. By using this more complex structure, the vacuum functional splits into distinct sectors

$$\langle\theta|\theta\rangle = \sum_{m,n} e^{im\theta} e^{-in\theta} \langle m|n\rangle = \sum_\nu e^{i\nu\theta} \sum_n \langle n+\nu|n\rangle , \nu \in \mathbf{N}, \tag{1.49}$$

[18] The case of a general $SU(n)$ or our QCD $SU_c(3)$ can be further generalized.

[19] In the quantum field theory, the field configurations vanishing at infinity, which have some 'topological twist' (expressed using the *winding number*), are called *instantons*. A nice review of instantons in QCD presents [18].

characterized by a winding number ν. Using definitions of n (1.47) and K^μ (1.44), it can be shown that ν has a gauge invariant meaning

$$\nu = \frac{\alpha_s}{8\pi} \int d^4x G^{a\mu\nu} \tilde{G}^a_{\mu\nu} \tag{1.50}$$

and in terms of the path integral can be written

$$\langle \theta | \theta \rangle = \sum_\nu \int \mathcal{D}A_\mu e^{iS_{eff}[A]} \delta\Big(\nu - \frac{\alpha_s}{8\pi} \int d^4x G^{a\mu\nu} \tilde{G}^a_{\mu\nu}\Big). \tag{1.51}$$

Thus, θ can be reinterpreted in terms of an effective action

$$S_{eff}[A] = S[A] + \theta \frac{\alpha_s}{8\pi} \int d^4x G^{a\mu\nu} \tilde{G}^a_{\mu\nu} \tag{1.52}$$

and therefore the surface term, which was originally driven away in section 1.2.2, has been recovered. The term is also directly connected to the chiral anomaly from the last section

$$\partial_\mu J^\mu_5 = \frac{\alpha_s}{4\pi} G^{a\mu\nu} \tilde{G}^a_{\mu\nu}. \tag{1.53}$$

Thus, the $U(1)_A$ cannot be a symmetry of QCD which also means that there is no $U(1)$ problem.

Nevertheless, with this new term another problem occurs

$$\int d^4x G^{a\mu\nu} \tilde{G}^a_{\mu\nu} \sim \int d^4x \vec{E}^a \vec{B}^a. \tag{1.54}$$

This means that this term directly violates P and CP symmetries in strong interactions, which is something that has never been experimentally observed. This phenomenon became known as the *strong CP problem*.

1.3.4 Strong *CP* problem

The vacuum structure is not the only contribution to the CP violation of strong interactions. In the latter was neglected the effect of the quark mass term

$$\mathcal{L}_{mass} = -\bar{q}_R \mathcal{M} q_R - -\bar{q}_L \mathcal{M}^\dagger q_L, \tag{1.55}$$

where $\mathcal{M}$ is the mass matrix emerging from the SSB in the weak sector, which is neither hermitian, neither diagonal. One can diagonalize the matrix by unitary transformations $(U(1)_A)$

$$q_R \to e^{i\frac{\alpha}{2}} q_R, q_L \to e^{-i\frac{\alpha}{2}} q_L, \tag{1.56}$$

where the angle $\alpha = \frac{1}{Nf} \mathrm{Arg}\det \mathcal{M}$. The total angle giving the CP violation of strong interactions is then

$$\bar{\theta} = \theta + \mathrm{Arg}\det \mathcal{M} \tag{1.57}$$

and $\bar{\theta}$ becomes a free parameter of the theory, where any value is equally likely.

On the other side the experimental observations say that $\left|\bar{\theta}\right| \leq 10^{-10}$ [14]. The reason why $\bar{\theta}$ is so unnaturally small or even possibly zero have not yet been

found and thus presents a fine tuning problem in this context called the strong CP problem.

There are several possible solutions to the strong CP problem [19]:

- Anthropic principle;
- Unconventional dynamics;
- Massless quark;
- Additional chiral symmetry.

The first solution is not a plausible answer, however cannot be ruled out unless some mechanism responsible for the CP conservation is found.

The second solution proposes that the solution of the $U(1)$ problem presented above is not the correct one and that there is a different mechanism.

The third one was a possible candidate within the SM with a massless quark or more specifically with $m_u = 0$ giving rise to an additional chiral symmetry enabling effectively rotating the θ away. Today we know that $m_u/m_d = 0.48$ [14] and thus this case does not solve the problem.

The last solution persists the most plausible one and resides in adding the SM an additional global $U(1)$ chiral symmetry.

2. Axions

As discussed in the section 1.3.4, probably the most plausible solution to the strong CP problem is by introducing a new $U(1)$ symmetry into the SM as proposed by R. D. Peccei and H. R. Quinn [20], who showed that the strong CP problem remains solved even if this symmetry is consequently spontaneously broken[1]. This symmetry can be introduced by adding a new CP conserving dynamical field $a(x)$, which effective potential saddles at a value causing cancellation of the θ term, which became known as the Peccei-Quinn mechanism. Weinberg and Wilczek independently stated that assuming such field necessarily leads to the appearance of new pseudoscalar boson, so-called *axion* [21] [22].

2.1 QCD axions

Following the derivation in [23], an axion field $a(x)$ will be presented as transforming under $U(1)$ as $a(x) \to a(x) + \alpha f_a$, where f_a is related to its SSB scale, and having a chiral anomaly

$$\partial_\mu J^\mu = \xi \frac{a}{f_a} \frac{g^2}{32\pi^2} G^a_{\mu\nu} \tilde{G}^{a\mu\nu}, \tag{2.1}$$

where ξ is a model dependent parameter. This allows one to present the extension of the SM in a model independent way as

$$\mathcal{L}_{total} = \mathcal{L}_{SM} + \bar{\theta} \frac{g^2}{32\pi^2} G^a_{\mu\nu} \tilde{G}^{a\mu\nu} - \frac{1}{2} \partial_\mu a \partial^\mu a + \mathcal{L}_{int}[\partial^\mu a / f_a; \Psi] + \xi \frac{a}{f_a} \frac{g^2}{32\pi^2} G^a_{\mu\nu} \tilde{G}^{a\mu\nu} \tag{2.2}$$

and ensuring that the effective action

$$\Gamma[a, A_\mu] = -\int d^4x V_{eff} \tag{2.3}$$

gives a periodic effective potential in a form similar to

$$V_{eff}(a) \sim m_a^2 f_a^2 [1 - \cos(a/f_a)]. \tag{2.4}$$

Thus, when the potential relaxes in its minimum

$$\left\langle \frac{\partial V_{eff}}{\partial a} \right\rangle = -\frac{\xi}{f_a} \frac{g_s^2}{32\pi^2} \left\langle G^a_{\mu\nu} \tilde{G}^{a\mu\nu} \right\rangle \Big|_{\langle a \rangle = -\bar{\theta} f_a / \xi} = 0, \tag{2.5}$$

one gets a Lagrangian with $a_{phys} = a - \langle a \rangle$, where the $\bar{\theta}$-term for QCD is effectively zero forbidding SSB in the vectorial subgroup of the flavour $U(2) \times U(2)$ (from the section 1.3.2) due to the Vafa-Witten theorem [24]. Furthermore, the axion mass can be defined expanding the effective potential

$$m_a^2 \equiv \left\langle \frac{\partial^2 V_{eff}}{\partial a^2} \right\rangle = -\frac{\xi}{f_a} \frac{g_s^2}{32\pi^2} \frac{\partial}{\partial a} \left\langle G^a_{\mu\nu} \tilde{G}^{a\mu\nu} \right\rangle \Big|_{\langle a \rangle = -\bar{\theta} f_a / \xi} \tag{2.6}$$

[1] Today the symmetry is usually referred as the Peccei-Quinn symmetry and it is labelled $U(1)_{PQ}$.

and one gets a general model-independent effective Lagrangian

$$\begin{aligned}\mathcal{L}_{total} = \mathcal{L}_{SM} + \mathcal{L}_{int}[\partial^\mu a_{phys}/f_a; \Psi] - \frac{1}{2}\partial^\mu a_{phys}\partial_\mu a_{phys} \\ - \frac{1}{2}m_a^2 a_{phys}^2 + \xi\frac{a_{phys}}{f_a}\frac{g^2}{32\pi^2}G^a_{\mu\nu}\tilde{G}^{a\mu\nu}.\end{aligned} \tag{2.7}$$

To extract any more specific information about axions, the mechanism introducing axions into the SM has to be presented and hence any further results will be model-dependent. However, there are several generic features these models will share as thanks to the chiral anomaly axions will possess some mass as well as their predominant coupling will be effectively to two photons like in the case of π^0 and η pseudoscalar mesons. Thus, the effective Lagrangians for low-energy QCD (e.g. the χPT [25]) might be applied as well as the outcomes of the lattice QCD [26] in order to get more precise results.

2.1.1 Peccei-Quinn theory

The original PQ[2] theory [27] assumed two Higgs doublets

$$\phi_1 = \frac{v_1}{\sqrt{2}}e^{i\frac{a}{v_F}x}\begin{pmatrix}1\\0\end{pmatrix},\ \phi_2 = \frac{v_2}{\sqrt{2}}e^{i\frac{a}{v_F}\frac{1}{x}}\begin{pmatrix}0\\1\end{pmatrix}, \tag{2.8}$$

where $x = v_2/v_1$ and $v_F = \sqrt{v_1^2 + v_2^2}$ and the Yukawa interaction Lagrangian

$$\mathcal{L}_{\text{Yukawa}} = \bar{q}_L\phi_1 u_R + \bar{q}_L\phi_2 d_R + \bar{L}_L\phi_1 l_R + \text{h.c.}, \tag{2.9}$$

which is invariant under $U(1)_{PQ}$

$$\begin{aligned}a &\to a + \alpha v_F;\\ u_R &\to e^{-i\alpha x}u_R;\\ d_R &\to e^{-i\alpha/x}d_R;\\ l_R &\to e^{-i\alpha/x}l_R.\end{aligned} \tag{2.10}$$

If one omits the lepton part, the associated Noether current will be

$$J^\mu_{PQ} = v_F\partial^\mu a + x\bar{u}_R\gamma^\mu u_R + \frac{1}{x}\bar{d}_R\gamma^\mu d_R \tag{2.11}$$

giving the coefficient ξ for this model

$$\xi = \frac{N_f}{2}\Big(x + \frac{1}{x}\Big). \tag{2.12}$$

In the following will be proceeded in the limit with two light quarks with an effective Lagrangian of the non-linear sigma model [16]. The quark operators will be replaced by their condensates $\langle\bar{q}q\rangle$, giving rise to π and η mesons

$$\mathcal{L}_{eff} = \frac{f_\pi^2}{4}\text{Tr}[\partial_\mu U\partial^\mu U^\dagger],\ U = \exp\left(i\frac{\tau_i\pi_i + \eta}{f_\pi},\right). \tag{2.13}$$

[2]Sometimes also refered as PQWW (Peccei-Quinn-Weinberg-Wilczek) theory taking into account all three papers [20][21][22] which it preceded.

τ_i here are the Pauli matrices and the product $\tau_i\pi_i$ is defined as

$$\tau_i\pi_i \equiv \begin{pmatrix} \pi^0 & \sqrt{2}\pi^+ \\ \sqrt{2}\pi^- & \pi^0 \end{pmatrix}. \tag{2.14}$$

The U transforms under $U(1)_{PQ}$ as

$$U \to U \begin{pmatrix} e^{i\alpha x} & 0 \\ 0 & e^{i\alpha/x} \end{pmatrix} \tag{2.15}$$

and hence only the $U(1)_A$ flavour symmetry is broken by the quark mass term (1.42), which is symmetric under $U(1)_{PQ}$ and gives

$$\begin{aligned} \mathcal{L}_{\mathcal{M}} &= -\frac{f_\pi^2 M_\pi^2}{2}\mathrm{Tr}[UA\mathcal{M} + (UA\mathcal{M})^\dagger], \text{ with} \\ A &= \begin{pmatrix} e^{-i\frac{a}{v_F}x} & 0 \\ 0 & e^{-i\frac{a}{v_F}\frac{1}{x}} \end{pmatrix}, \ \mathcal{M} = \begin{pmatrix} \frac{m_u}{m_u+m_d} & 0 \\ 0 & \frac{m_d}{m_u+m_d} \end{pmatrix}. \end{aligned} \tag{2.16}$$

We already know there is also the anomalous term breaking both $U(1)_A$ and $U(1)_{PQ}$, responsible for the correction of the mass of the η meson as well as giving a mass to our axion and the a-π and a-η mixing

$$\mathcal{L}_{anomaly} = -\frac{M_\eta^2}{2}\left[\eta + \frac{f_\pi}{v_F}\frac{1}{2}\left(\frac{N_f}{2} - 1\right)\left(x + \frac{1}{x}\right)a\right]^2. \tag{2.17}$$

Combining both previous contributions one gets the axion mass as

$$m_a = \frac{N_f}{2}\left(x + \frac{1}{x}\right)\frac{f_\pi}{v_F}m_\pi\frac{\sqrt{m_u m_d}}{m_u + m_d} \tag{2.18}$$

and from mixing with π and η also the coupling to two photons from the EM anomaly

$$\partial_\mu J^\mu_{\mathrm{PQ}} = \frac{e^2}{24\pi^2}N_f\left(x + \frac{1}{x}\right)F_{\mu\nu}\tilde{F}^{\mu\nu} \tag{2.19}$$

$$\mathcal{L}_{a\gamma\gamma} = g_{a\gamma\gamma}a_{phys}F_{\mu\nu}\tilde{F}^{\mu\nu} = \frac{e^2}{32\pi^2}N_f\left(x + \frac{1}{x}\right)\frac{m_u}{m_u + m_d}\frac{a_{phys}}{f_a}F_{\mu\nu}\tilde{F}^{\mu\nu}. \tag{2.20}$$

As this model gives the SSB scale of $U(1)_{PQ}$ coincident with the electroweak SSB scale $f_a = v_F$, all the above variables have fixed values. However, these were quickly excluded by experiments and other models came to the fore as in principle the SSB scale might be at much higher energies $f_a \gg v_F$. Then the coupling would be much weaker and axions would be very light, so-called *invisible axions*, which was later realized makes them perfect candidates for the dark matter (DM).

2.1.2 Invisible axions

There are in principle two mechanisms how to extend the original PQWW model to shift the f_a at higher energies, which can be collectively called the *hadronic models* and the *non-hadronic models*.

The Kim-Shifman-Vainshtein-Zakharov [28] [29] (KSVZ) model was the first hadronic model proposal. It expands the SM with a heavy quark Q and an additional complex Higgs scalar σ both are weak-interaction-singlets and are symmetric under $U(1)_{PQ}$. The describing Lagrangian can be expressed in a form

$$\mathcal{L}_{KSVZ} = i\bar{Q}\gamma^\mu D_\mu Q + \partial^\mu \sigma^\dagger \partial_\mu \sigma - h(\bar{Q}_L \sigma Q_R + \bar{Q}_R \sigma^\dagger Q_L) + m^2 \sigma^\dagger \sigma - \lambda(\sigma^\dagger \sigma)^2. \quad (2.21)$$

The $U(1)_{PQ}$ is spontaneously broken by the $f_a = \langle \sigma \rangle = m/\sqrt{2\lambda} \gg v_F$, so the quark Q gets a mass $m_Q = h f_a$ and the complex field σ in (2.21) gives a rise to a scalar state from its radial part with a mass $m\sqrt{2}$ and a pseudoscalar state a from its phase. The anomalous triangle gives then

$$\mathcal{L}_{anomaly} = -\frac{M_\eta^2}{2}\left[\eta + \frac{a_{phys}}{2f_a} a\right]^2 \quad (2.22)$$

and thus a mass m_a and axion-photon coupling $g_{a\gamma\gamma}$

$$m_a = 6.3 \text{ eV}\left(\frac{10^6 \text{ GeV}}{f_a}\right), \; g_{a\gamma\gamma} = \frac{e^2}{32\pi^2}\frac{2}{f_a}\left(3e_Q^2 - \frac{4m_d + m_u}{3(m_u + m_d)}\right), \quad (2.23)$$

where e_Q is the EM charge of the quark Q.

In the case of non-hadronic models the Dine-Fischler-Srednicki-Zhitnisky [30] [31] (DFSZ) model was the first one. It adds to the PQWW model (i.e. to the two scalars ϕ_1 and ϕ_2) a new scalar ϕ transforming under $U(1)_{PQ}$, which $\langle \phi \rangle = f_a \gg v_F$. One gets similar results to the KSVZ model, when one rescales $f_a \to f_a/N_f$, the axion mass is given by the same expression as in the former case and the coupling to photons is given by

$$g_{a\gamma\gamma} = \frac{e^2}{32\pi^2}\frac{2}{f_a}\left(\frac{4}{3} - \frac{4m_d + m_u}{3(m_u + m_d)}\right). \quad (2.24)$$

2.2 Axion-Like Particles

In principle one can access the whole $(g_{a\gamma\gamma}, m_a)$ parameter space in a model independent way as the role of elementary pseudoscalars might be much more general then the above proposed solutions to the Strong CP problem. Due to the fact that the nature of these pseudoscalars is very similar to axions (they are usually remnants of a breaking of some $U(1)$ symmetry, they couple predominantly to photons, etc.) a generalization called *axion-like particles* (ALPs) will be used in the rest of the text. Based on the results of the previous section, a general interaction Lagrangian can be assumed

$$\begin{aligned}\mathcal{L}_{ALP}^{int} = {} & g_{a\gamma\gamma} a F_{\mu\nu}\tilde{F}^{\mu\nu} + \bar{g}_{a\gamma\gamma} a F_{\mu\nu} F^{\mu\nu} + g_{af\bar{f}} a \sum_f i\bar{f}\gamma_5 f + \bar{g}_{af\bar{f}} a \sum_f \bar{f} f \\ & + g_{a\gamma f\bar{f}} a F_{\mu\nu} \sum_f i\bar{f}\sigma^{\mu\nu}\gamma_5 f + \ldots\end{aligned} \quad (2.25)$$

The breaking of $U(1)$ symmetries is a common phenomenon in many theories beyond the SM (if not in most of them), so only the most usual examples will be

presented here: *majorons* connected with the breaking of the lepton number and *familons* connected with the breaking of the family number.

One of the first ideas of majorons came in [32], where neutrinos are considered to be Majorana particles and hence breaking the lepton number, but unlike in the usual approach the lepton number is broken spontaneously. In the case of familons, where the flavour symmetries are spontaneously broken a general approach was discussed in [33].

2.2.1 Kaluza-Klein axions

Many of the unified field theories follow the idea behind the Kaluza-Klein theory, where the space-time in which the theory is postulated is made of a tensor product of the 4-dimensional Minkowski space-time (or a pseudo-Riemannian manifold in general) and a manifold geometrically reflecting given symmetries. At low energies, this manifold can be seen as compactified and the original action in the higher dimensional space-time gives rise to gauge fields in four dimensions obeying the symmetries of the compactified manifold[3] and extra modes which decouple from these gauge fields are not observable in four dimensions.

In late 90's it was realized that the size of some dimensions need not to be as small as Planck length ($\sim 10^{-35}$ m) and instead could have the right size to solve the hierarchy problem [35]. This new approach has influenced also other theories beyond the SM even if they have a different original motivation. Axions, which in models built in previous section 2.1 seek for a mechanism putting the SSB scale f_a into high values, are one such case. Thus, could have the similar solution to the gravity as they would propagate into our 4 dimensions as Kaluza-Klein particles [36].

Meanwhile a different strategy, much more similar to the original KK one, was followed during the years and it was shown that by a reduction about more than one dimension also non-Abelian gauges can be restored [37]. Most of the unification schemes of today try to restore the whole $SU(3) \times SU(2) \times U(1)$ SM gauge group, which corresponds to a manifold of at least seven compact dimensions. In such theories the cases of ALPs as presented above (majorons, familons, ..) have a much more general character, which supports an idea that a lot of ALP modes could appear in the spectrum independently. A similar dimensional reduction scheme follow also string theories, where ALP modes (besides the axion one [38]) appear very naturally as KK zero modes of antisymmetric tensor fields or more similarly to the previous case as open strings on D-branes. The plenitude of ALPs in string theory is recently being referred as a *string axiverse* [39] and predicts ALPs in experimentally reachable regions.

[3]The original KK theory assumed the simplest topological manifold, the circle, and a 5-dimensional metric incorporating the 4-dimensional metric, the EM 4-potential and an additional scalar field. As a result of the compactification it restored from the unified equation the general relativity equations and the QED, where the $U(1)$ symmetry corresponded to the transformations in the compactified dimension. The theory however failed in the prediction as, when incorporating the fermionic field corresponding to the electron with the given electric charge, it predicted an incorrect value of the electron mass [34].

2.2.2 Cosmological implications

As already mentioned in the previous section 2.1, axions or ALPs are perfect DM candidates and thus one has to take into account the corresponding cosmological phenomena most of which are model-dependent. This presents a very wide topic nicely reviewed e.g. in [40]. Only a few generic instances derived for QCD axions will be presented here for the convenience of description of cosmological restrictions in the following chapter. The case of hot axions created and annihilated in the primordial soup influences also the amount of observable matter as in the early universe they couple predominantly to gluons and the corresponding restrictions from observations will be presented in the following chapter. The population of hot axions, however, might have been wiped out by the inflation unless they are reheated. Thus, the case of cold axions will be mainly discussed furher.

There are two general scenarios differing the production of cold DM (CDM) axions in the early universe as discussed in [41]. In the first case the $U(1)_{PQ}$ symmetry was spontaneously broken at energy f_a after the inflation and in the second one before or during the inflation.

In the post-inflation scenario, a network of one-dimensional topological defects (cosmic strings) creates and consequently starts disintegrating by the emission of massless axions, which at temperatures below the QCD scale obtain mass by the instanton (anomalous) term 2.17 as discussed in the section 2.1.1 and the axion potential takes a periodic form

$$V(a) = m_a^2 f_a^2 [1 - \cos(a/f_a)]. \tag{2.26}$$

Since the potential (2.26) has infinitely many minima, the axion field settles down to a different minima around the universe as it cools down and gets divided into domains separated by quasi-stable domain walls attached between cosmic strings creating string-domain network.

In fact, the instanton effects break the $U(1)_{PQ}$ symmetry into a discrete subgroup, $Z(N)$ symmetry, as $f_a = v_a/N$. The spontaneously broken $Z(N)$ symmetry implies N degenerate vacua and the further development of string-domain network varies for $N = 1$ and for $N > 1$.

- For $N = 1$ the domain walls are quantum-mechanically unstable and decay into axions giving significant contribution to the matter density of the universe.
- For $N > 1$ the domain walls are stable giving rise to extra acceleration to the universe expansion. One could identify this expansion with the observed one. Nevertheless, such universe would be less homogeneous than is observed, which became known as the *domain wall problem*. This problem is solved for $N = 1$ or if the $Z(N)$ symmetry is somehow explicitly broken or in the pre-inflation scenario discussed further.

In the pre-inflation scenario, the inflation expands 'our' domain into larger size than is the present observable universe and thus there is no domain wall problem and the current axion density is given by coherent oscillation of the axion field.

3. Searches for ALPs

Most of the searches for ALPs stand on the coupling of ALPs to two photons $g_{a\gamma\gamma}$[1], giving the decay width (in leading order) for a simple two-body decay as

$$\Gamma(a \to \gamma\gamma) = \frac{g_{a\gamma\gamma}^2 m_a^3}{64\pi}. \tag{3.1}$$

The approach how to measure the decay, however, varies a lot throughout distinct sections of the parameter space, see figure 3.1. Several experimental approaches will be outlined here together with some representing experiments, a comprehensive review presents e.g. [42].

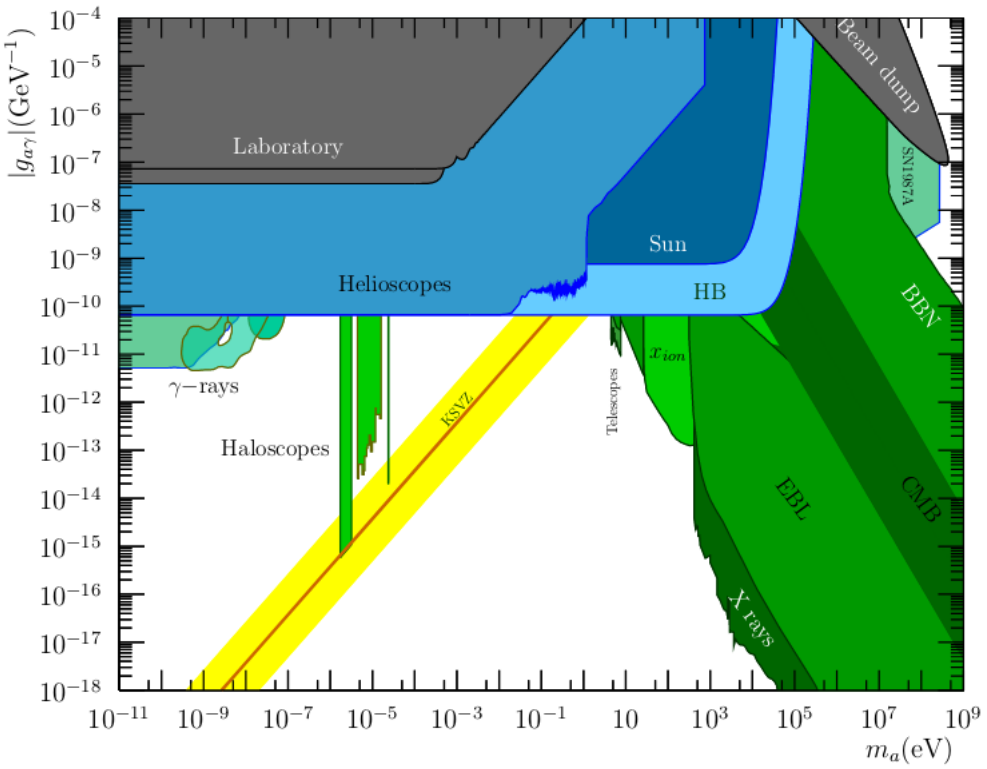

Figure 3.1: Current coverage (excluded regions with 95% C.L.) of the $(g_{a\gamma\gamma}, m_a)$ parameter space from the summary of [42].

Apart from experimental searches there are also cosmological constraints implied by effects already discussed in the previous section 2.2.2 as well as appearing naturally due to the coupling to the observable matter, which will be briefly sketched here. Based on the current knowledge of the universe evolution and astrophysical observations the ALPs with a high mass but a small coupling are generically ruled out by cosmological bounds 3.1. Among the most constraining effects are:

[1]There are of course many other possibilities, yet the coupling to two photons is probably the most pratical one and in most of the models also the dominant one.

- Big Bang Nucleosynthesis (BBN) - mostly coming from the D/H ratio as well as the n/p ratio giving rise to the ^{4}He;
- Cosmic Microwave Background (CMB) - there cannot be distortions in the CMB spectrum;
- Extragalactic Background Light (EBL) - photons produced in ALP decays cannot exceed extragalactic background light;
- X-rays, γ-rays - peaks in galactic spectra coming from ALP decays cannot exceed the background;
- Star evolution - too strongly coupled ALPs would cause faster star evolution than is observed[2].

3.1 Dark matter experiments

According to [43], the local dark matter halo density is $\rho = 0.2{-}0.56$ GeV cm^{-3} and in a case that this halo is made of ALPs, they might be directly measured by a conversion into two photons in a magnetic field by so-called *axion haloscopes* as proposed in 1983 by Siskivie [44].

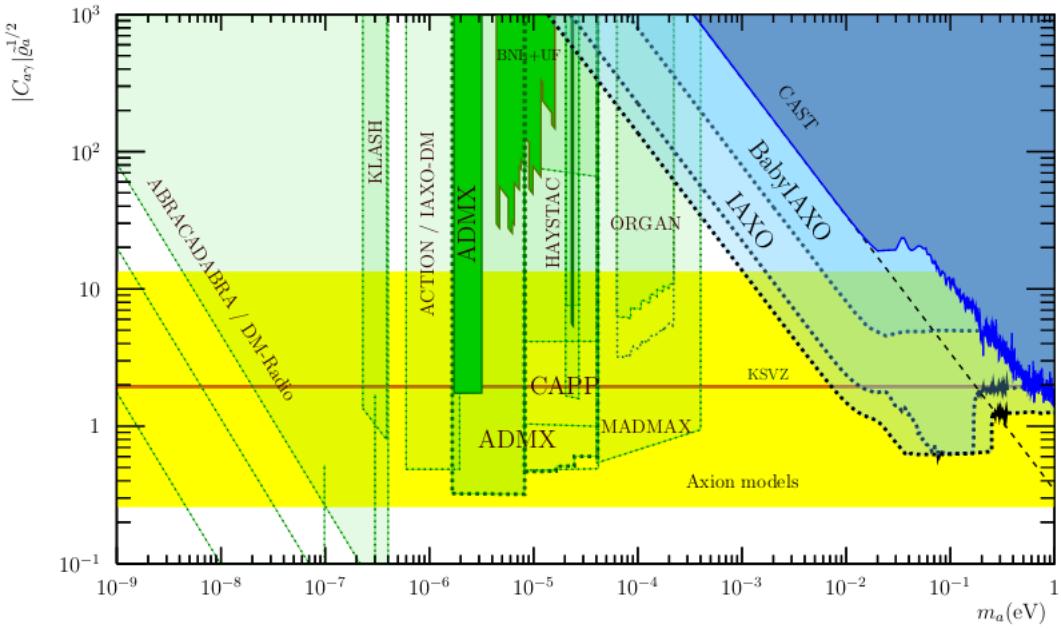

Figure 3.2: Curent limits from haloscopes (dark green) and proposed ones (semi-transparent green) in parameter space expressed in terms of $|C_{a\gamma}|\sqrt{\bar{\rho}_a}$, where $C_{a\gamma} = g_{a\gamma\gamma} f_a (2\pi/\alpha)$ and $\bar{\rho}_a$ is local axion DM density [42].

The technique assumes that DM axions are non-relativistic and hence produce monochromatic photons of energy given by the mass of ALP. Using microwave

[2]This holds mostly for Sun. There are in fact energy losses e.g. in the evolution of white dwarfs and for which ALPs might be responsible and hence gives us a hint where to look for ALPs in the parameter space.

cavities the signal can be enhanced by a quality factor Q when the resonant frequency of the cavity matches the axion mass. By tuning of the resonant frequency one can thus scan the mass spectrum with an immense sensitivity. The results of the ADMX Collaboration [45] have proven the possibility of reaching regions of coupling for axion masses yet inaccessible by other measuring techniques, see figure 3.2.

3.2 Solar axions

The expected predominant production of ALPs in Sun is by the Primakoff conversion of plasma photons in the EM field of charged particles giving the solar axion flux at the Earth surface $\Phi_a = g_{a\gamma\gamma}^2 3.75 \times 10^{31} \mathrm{GeV}^2 \mathrm{cm}^{-2} \mathrm{s}^{-1}$ [46]. The most promising method to measure solar axions are the axion helioscopes, where the incoming axion flux is converted to a flux of X-rays in presence of a transverse magnetic field B. If the background is static the energies of photons are given by energies of incoming axions, where the expected energy is of a few keV. The probability of axion conversion is given by [42]

$$\mathcal{P}(a \to \gamma) = 2.6 \times 10^{-17} \left(\frac{g_{a\gamma\gamma}}{10^{-10} \mathrm{GeV}^{-1}} \right)^2 \left(\frac{B}{10\mathrm{T}} \right)^2 \left(\frac{L}{10\mathrm{m}} \right)^2 \mathcal{F}(qL), \tag{3.2}$$

where L is length of the magnet coil (in meters) and the form factor reflecting the coherence of conversion goes as

$$\mathcal{F}(qL) = \left(\frac{2}{qL} \right)^2 \sin^2 \left(\frac{qL}{2} \right), \quad q = k_\gamma - k_a. \tag{3.3}$$

Case for $qL << 1$ gives a coherent conversion along the whole length $\mathcal{F} = 1$ and $q \simeq m_a^2/2\omega$ and is satisfied for masses $m_a \lesssim 10^{-2}$ eV[3].

The state of art presents the CERN Axion Solar Telescope (CAST), described in the following figure 3.3, which provided the current average limit $g_{a\gamma\gamma} \lesssim 2.3 \times 10^{-10}$ GeV^{-1} (95% C.L.) for 0.02 eV $< m_a <$ 0.64 eV and then about $g_{a\gamma\gamma} \lesssim 3.3 \times 10^{-10}$ GeV^{-1} (95% C.L.) for 0.64 eV $< m_a <$ 1.17 eV with ^{3}He buffer filling gas [47].

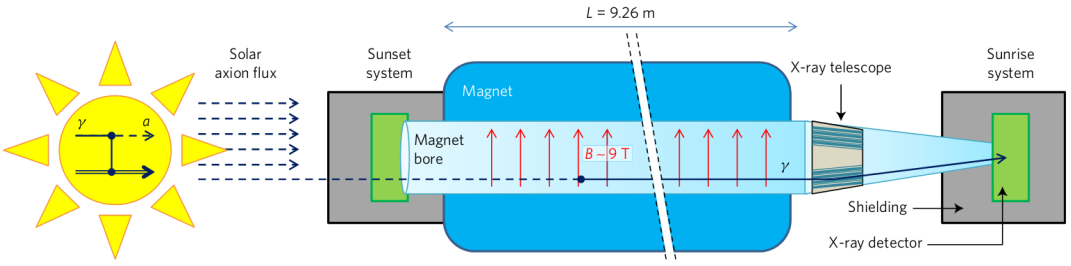

Figure 3.3: Sketch of the CAST helioscope from [48].

The next generation of helioscopes, namely IAXO [49], will go even further to the region $g_{a\gamma\gamma} \sim 10^{-11}$, see figure 3.4.

[3]The sensitivity of the experiment decreases with masses $m_a > 10^{-2}$ eV as $(2/qL)^2 \propto 1/m_a^4$.

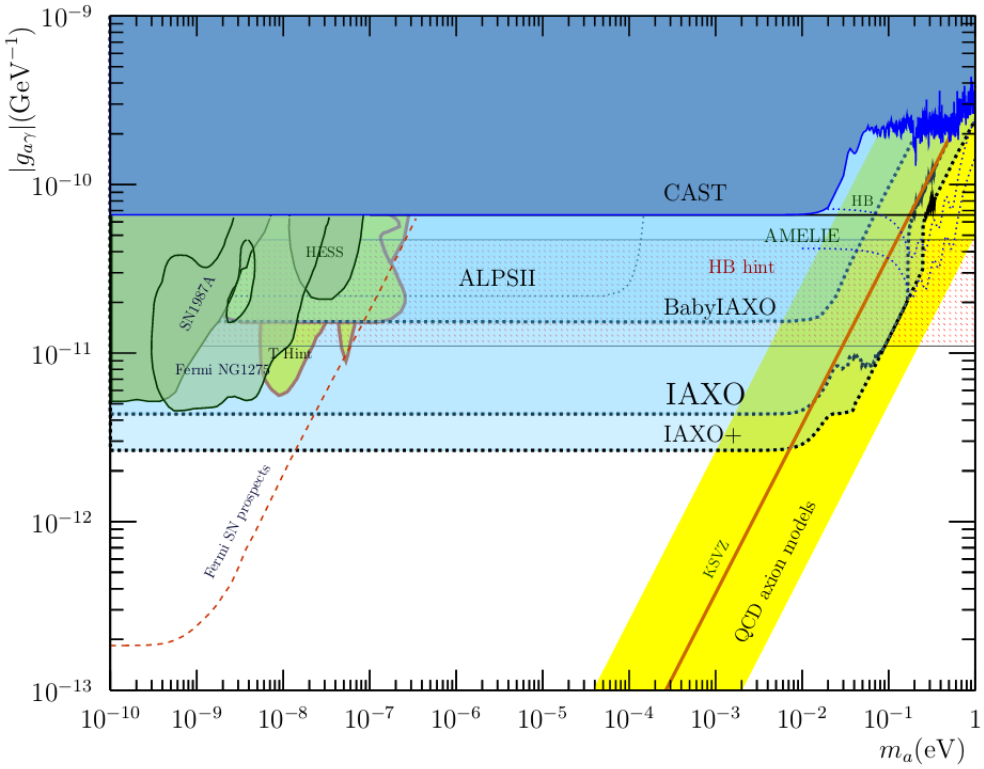

Figure 3.4: Curent limits from helioscopes (dark blue) and proposed ones (semi-transparent blue) [42].

3.3 Laboratory experiments

Apart from astrophysical sources, there are options how to measure possible effects of axions purely from terrestrial sources in laboratory. One of the options is using the same process for the creation of ALP as for its decay, the photon regeneration in magnetic field $\gamma+\gamma^* \to a \to \gamma+\gamma^*$ in an experimental setup based on so-called *light-shining-through-wall* (LSW) technique. In LSW experiment a high-energy laser is used as a source of photons, which are exposed to a strong transversal magnetic field, the flux is then shielded by a wall and again exposed to a magnetic field and possible regenerated photons are measured by the detector. The probability of LSW can be then written as

$$\begin{aligned}\mathcal{P}(\gamma \to a \to \gamma) &= \mathcal{P}(\gamma \to a)\mathcal{P}(a \to \gamma) \\ &= \left[\left(\frac{g_{a\gamma\gamma}B_e L_P}{2}\right)^2 \mathcal{F}_P\right]\left[\left(\frac{g_{a\gamma\gamma}B_e L_R}{2}\right)^2 \mathcal{F}_R\right],\end{aligned} \tag{3.4}$$

where form factor is defined as in the former case (3.3). The technique has been improved by adding Fabry-Perot cavities into the magnetic field, see picture 3.5, enhancing the transition probability by a factor $\beta_P\beta_R$. The factor β_P corresponds to the amplification of the right-moving photon wave when the cavity is in resonance and the second factor β_R is given by the coherent detection of the ALP field, together giving

$$\mathcal{P}(\gamma \to a \to \gamma) = \left[\left(\frac{g_{a\gamma\gamma}B_e L_P}{2}\right)^2 \mathcal{F}_P\beta_P\right]\left[\left(\frac{g_{a\gamma\gamma}B_e L_R}{2}\right)^2 \mathcal{F}_R\beta_R\right]. \tag{3.5}$$

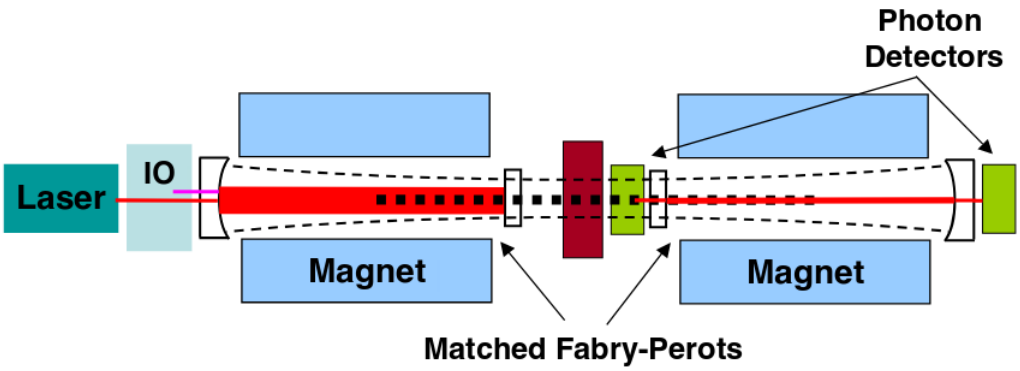

Figure 3.5: The principle of LSW experiment [50].

The most current limits coming from LSW experiments are from an ongoing experiment OSQAR $g_{a\gamma\gamma} \sim 10^{-8}$ [51], much further up to the region $\sim 10^{-11}$ will go the future experiment ALPS-II in its final stage [52].

Apart from the LSW experiments, another possibility how to use the axion-photon coupling for measurements is its influence on the light polarization [53]. A different approach offer experiments measuring possible ALP forces between baryons competing with gravity at distances $\sim 1/m_a$ [54].

3.4 Beam-dump experiments

ALPs are usually being taken as weakly interacting sub-eV particles (WISPs) as the case of heavy ALPs is usually ruled out by the nucleosynthesis (see figure 3.1). There is, however, a possible window at the MeV/GeV scale which is reachable by the collider beam-dump experiments, where the accelerated beam (electron or proton) is dumped in a target with a high proton number Z and produced ALPs would decay in the decay region covered by the detector. An experiment with the distance between the target and the detector comparable to the ALP decay length l_a would be most sensitive to ALPs. Mean proper lifetime $\tau = 1/\Gamma$ is given by (3.1) and for high energies $E_a \gg m_a$, thanks to the Lorentz boost (additional γ factor), the decay length is [55]

$$\begin{aligned} l_a = \beta\gamma\tau &= \frac{64\pi E_a}{g_{a\gamma\gamma}^2 m_a^4} \\ &\approx 40 \text{ m} \times \frac{E_a}{10 \text{ GeV}} \left(\frac{g_{a\gamma\gamma}}{10^{-5} \text{ GeV}^{-1}}\right)^{-2} \left(\frac{m_a}{100 \text{ MeV}}\right)^{-4}. \end{aligned} \tag{3.6}$$

For the fixed decay length measurable by the experiment, there is an obvious inverse dependence between m_a and $g_{a\gamma\gamma}$, giving the exclusion region of beam-dump experiments the typical prolonged shape.

There are several ways of the production of ALPs in beam-dump experiments:

- coherent scattering (elastic scattering: the beam proton on the target nucleus);

- incoherent scattering (inelastic scattering: the beam proton constituents on the target nucleus ones);
- non-perturbative processes (decays of hadrons).

The coherent scattering presents the dominant source of ALPs which are not directly coupled to quarks and the ALP production goes via the Primakoff process [56], effectively described by diagram 3.6. An advantage accompanying the coherent scattering is that it can be calculated perturbatively at low energies and hence provides very clean theoretical prediction.

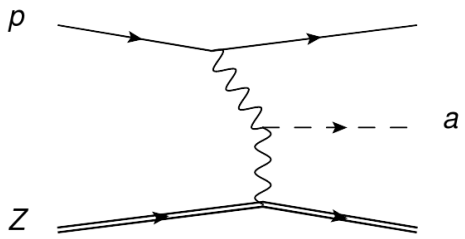

Figure 3.6: Primakoff production of ALPs in proton-nucleus collisions [55].

The current constraints are given mainly by experiments on electron-positron colliders (electron beam-dumps SLAC 137 and 141) and by CHARM and NuCal experiments with the proton beam, see figure 3.7. The data set in the case of CHARM is determined by $N_{POT} = 2.4 \cdot 10^{18}$ on a copper target and $N_{POT} = 1.7 \cdot 10^{18}$ on an iron target in the case of NuCal.

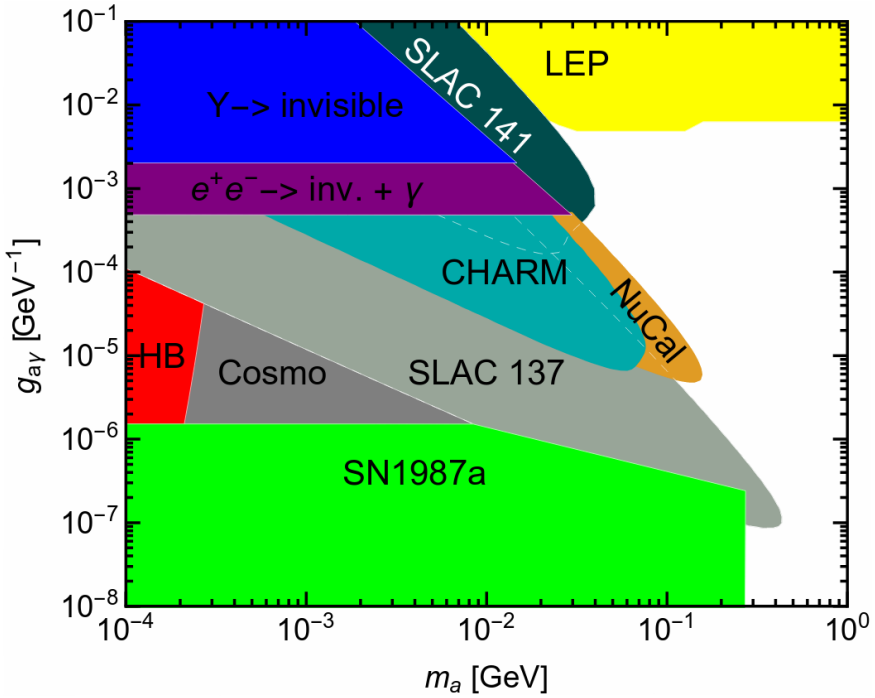

Figure 3.7: Current constraints in the ALP parameter space [55].

An ongoing research in the beam-dump mode is currently being performed at the NA62 experiment discussed in details in the following chapters. A notable

near-future experiment presents the SHiP, which will be made particularly for this kind of searches and will go well beyond the current limits, for details see the ShiP physics study [57].

Recently, a more detailed simulation of the production of ALPs in targets has been performed taking into account the contribution of secondary photons resulting from π^0 and η decays, giving even further reach of beam-dump experiments [58]. The corrected sensitivities of past and future experiments are projected in the following figure 3.8.

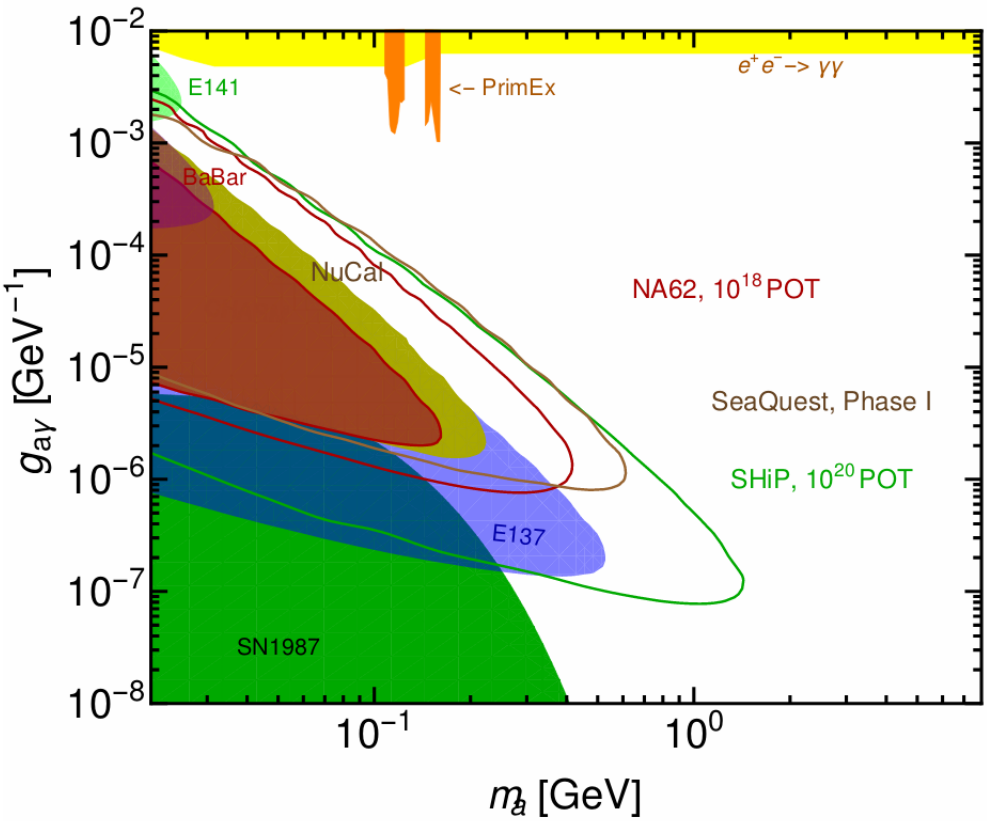

Figure 3.8: Corrected sensitivity of past and future searches [58].

4. Layout of NA62 experiment

The NA62 experiment is a fixed-target experiment[1] at CERN laboratory located on the border between France and Switzerland near Geneva. The European Organization for Nuclear Research known as CERN (Conseil Européen pour la Recherche Nucléaire) operates the largest particle physics laboratory in the world hosting a chain of accelerators. Each machine in the chain provides beams for its own experimental halls as well as for the next machine in the sequence.

Most of the experiments are provided with a proton beam. The proton source is a simple bottle of hydrogen gas and an electric field is used to strip hydrogen atoms of their electrons to yield protons. Linac 2 (linear accelerator), the first accelerator in the chain, accelerates the protons to the energy of 50 MeV. The beam is then injected into the Proton Synchrotron Booster (PSB), which accelerates the protons to 1.4 GeV, followed by the Proton Synchrotron (PS), which pushes the beam to 25 GeV. Protons are then sent to the Super Proton Synchrotron (SPS) where they are accelerated to 450 GeV and then injected to the two beam pipes of the LHC, where the nominal energy for each beam reaches 6.5 TeV [59].

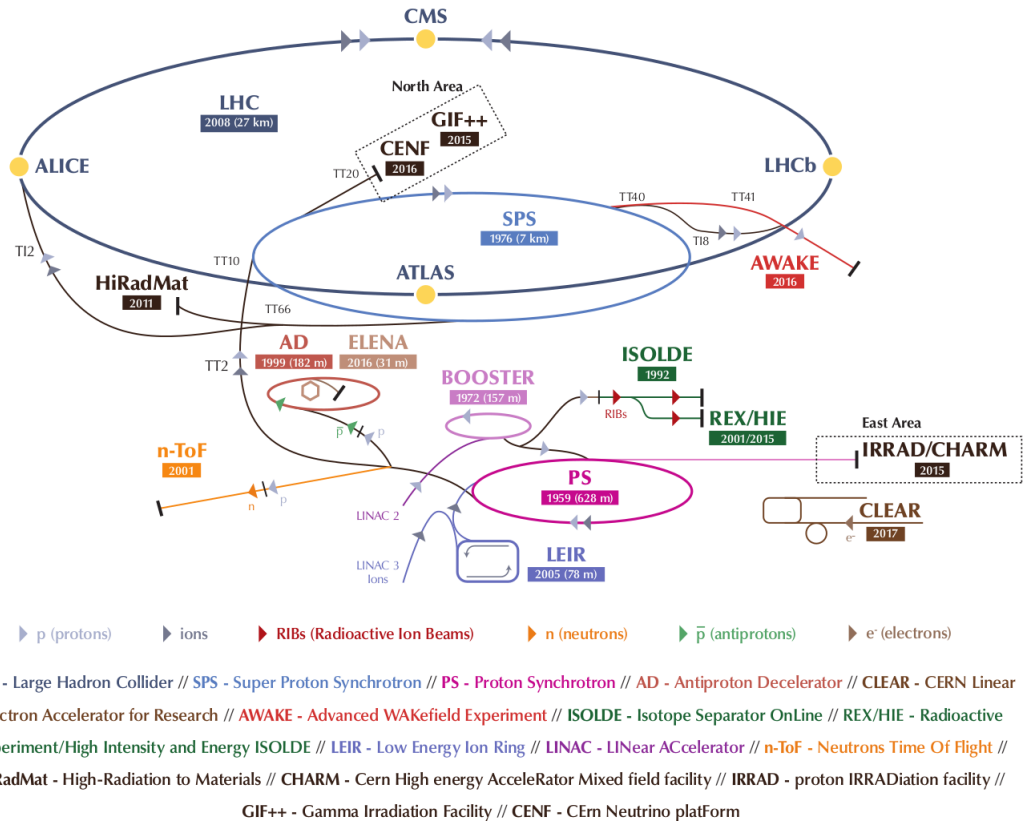

Figure 4.1: CERN's accelerators complex [59].

[1]Experiment where the particle beam is impinged onto a specific target and products of the interaction (constituents of the secondary beam) are studied.

4.1 The aim of NA62

The NA62 is one of the fixed-targed experiments located in the Prévessin (France) site, called North Area. The main purpose of the NA62 experiment is to study rare kaon decays, where in the present configuration the main goal is to measure the ultra-rare decay $K^+ \to \pi^+\nu\bar{\nu}$ [60]. The first observation of such decay in the data sample taken in 2016 has been published [61]. The data from 2017 and 2018 have yet to be analyzed.

The experimental site can be subdivided in three parts. The region where the secondary kaon beam is produced and adjusted. Then, the region where undecayed kaons are tagged and beam momentum is measured, called the 'upstream region', and finally the 'downstream region' where the decay products are identified and their momenta are measured, see the NA62 layout in the figure 4.2.

4.2 Beam line

The primary proton beam taken from the SPS accelerator passing T4 target ($\sim 10^{12}$ protons/s) at 400 GeV/c impinges beryllium target T10 and generates a secondary high-intensity (750 MHz) hadron beam containing about 6% of K^+. A triplet of radiation-hard quadrupole magnets (Q1, Q2, Q3) collects large angle of particles and is followed by an achromat selecting a beam momentum around 75 GeV/c. The archomat consists of four dipole magnets. The first two magnets displace the beam by 110 mm from the original axis and keep it parallel. Then the beam passes through a set of apertures so-called 'Target Attenuator eXperimental areas' (TAX) in a metallic beam-dump/collimator TAX1 and TAX2, which select momentum about 75 GeV/c and absorb unwanted particles. Next, two magnets of achromat return the beam onto the original axis. A following triplet of quadrupoles (Q4, Q5, Q6) focuses the beam and finally muons of both signs are swept aside using three 2 m long dipole magnets.

The beampipe then enters the experimental area, where in the 'upstream region' kaons in the beam are identified. Kaon momenta are further measuered before entering the 60 m long decay region in the first part of a 117 m long tank. The tank is evacuated down to $\sim 10^{-6}$ mbar and hosts the downstream spectrometer measuring charged tracks of the decay products. Besides the spectrometer, the whole tank is encircled by 11 veto detectors to detect all possible particles escaping the decay region in angles out of the acceptancy of the downstream detectors. After passing the downstream region at the end of the experimental hall, the beam is deflected by a magnet and absorbed in a beam dump. [60].

4.3 KTAG/CEDAR

As K^+ comprise about 6% of the beam, and the rest are mostly pions and protons which cannot be efficiently separated from the beam, there is a need for a particle identification detector. The first detector in the experimental hall is

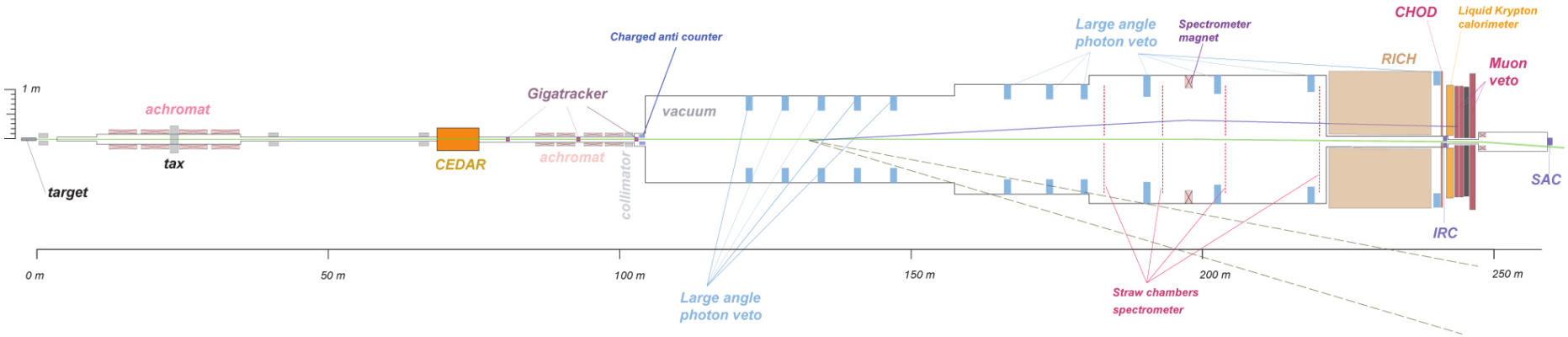

Figure 4.2: NA62 setup [60].

the CEDAR (Cherenkov Differential counter with Achromatic Ring), also called KTAG (Kaon tagger). The KTAG tags kaons very precisely with the time resolution below 100 ps and an efficiency of the kaon identification about 98% [60].

The CEDAR is filled with a nitrogen gas at the pressure about 1.7 bar. The amount of the material in the path of the beam can be further decreased by the use of hydrogen gas. This option was, contrary to the original proposal, ruled out due to safety reasons. For the given relativistic velocity of the beam, the angle of Cherenkov light is a function of the mass of a particle.

The Cherenkov light is reflected by a spherical mirror at the end of the vessel back on the diaphragm at the beginning, so only the light from a specific particle type has the right angle to reach the slit. There is a sequence of 8 quartz windows, lenses and spherical mirrors to transfer the light to 8 collecting sections of cones which can be seen on the figure 4.3. A coincidence of at least 6 of them indicate a passage of the kaon.

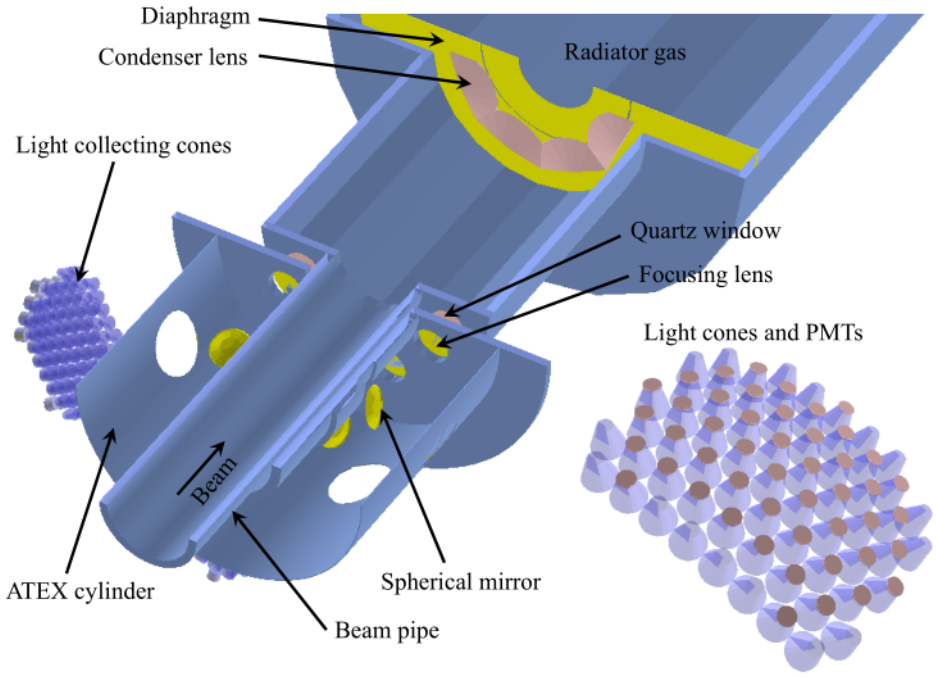

Figure 4.3: KTAG/CEDAR detector [60].

4.4 GTK

The following detector in the chain is the beam spectrometer called Giga-Tracker (GTK). The GTK is a silicon pixel spectrometer and measures the momentum, time and the outgoing angle of the passing beam. An exceptional accuracy is essential here as for the beam rate $\sim$ 750 MHz a hit time resolution below 200 ps is required.

The GTK consists of three stations with four dipole magnets among them. Each station is made of one silicon pixel detector with matrix of 18000 pixels on an area 63.1 $\times$ 29.3 mm. The matrix is read out by ten chips (further called

TDCpix) in two rows, each TDCpix is 40×45 pixels, see figure 4.4. As GTK is exposed to a high rate of radiation, the detector has to be cooled. Its lifetime can be also increased during the years by a higher bias voltage.

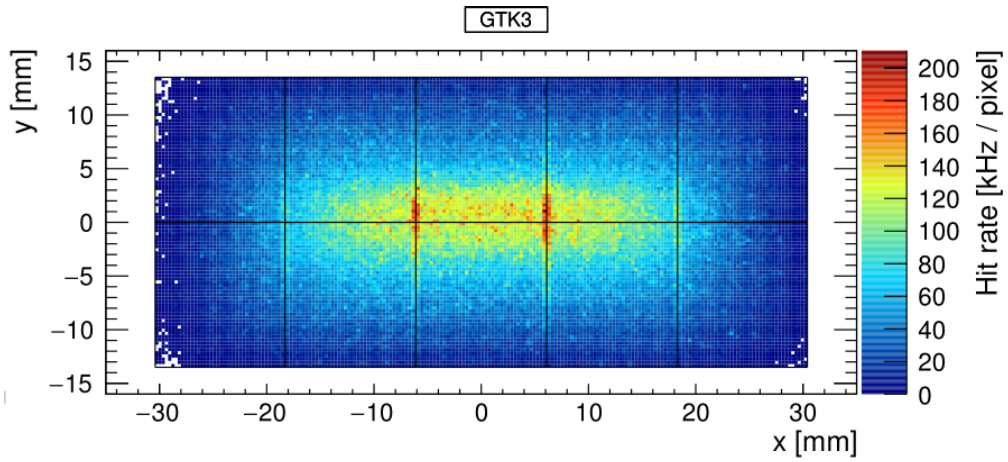

Figure 4.4: GigaTracker station [62].

The magnetic field from the dipole magnets deflects charged particles to the second station and back to the axis of the beam line, see figure 4.5. The layout is set to measure the momentum around 75 GeV/c. The real momentum can be derived from the particle displacement in the central station with respect to other two stations [62].

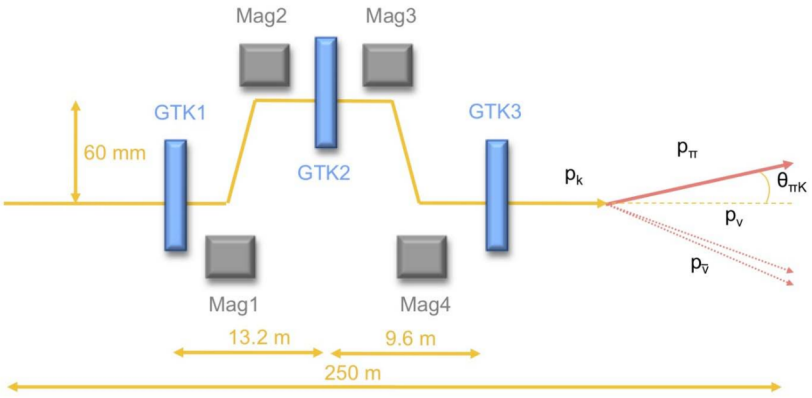

Figure 4.5: GigaTracker setup [62].

4.5 CHANTI

Particle interactions in the last GTK station are not swept away by the magnetic field like in the first two stations and can produce additional background in the downstream region. For this case there is the CHANTI (The Charged Anti-Coincidence Detector) placed between the GTK3 station and the beginning of the decay region.

The CHANTI consists of six hodoscope stations, each of 300×300 mm. A single station is made by 48 bars triangular in cross section. One plane of bars for X and one for Y coordinate, as can be seen in the figure 4.6. Each bar has a polystyrene scintillator with an optical fibre in the middle. Ends of the fibre are connected to photomultipliers and the signal from a possible incoming particle is detected.

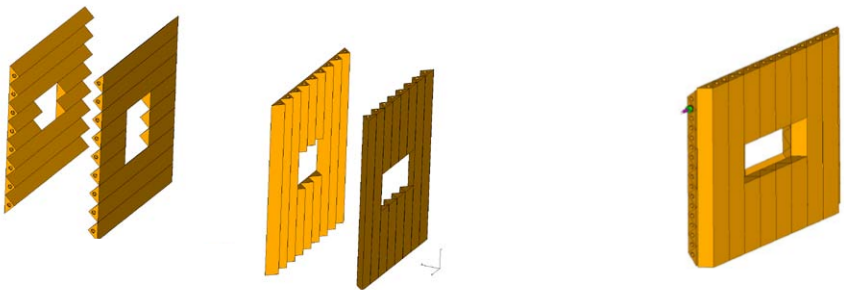

Figure 4.6: CHANTI station construction [63].

Single CHANTI stations locations are chosen to cover the acceptance of the decay region, so any possible inelastic interactions cannot make background, see figure 4.7. The first station is located 28 mm from the GTK3 station and is covered in the vessel with this last GTK station [63].

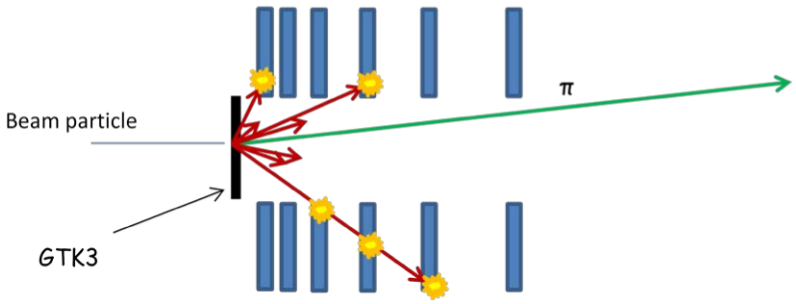

Figure 4.7: CHANTI detector layout [63].

4.6 Decay region and LAVs

About 18% of tagged kaons with momentum measured by the GTK decay in a 60 m long region in the first part of a circa 117 m long evacuated tank with the vacuum at pressure about 10^{-6} mbar. This part of the tank is also referred to as the 'blue tube' due to the cover colour. The beam is being slightly deflected in this long region by the so called 'blue field'[2], which has to be taken into account during the subsequent data analysis. Final reconstructed results of the track has to be corrected about $\Delta\theta \sim 35$ μrad for a 25 GeV/c track [64].

[2]The presence of the 'blue field' is mostly a consequence of the Earth magnetic field.

The decay region tube is widening with the beam with 1.92 m in the diameter at the beginning, widening to 2.8 m in the end. Because of the events where photons are radiated in wide angles (8.5 up to 50 mrad), LAV (Large Angle Veto) photon detectors are placed in the full length of the region, see figure 4.8. There are 11 LAV stations alongside the whole tank and a last twelfth LAV station operated in the air, about 3 m upstream of the calorimeter. The LAV station's diameter increases just as increases the diameter of the tube.

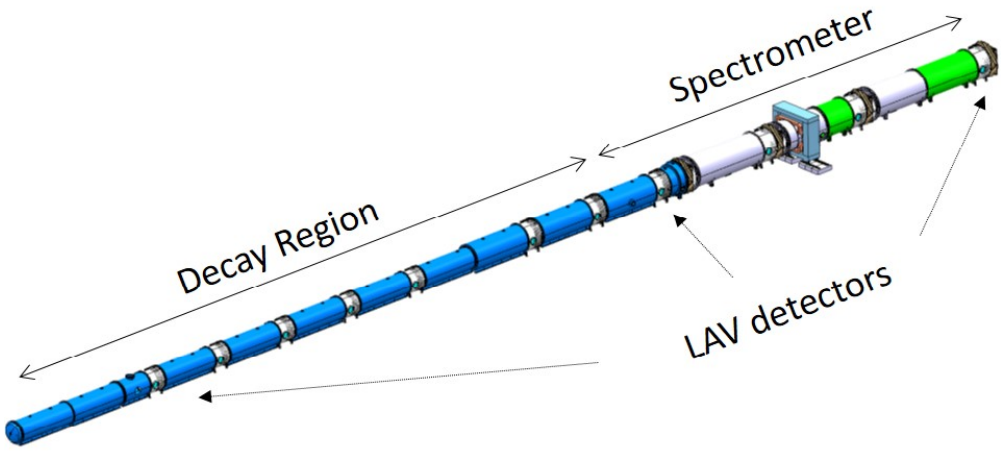

Figure 4.8: Decay region scheme [60].

For the setup of one LAV station, see figure 4.9. Each station has lead glass blocks arranged on the edge in several mutually shifted rows to cover the whole border of the station. A possible passing particle leaves an electromagnetic shower producing Cherenkov light. Each block is then read out by a photomultiplier.

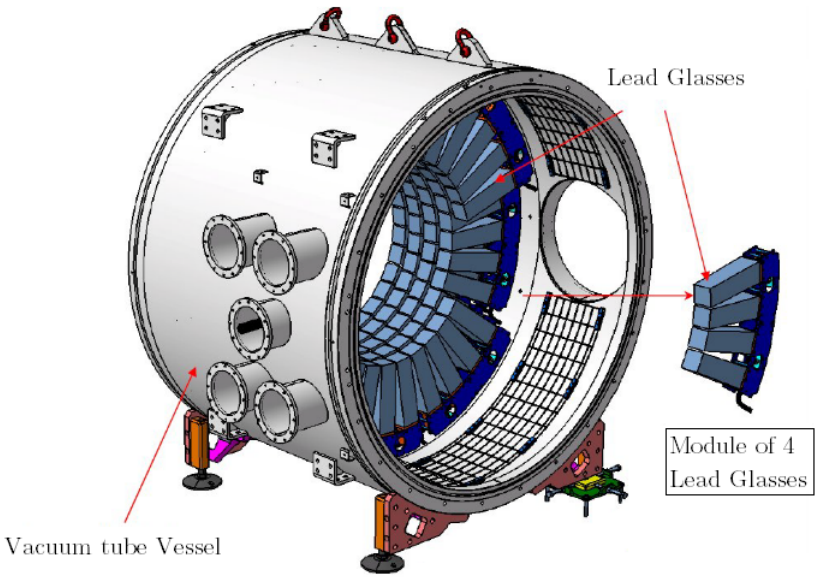

Figure 4.9: Complete station layout [64].

4.7 Straw Spectrometer

The Straw spectrometer occupies the last 35 m of the 117 m long evacuated tank and its purpose is to measure momenta of the decay products. As in the case of the GTK, a good accuracy is necessary to achieve the sufficient background rejection. The spectrometer has four identical stations, where the first station is placed 25 m downstream from the fiducial region, see figure 4.10. A large aperture dipole magnet (MNP33), providing vertical magnetic field of 0.38 T, is located between the second and the third station. The first and the last two stations provides vectors of the track of charged particles. The position vectors accompanied with the deflection from the magnetic field provides information about the particle momentum.

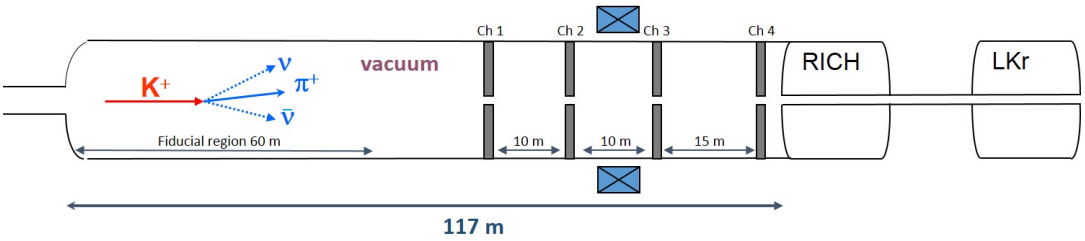

Figure 4.10: Straw spectrometer location [60].

Every station is composed of four planes, each plane giving a position in one axis perpendicular to the beam axis. The first two planes measuring the vertical (0°) and the horizontal (90°) position and another two planes rotated by 45°, see figure 4.11 on the left. Such layout provides more precise measurement of coordinate for one particle and prevents ambiguities when two particles hit the station at the same time [60].

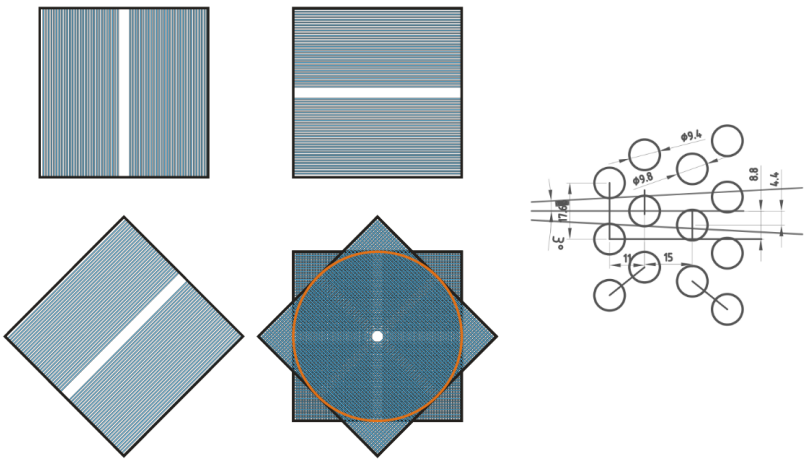

Figure 4.11: Left: Straw chamber layout. Right: Straws positioning in the plane [65].

Each plane consists of 1,792 straws, 2160 mm long about 9.82 mm in diameter and a 12 cm gap for the beam is left near the center. The straws are

staggered in four rows in the plane to cover all possible angles, as can be seen in the figure 4.11 on the right, and are made of a very thin (36 μm) PET foil to minimize the scattering. The straw chambers are placed in the vacuum tank while the straws are filled with a mixture of 30% of CO_2 and 70% of argon at the atmospheric pressure. Straws are coated from the inside by two metal layers (50 nm of copper and 20 nm of gold) as a cathode, and has a gold-plated tungsten anode wire in the middle with an electric field $\sim$ 1 kV between the anode and the cathode. The passing particle ionize the filling gas and the leftover charge is collected and processed by the front-end electronics [65].

4.8 RICH

The Ring Imaging Cherenkov Counter (RICH) is a downstream particle identification detector with a time resolution less then 100 ps. The RICH is a 17.5 m long cylindrical vessel (see figure 4.12) filled with the neon gas at a constant pressure of 990 mbar. The vessel has four sections with diameter increasing backwards against the direction of the beam. The entrance and the exit windows have a conical shape and are made of two and four mm thick aluminium, where the entrance window separates the vessel from the vacuum of the decay region [66].

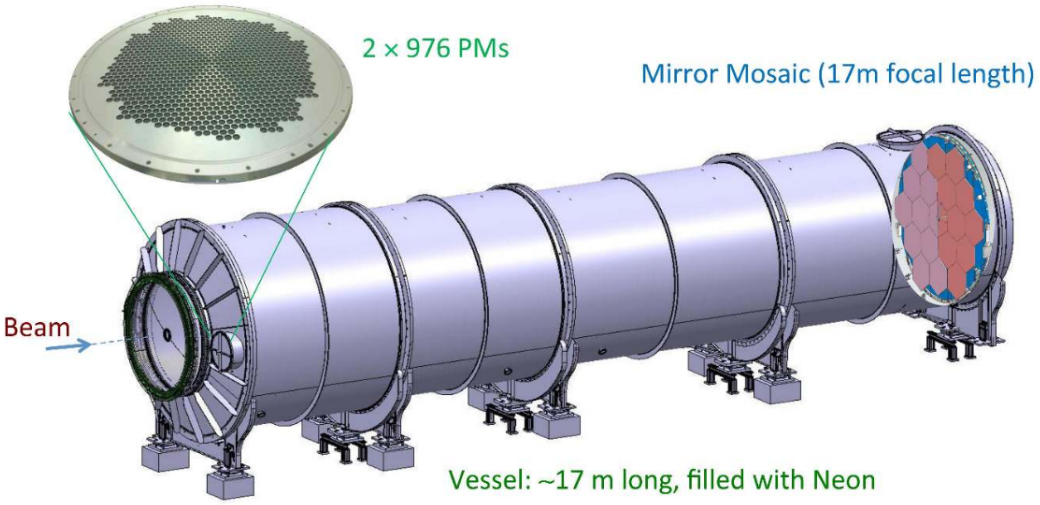

Figure 4.12: The RICH layout [60].

The RICH is designed to separate pions from muons between 15 and 35 GeV/c momentum, see the momentum resolution on the figure 4.13 on the left. To increase the resolution and to keep the photomultipliers out of the active area, the downstream end of the vessel of the 3.2 m diameter is filled with mosaic of 20 spherical mirrors which reflect the cone of Cherenkov light backwards onto the photomultipliers, see figure 4.13 on the right. Half of the mirrors points left and half right of the beam pipe. The inner side of the vessel is covered with black epoxy painting to avoid reflection of the Cherenkov light from it [66]. During 2014 - 2015 runs for 86% pion efficiency a 1.3% muon survival probability was observed in the 15-35 GeV/c range. The RICH yields an intrinsic event time resolution about 70 ps and hence is used as a referential time for charged tracks [60].

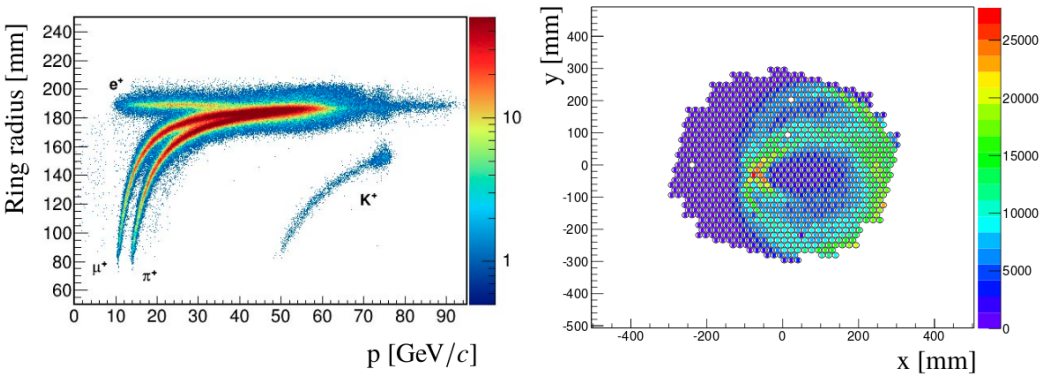

Figure 4.13: Left: Cherenkov ring radii for different particles. Right: Cherenkov light ilumination on the photomultipliers [60].

4.9 CHOD/NewCHOD

Charged particle hodoscopes (CHOD) are fast scintillator detectors providing the impact point position of a passing charged particle. There are two CHOD detectors, the New CHOD detector immediately behind the RICH, followed by the last LAV station and the original NA48-CHOD further downstream.

The NewCHOD is a single plane of 152 polystyren scintillator tiles, covering the radius from 140 to 1070 mm. All the tiles are 30 mm thick and mostly 200 mm or 135 mm wide[3] and are organized in rows with a mutual overlap 1 mm, as one can see in the following figure 4.14. The scintillation light is read out of each tile by two bundles of wavelength shifting (WLS) fibres coupled to silicon photomultipliers [67].

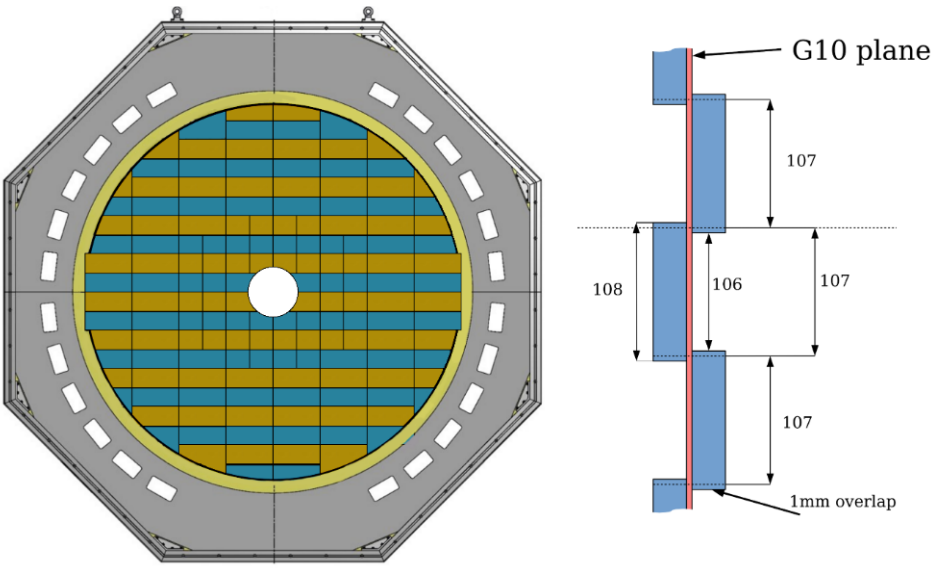

Figure 4.14: Left: Layout of rows on the support panel. Right: Layout of tiles in single rows [67].

[3]Smaller tiles are located around the beam pipe to sustain the higher hit rate.

The original NA48-CHOD has two planes of 64 scintillator slabs with photomultipliers on the ends and space left around the beam pipe, see 4.15. The NA48-CHOD posses worse efficiency for high intensity beams than the NewCHOD, yet it was left in the experiment and is used as a control detector. [60].

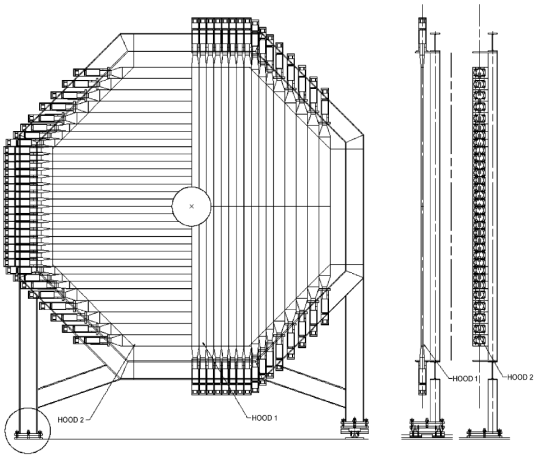

Figure 4.15: CHOD scheme [60].

4.10 LKr

The Liquid Krypton calorimeter (LKr) is an electromagnetic calorimeter, placed inside the cryostat filled with 9 m^3 of liquid krypton at 130 K. It presents a key part of the experiment enabling a precise photon detection with an inefficiency about 10^{-5}. The radius of the LKr is 128 cm, where first 8 cm are left for the beam pipe, see the following figure 4.16. The active area of LKr is composed of a single plane about 127 cm in depth (corresponding to 27 X_0), containing 13248 cells about 2×2 cm with Cu-Be electrodes [60].

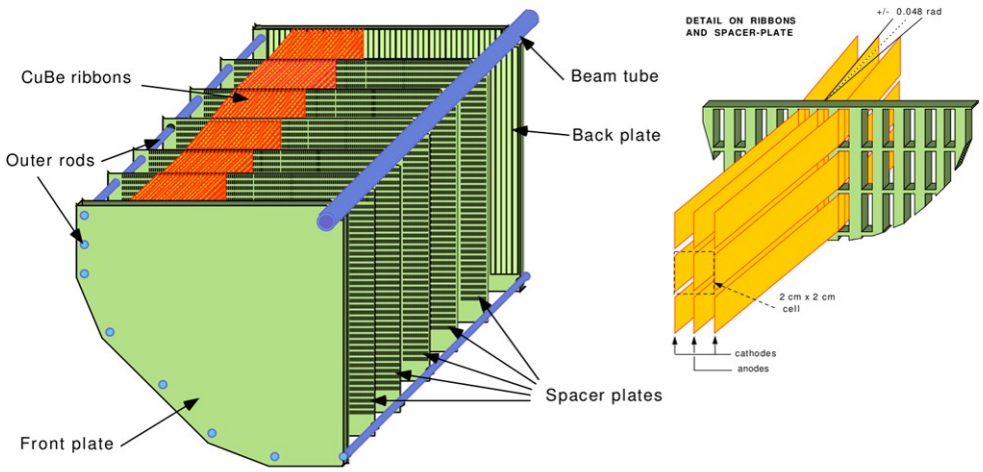

Figure 4.16: Left: One LKr quadrant layout, Right: LKr cells 'zig-zag' arrangement detail [60].

Alternating electrodes filling the plane are oriented with the beam axis but slightly deflected. They also change the direction of the deflection several times to avoid inefficiency for very flat tracks close to the anodes, see the figure 4.16 on the right. Electrodes are connected directly to the preamplifiers sending a signal to the readout electronics.

4.11 MUV

The muon veto (MUV) is a system of three independent detectors succeeding the LKr: hadronic calorimeters MUV1 and MUV2 and a fast muon veto MUV3. See the system layout in the following figure 4.17.

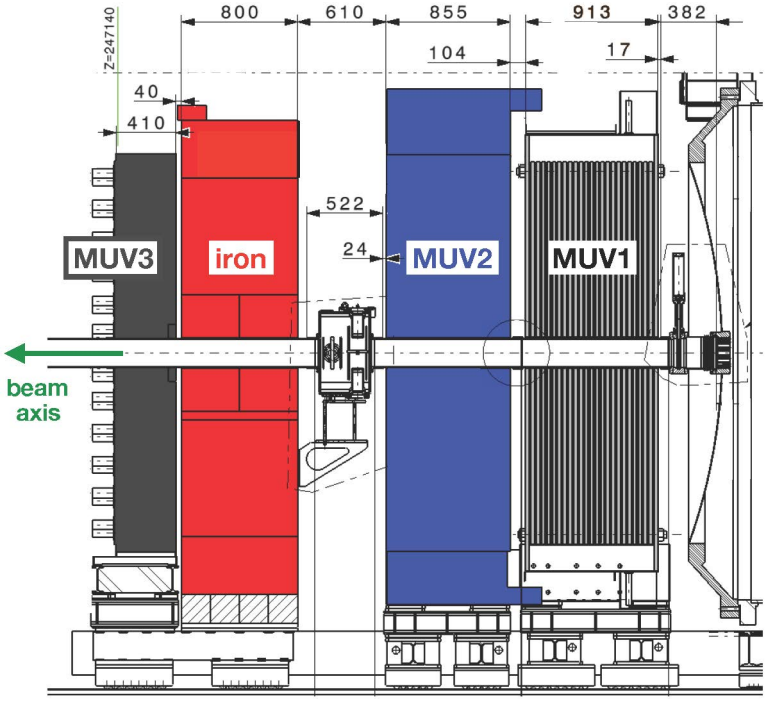

Figure 4.17: MUV detectors layout [60].

MUV1 and MUV2 are iron-scintillator sandwich calorimeters of twelve vertical and twelve horizontal layers of iron alternating with scintillator covering a plane of 260 × 260 cm and corresponding to $\sim 8\ X_0$. Each scintillator strip is 260×6 (or 4) $\times 1$ cm and is connected to photomultipliers through the WLS fibres in case of MUV1. The MUV2 is a refurbished original NA48 hadron calorimeter very similar to the new MUV1. It has readout photomultipliers connected directly to scintillators [60].

The iron wall of 80 cm is placed between the MUV2 calorimeter and the MUV3 muon veto and is thick enough to stop everything, but muons. MUV3 itself is composed of 22 × 22 cm tiles with two photomultipliers placed 21 cm behind each tile. They cover the angle for scintillation photons, but as they also detect Cherenkov radiation if a muon passes through the photomultiplier windows two photomultipliers are neccesary for a better timing [60].

4.12 Additional Veto Detectors

Two pairs of additional veto detectors are implemented in the experiment. The Small angle veto (SAV) system serves for detection of photons emitted at small angles close to the beam line out of the acceptance of the LKr. It is composed of the Small angle calorimeter (SAC) and the Intermediate ring calorimeter (IRC). Both detectors are of made of an alternating sequence of lead plates and scintillators (also referred to as the shashlyk type) read out by photomultipliers coupled through WLS fibres and both are of a similar construction outlined in the following figure 4.18. The IRC is placed between the CHOD and LKr and covers radia between 7 cm and 14 cm. The SAC is placed inside the beam vacuum towards the beam line when the charged part of the beam is swept to the beam dump, to detect the leftover photons in the beam line.

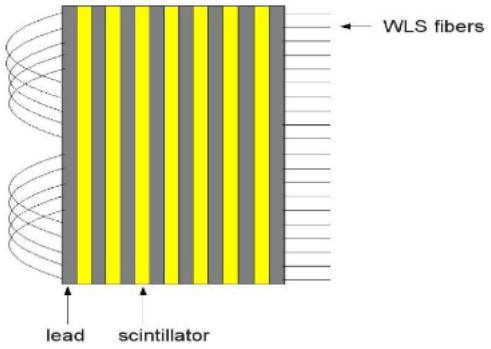

Figure 4.18: Shashlyk type detector [64].

The second pair of detectors serve for a detection of charged pions in the $K^+ \to \pi^+\pi^-\pi^+$ ($K_{3\pi}$) decays and consists of the peripheral MUV0 detector and the hadronic sampling calorimeter (HASC). The MUV0 is a single plane of two layers of scintilator tiles read out by photomultipliers via WLS (see figure 4.19 on the left) and detects π^- with momenta below 10 GeV/c deflected by the spectrometer magnet out of the acceptance of other downstream detectors.

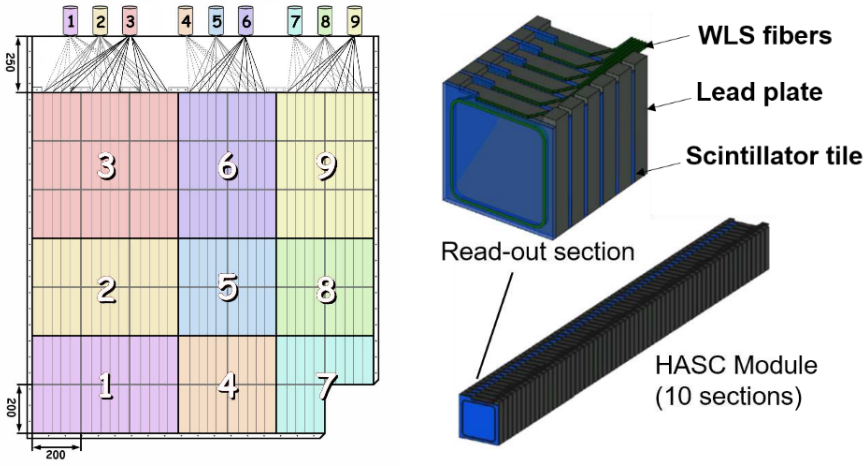

Figure 4.19: Left: Sketch of MUV0. Right: Layout of one HASC module [60].

The HASC on the other side detects π^+ above 50 GeV/c propagating through the beam line. These π^+ are deflected off-axis together with the charged component of the beam at the end of the beam line before the SAC detector. Unlike the 75 GeV/c beam, which is dumped, these π^+ hit the HASC as they have lower momentum [60]. The HACS is a sandwich calorimeter consisting of 9 identical modules. The layout of each module can be seen in figure 4.19 on the right.

4.13 Data taking

As mentioned at the beginning of the chapter, SPS provides the primary beam and sets its intensity by changing the position of beam selecting apertures at the T4 target[4]. The primary beam is not continuous but is split into 4.6 s long spills, so-called *bursts*, and its intensity on the T10 target is in the order of $\sim 10^{12}$ PoT/s [5]. The secondary beam generated at T10 has an intensity in the order of $\sim 10^8$ s^{-1} and has about $\sim 6\%$ of K^+.

During the data-taking period 2016-2018 the intensity has been gradually increased with a better understanding of the detector readout logic response. It is expected that the intensity could be even higher in the next data-taking period (starting in 2021) if the signal-to-background ratio (S/B) is kept at an acceptable level. For the declared intensity, one burst usually corresponds to about $3 \cdot 10^5$ measured events, where the selection of well-measured events is provided by the trigger and data acquisition system, which will be discussed further in the following chapter.

[4]The beam has a gaussian profile, hence a lower intensity subset of the beam can be chosen.
[5]PoT or N_{POT} means protons-on-target.

5. Readout and TDAQ system

The high beam rate of decays up to 10 MHz in the detector dictates a need for a high-performance trigger system to maximize the high quality data collection, for which a unified trigger and data acquisition (TDAQ) system is used at NA62. The TDAQ system is composed of the readout (section 5.1), a single hardware trigger level L0 (section 5.2) and high level software triggers (section 5.3).

The L0 trigger decision is stated by the *L0 Trigger Processor* (L0TP), reducing the data flow by factor of 10, based on the *trigger primitives* generated by the readout of single detectors. The higher level software triggers are performed at the PC-farm. Both levels together reduce the data rate down to 10 - 100 kHz, which meets the bandwidth of the data flow for the permanent storage tapes. The data passing all the trigger levels are written on the disk by the Central Data Recording (CDR) service, see figure 5.1.

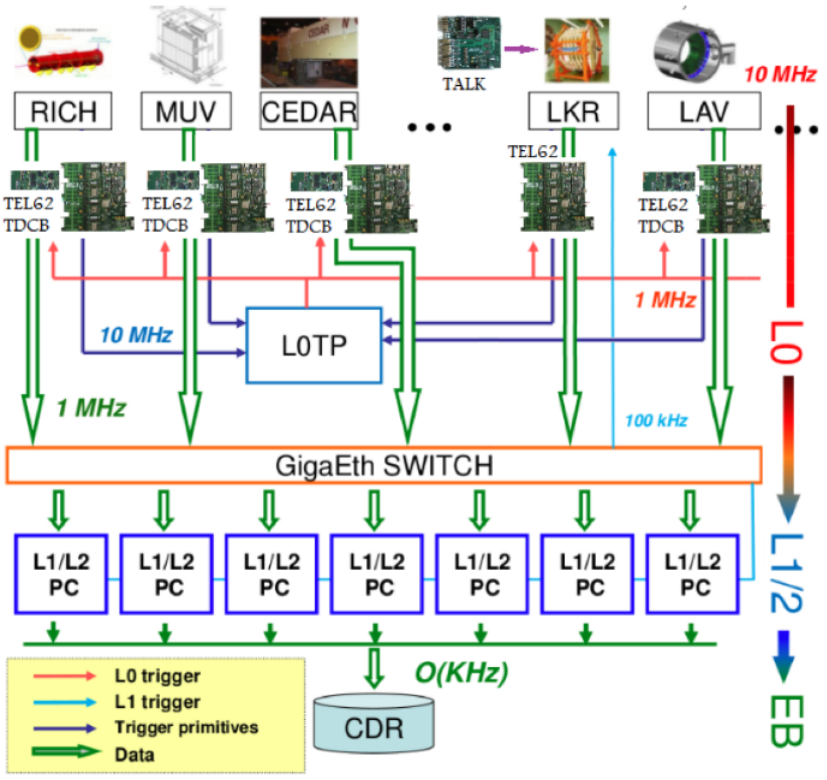

Figure 5.1: An overview of the NA62 trigger system and the corresponding data flow reduction [68].

For practical considerations, a common Timing, Trigger and Control (TTC) system[1] has been used for clock and trigger distribution. The TTC transmission system contains two multiplexed channels encoded using 40 MHz clock and transmitted at 160 MHz rate. All the synchronous elements of the TDAQ system (see the next section 5.1) run on the TTC clock and are synchronously reset by

[1]The system was developed at CERN and is adopted by all LHC experiments[60].

a *Start of Burst* (SOB) command and similarly stop on an *End of Burst* (EOB) signal delivered after a given number of 25 ns clock periods [60].

5.1 Readout

Most of the detector sub-systems at NA62 share a similar timing precision and readout capabilities, which led to a design of a common system based on high-precision Time-to-Digital converters (TDCs) (sec. 5.1.1). The spectrometers use their own dedicated systems made suitable for a high number of channels, where the GTK has the highest number of channels, which are coupled by optical fibres to meet the necessary time resolution (sec. 5.1.2). On the other side, in the case of the Straw spectrometer a lower time-resolution readout is sufficient (sec. 5.1.3). Calorimeters are read out by a flash analog-to-digital converter (FADC) system and have a separate readout (sec. 5.1.4).

5.1.1 Common readout

A TDC based system TEL62 provides a 100 ps time resolution and a possibility of an implementation of different trigger conditions. To provide the sufficient flexibility and programmability, the TEL62 board is able to host up to 4 mezzanine boards for input data channels controlled by field-programmable gate array (FPGA) with up to 2 GB of DDR2 RAM.

Each mezzanine TDC board houses 4 high-performance TDC (HPTDC) chips and can digitize times of leading and trailing edges for 128 detector channels. A 32-bit word is read out by HPTDC every 25 ns and 6.4 μs long frames are created. Frames from each TDC are merged and compacted together with additional data into the data blocks.

The TEL62 can also host an output quad-Gigabit Ethernet board driven by a fifth identical FPGA, which sends L0 trigger primitives to the L0TP and detector data blocks to the PC farm in the case that the L0 trigger is received.

Figure 5.2: A TEL62 board equipped with two TDC boards and the quad gigabit board [60].

5.1.2 GTK readout

The GTK off-detector readout (GTK-RO) comprise ten GTK-RO cards for each station (each card serving to one TDCpix). The GTK-RO card is controlled by an FPGA with 2GB of DDR2 RAM and is located directly at the PC-farm, connected to the corresponding TDCpix by 200 m long optical fibre. Each five GTK-RO cards (one row of TDCpix) share one PC making an interface between the card and the PC-farm [60].

5.1.3 Straw readout

The Straw Tracker readout chain can be structured into two parts. The first are front-end boards hosting two analogue readout CARIOCA chips[2], each reading and processing leading and trailing edges of 8 channels, and one FPGA containing 32 TDCs. The second part, containing the back-end electronics built on Straw Readout Boards (SRB), serves for communication with the TTC system and for sending the collected data to the PC-farm if they are selected by the trigger.

5.1.4 Calorimeter readout

The calorimeter readout system is based on Calorimeter Readout Modules (CREAM) and is used for LKr, MUV1, MUV2, IRC and SAC. One CREAM board is able to read up to 32 analogue channels via a daughter-board, which shapes the input signals and further digitizes them using an FADC. Data are further processed by an FPGA on the motherboard and copied to a DDR3 RAM waiting for the trigger condition to be sent.

5.2 L0 trigger

The L0 trigger is designed to reduce the data flow to the maximum rate of 1 MHz and latency below 1 ms which by default comprises only a small set of sub-detectors but can be easily extended to most of them. This set of detectors consists of: CHOD, NewCHOD, RICH, LAV12, MUV3 and calorimeters.

5.2.1 TDC-based L0

As discussed in section 5.1.1, these L0 trigger primitives are generated by TDCs on the corresponding TEL62 boards and the result of the trigger decision is based on the identification of hits belonging to the same event.

CHOD L0 provides selection of just single-track events with impact time correction, which is required due to the length of NA48 CHOD scintillator bars. These corrections become time demanding in a case of multiple hits[3]. It is used in L0

[2]The CARIOCA chips were originally developed for the LHCb muon chambers [60].

[3]The increasing inefficiency of the NA48 CHOD with higher intensity rates led to the construction of the NewCHOD detector.

as an independent stream (control trigger).

NewCHOD L0 is used for the appraisal of multi-track events as the tile construction does not require such corrections.

RICH L0 is based on the multiplicity of clusters of hits for any charged track above the Cherenkov signal threshold.

LAV12 L0 from the LAV system can be used in order to tag events with EM interacting particles within its geometrical acceptance.

MUV3 L0 can be used as both the positive trigger or a fast muon veto. All 296 MUV3 channels are connected to a single TEL62 board equipped with three TDC boards.

5.2.2 Calorimeter L0 (L0-Calo)

Due to a large data rate of calorimeters, their channels are first connected to the CREAMs, which save data into local temporary buffers, see section 5.1.4. The L0-Calo itself is based on TEL62 boards in three stages: Front-End, Merger, Concentrator, see figure 5.3.

Front-End boards ask a simplified information from CREAMs[4] and perform a search for energy peaks and compute related parameters. Merger boards merge peaks from the Front-End into single electromagnetic clusters[5]. And the final Concentrator board compute the total energies related to the event and generates trigger primitives, which are passed to the L0TP.

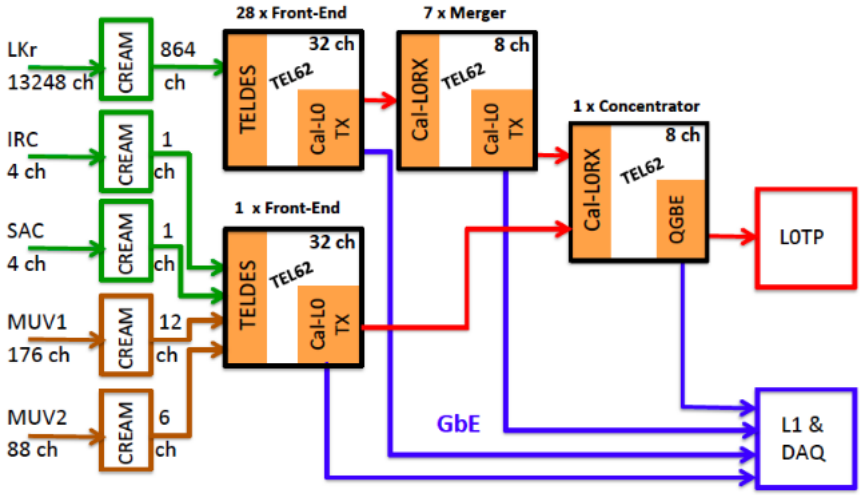

Figure 5.3: A scheme of the L0-Calo system [60].

[4]Front-End boards ask a total energy from each 4×4 cells and only 10 most significant bits of FADC (from the total 14).

[5]Contrary to the figure description, the L0-Calo is currently applied only for the LKr.

5.2.3 L0 Trigger Processor (L0TP)

The L0TP is made of a single FPGA which receives packets with multiple primitives, sorts them in time and checks if the combination within the time window meets the preset configuration, so-called *trigger masks*. If it does, L0TP sends a signal for the readout to send the data further to the PC-farm with the preset downscaling for given trigger masks. This operation is managed by the Associative Memory Module (AMM), which also generates so-called *trigger word*. Different types of *trigger word* will be summarized in section 5.4.

The synchronization of internal L0TP clock with the TTC is managed by a Phase Locked Loop (PLL), which automatically adjusts the phase of internal signal with the input one. There are two clock domains, the 40 MHz one is common with the TTC and 125 MHz clock is common with the trigger-algorithm logic and the ethernet communication.

Driving two uncorrelated streams corresponding to the same events, as is required for running both Physics and Control, is possible thanks to the Memory Management Unit (MMU), see figure 5.4. The time alignment of these two uncorrelated flows is critical as the output RAMs are read in parallel so the addresses of RAM are using the output of MMU, which is in principle the content of *merged_FIFO*[6] filled with sorted primitives of one 6.4 μs frame from the *reference_FIFO* and *control_FIFO*.

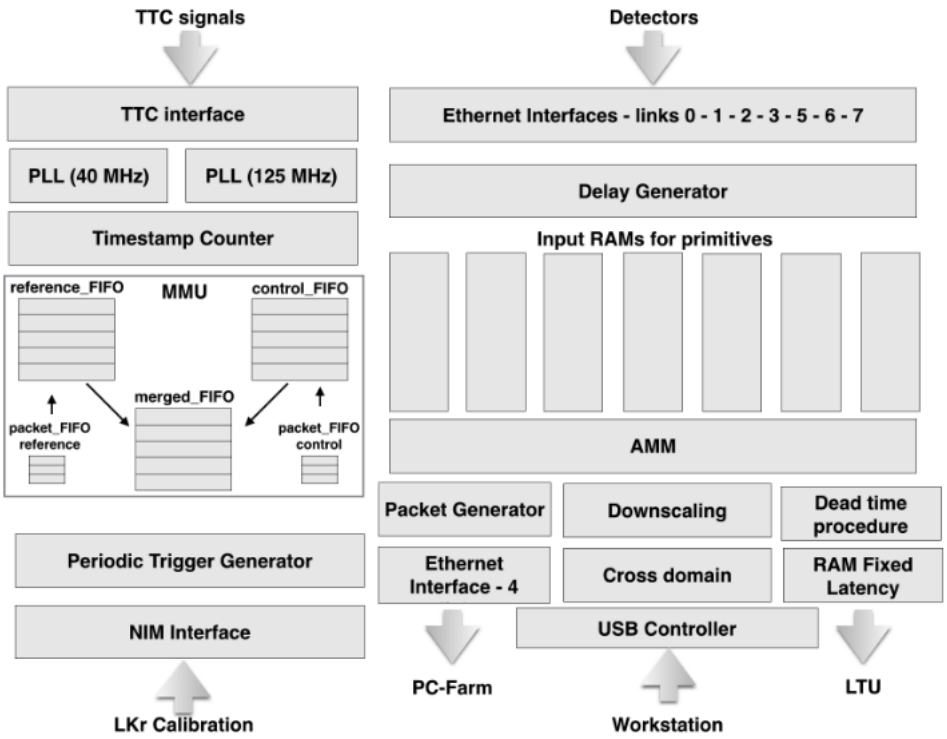

Figure 5.4: A scheme of the L0-Calo system [69].

[6]By FIFO we mean a memory buffer with the First-In-First-Out type of queue, where the first address entering the register also leaves as first.

5.3 High level triggers

While the maximum rate of the L0 trigger is 1 MHz a considerable data reduction has to be made to meet the requirements of the permanent data storage and hence a high level software trigger is used.

5.3.1 L1 trigger

The L1 trigger reduces the data rate by another factor 10. It uses KTAG and whole LAV system separately from L0 trigger. A partial downstream track reconstruction from Straws is also implemented, reducing the data flow even more.

5.4 Trigger types

The data type propagating through the TDAQ system is defined on the L0 level and is commonly classified by the *Trigger word* and can take the following definitions:

- The standard data-taking *Physics trigger* comprises the already mentioned hardware L0 and higher level software trigger.
- *Control trigger* is ran with a very general definition on the L0 level with an appropriate downscaling[7] and is usually used for the trigger efficiency studies.
- Beyond the standard data-taking triggers are used several special triggers gathering useful information for tests and monitoring purposes, e.g. the *Periodic trigger* or already mentioned SOB and EOB.

[7] In the case of $\pi\nu\bar{\nu}$ data-taking only CHOD is usually used as a Control trigger. The beam-dump case has specific trigger conditions, which will be specified in chapter 7.

6. Reconstruction procedure

The stored raw data are already distributed into *events* with some initial time offset[1]. The offline data reconstruction is made for each detector separately using the NA62Reconstruction routines of given revision of NA62FW [3]. It is based on matching signals in distinct channels into *hits* and matching hits into *candidates*. Unlike raw data, the reconstructed files have already the typical tree-like structure of ROOT files and are stored burst-by-burst.

6.1 Track reconstruction

By track reconstruction we mean the reconstruction of a Straw candidate, the reconstruction of whole charged track is done within the analysis and will be discussed in chapter 9, where standard (kaon) runs are analyzed. The Straw candidate reconstruction is based on an in-time matching of chamber hits (ideally full 4 hits for a high quality track) and an inter-chamber (first two and last chamber) matching in order to create the track vector.

The combination of vectors from before and after the magnet chambers with respect to the magnetic field gives rise to the full momentum vector before and after the magnet and a corresponding charge sign. The blue-field corrections already mentioned in section 4.6 are applied during the analysis.

6.2 LKr cluster reconstruction

The LKr cluster reconstruction algorithm scans all LKr cells for each event and makes a list of cells with $E_{cell} > 0.25$ GeV ordered from the highest to the lowest deposited energy. During this procedure the cells marked as *dead*[2] are skipped. Then, a loop over all these cells is performed checking the surrounding 8 cells[3] (3×3 box) to see whether the central cell really presents the most energetic one. If it does it is marked as a *seed* of the cluster [70].

After this procedure, there is a loop over all seeds and for each seed all the possible contributing cells based on the energy profile are taken into account to reconstruct the whole cluster. If the cell is shared among more clusters at the same time, the energy contribution to each cluster is weighted by the cluster profile as

$$E_i = E_{cell} \frac{W_i}{\sum_{clus} W_j}, \tag{6.1}$$

where W_i is the weight estimated for given types of cluster profile. If the cell is

[1]Time corrections (both pre-reconstruction and reconstruction) will be discussed further in section 6.3.3.

[2]Cell is considered dead if it manifestly provides a wrong signal (e.g. can be spotted as a *hot cell*). The list of dead cells is updated for each run and is attached to the reconstruction tool.

[3]If there is a dead cell among the surrounding cells, it checks also another line (5×5 box) of cells to inspect if the seed is not located in the dead cell.

marked in the database as dead, its energy contribution to the cluster is extrapolated from the cluster profile[4].

6.3 Corrections

During the reconstruction several correction and calibration procedures take place among which the most important corrections are the time corrections (T0) and momentum/energy corrections, which will be discussed in following sections. There are also some post-reconstruction corrections usually applied as *preanalyzers* before the data analysis itself.

6.3.1 Track corrections

Besides the mentioned blue-field corrections and T0 corrections discussed in the following section 6.3.3, which are applied already during the data reconstruction, so-called α and β corrections are applied using the SpectrometerTrackCorrections preanalyzer.

The SpectrometerTrackCorrections tool corrects the chamber x-y misalignment, which induces a split between opposite charged particles reconstructed masses, and track momentum p as

$$p_{corr} = p(1+\beta)(1+\alpha p \cdot q), \tag{6.2}$$

where q is the track charge and α, β constants are evaluated from reconstructed $K_{3\pi}$ decays for each run and are provided by the NA62ConditionsService. The α here corresponds to the geometrical misalignment of chambers and takes the value $\sim 10^{-9}$ MeV$^{-1}/c$ and β corresponding to miscalibration of the magnetic field is typically $\sim 10^{-3}$ [71].

6.3.2 LKr cluster corrections

The LKr corrections incorporate the position alignment and the energy corrections required for the overall energy as well as a cluster non-linearity or the energy loss in the beamline hole. All are treated by the LKrClusterCorrections preanalyzer.

The position alignment has a fixed value for the Monte Carlo (MC) data and for real data is determined offline for each run. The values are provided by the NA62ConditionsService. The x-y cluster position is corrected for the motion of the center of the shower developing in the LKr and can be simulated by the MC. Also extra x position correction is applied to compensate the cell zig-zag structure [70].

Similarly for the energy corrections, which vary run-by-run or burst-by-burst and are either provided by the NA62ConditionsService, which loads them from

[4]There is obviously a possibility of a systematic error entering the data analysis in this procedure and hence more strict cuts on the cluster distances and distances from dead cells will be applied in the data analysis.

the database[5], or are fixed for MC. The loss-in-the-hole corrections have fixed values evaluated using MC for given radius and vary with energy but by choosing an additional acceptance cut during the analysis one can avoid bad cluster reconstruction completely. The non-linearity corrections cover the bias induced by the feedback in electronics, while the overall correction covers a different behaviour of low energy and high energy clusters with respect to their position [70].

6.3.3 Time corrections

There are several steps in which are time corrections (so-called T0s) calculated and applied [72].

- *Initial T0s* are setup already before data-taking by hand and are applied online as they are essential for an alignment of trigger primitives within one event and hence also for the trigger decision.
- *Coarse T0s* are applied offline as the first step during reconstruction. They are calculated on 100 bursts and they give us time offsets for sets of channels.
- *Magic T0s* are applied offline and are evaluated for Straw channels wire-by-wire, where the hit time distribution is compared to the hypothesis one by a Gaussian fit [3].
- *Fine T0s* are applied during the offline reconstruction. They represent channel-by-channel time corrections with respect to the referential time (usually taken as the KTAG time).

[5]These values for cluster corrections are evaluated from a known densly populated mode. Up to NA62FW v1.0.4 a value EoP (see section 8.1) from K_{e3} decay was used. From v1.0.5 π^0 reconstruction from $K_{2\pi}$ decay is used (see chapter 9) [72].

7. NA62 in the beam-dump mode

Despite the fact that the target at NA62 experiment is quite far from the decay region (as is needed for kaon decays), it was realized that even without significant intervention there is a possibility of running the experiment in the beam-dump mode and reach energy and sensitivity regions necessary for exotic searches yet unreached by other experiments. It was verified by MC simulations that the big distance between target and decay region is partly compensated by the primary beam energy thanks to the Lorentz boost of the secondary products. The Lorentz boost also shifts their angle distribution into the acceptance of downstream detectors, giving an opportunity to study the following:

- heavy neutral leptons;
- dark photons (heavy vectors);
- scalar (Higgs-like) particles;
- pseudo-scalar (axion-like) particles

in a new way beside the *parasitic mode*[1].

The general conditions in the beam-dump mode, incorporating changes with respect to the conditions described in previous three chapters, will be summarized in the following section 7.1. A more specific study for ALPs is outlined in the section 7.2.

7.1 General data taking conditions and status

When running the NA62 experiment in the beam-dump mode, several special data-taking conditions have to be incorporated:

- the beam momentum selecting TAX apertures are closed;
- the beryllium target T10 is removed and hence the proton beam is impinged directly onto 1.6 m thick copper TAXes;
- only the downstream part of the experiment is used as the measurement of the original beam properties (or the beam itself) are ill-defined in this case;
- a different trigger setup of the trigger masks is used.

The trigger for the beam-dump mode incorporates only two detectors as a positive trigger (no veto is used): the NewCHOD as a physics and the LKr as a control trigger. More specifically, any of the trigger primitives defined in the following table (7.1) has to be received by the L0TP so it sends a signal for the transition of the data to the PC-farm.

[1]By parasitic mode is meant a possible production of hidden sector particles from interactions of remaining protons in the secondary beam with the material of TAX in the kaon data-taking mode.

detector	trigger word(bit)	definition	downscaling
NewCHOD	physics (bit 14)	Q1 (hit in one quadrant)	5
NewCHOD	physics (bit 10)	Q2 (hit in two quadrants)	1
LKr	control (bit 10)	$E_{LKr} \geqq 2$ GeV $\wedge$ $N_{clus} \geqq 2$	1

Table 7.1: Overview of the trigger primitives.

There were several occasions during the data-taking in years 2016-2018 when it was not possible to run the experiment in the 'standard' data-taking mode but it was possible to fulfill other conditions necessary for exotic searches. An overview of runs taken in the beam-dump mode together with the occasion and other information is summarized in the following table 7.2.

Run number	N_{POT} (10^{15})	revision	occasion	T0 run
6814 (2016)	2.4	r1982	LHC Pb	6793
6912 (2016)	0.6	v1.04	LHC Pb	6903
7858 (2017)	2.4	r1982	GTK off	7847
7859 (2017)	1.1	r1982	GTK off	7847
7980 (2017)	0.2	v1.04	MNP33 unstable	7978
7981 (2017)	1.3	v1.04	MNP33 unstable	7978
8179 (2017)	0.1	v1.04	GTK off	8177
8278 (2017)	0.3	v1.04	in/close	8274
8279 (2017)	0.3	v1.04	out/close	8274
8280 (2017)	0.11	v1.04	out/open	8274
8477 (2018)	2.7	v1.04	HASC off	8470
8478 (2018)	1.15	v1.04	HASC off	8470
8762 (2018)	1.2	v1.04	GTK off	8778
8763 (2018)	1.8	v1.04	GTK off	8778
8764 (2018)	2.4	v1.04	GTK off	8778
8765 (2018)	0.8	v1.04	GTK off	8778
8768 (2018)	0.1	v1.04	GTK chip 8	8778
8769 (2018)	2.3	v1.04	GTK chip 8	8778
8770 (2018)	2.3	v1.04	GTK chip 8	8778
8771 (2018)	2.0	v1.04	GTK chip 8	8778
8773 (2018)	0.7	v1.04	GTK chip 8	8778
8774 (2018)	2.7	v1.04	GTK chip 8	8778

Table 7.2: A summary of runs taken in the beam-dump mode in a 2016-2018 period. Runs taken during 2016 had a trigger set only for charged particles [73].

By summarizing the number of protons-on-target N_{POT} for the whole period, we have a total of $2.6 \cdot 10^{16}$ POT collected from the control trigger and $2.9 \cdot 10^{16}$ POT from charged triggers.

7.2 Production and detection of ALPs at NA62

The search for ALPs in the NA62 beam-dump mode is dedicated to the decay to two photons, which means a restriction to the neutral channel depicted in the previous section[2].

Estimated production of ALPs via the Primakoff effect by 400 GeV/c proton beam on a copper target, as is the case of NA62, has been evaluated in [55] for $g_{a\gamma\gamma} = 10^{-4}$ GeV^{-1}, see figure 7.1.

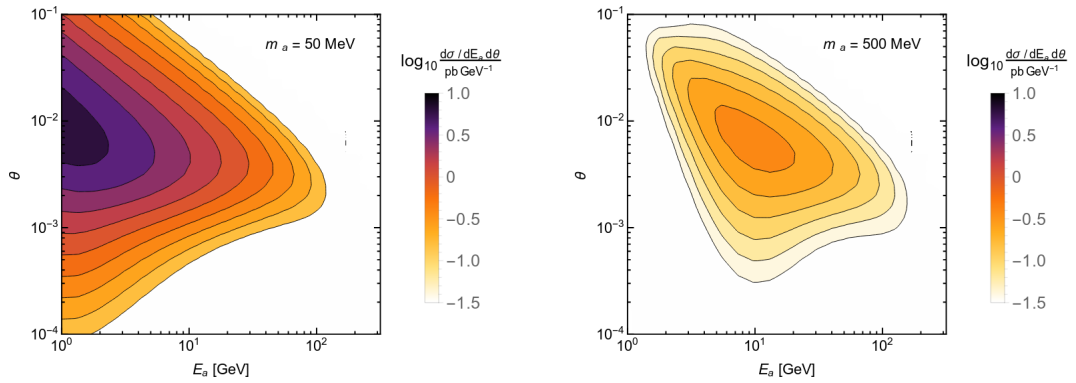

Figure 7.1: Predicted ALP production angle distribution of differential cross-section for Cu target and 400 GeV/c proton beam for cases $m_a = 50$ MeV/c^2 and $m_a = 500$ MeV/c^2 [55].

A simple guess of the probability that the produced ALP will decay within the detector acceptance will be given by the probability of a decay in the decay region distant D from the target. Also the angle between photons θ has to be within the acceptance of the LKr $\theta_{max} \approx R/(D+L)$, where R is the LKr radius and L is the length of the decay region (or in terms of Lorentz factor $\gamma > L/R$). On the other side the opening angle between photons must allow separation of their clusters (or in terms of distance between clusters d_{min} and Lorentz factor $\gamma < 2L/d_{min}$). The overall probability guess for an ALP with decay length l_a, derived in (3.6), is then

$$p(l_a, \gamma, \theta) = \begin{cases} \exp(-D/l_a), & \text{if } \gamma < L/R,\ \gamma < 2L/d_{min} \text{ and } \theta < \theta_{max} \\ 0, & \text{otherwise} \end{cases} \tag{7.1}$$

and the fiducial cross-section is then given by the product of the detection probability and the production cross-section as

$$\frac{d\sigma_f}{dE_a d\theta} = p(l_a, \gamma, \theta) \cdot \frac{d\sigma}{dE_a d\theta}. \tag{7.2}$$

A more sophisticated approach would be an MC simulation[3], where a preliminary simulation has been performed in [55]. For the resulting fiducial cross-section

[2]Other decay modes (leptons) are restricted from the parasitic mode, where in spite of a tremendous statistics, the S/B is too small for the neutral channel.

[3]Actually, it is a necessary approach in order to evaluate the single event sensitivity (SES), which will be further discussed in chapter 10. The overall experiment geometry can be then taken into account within the NA62FW.

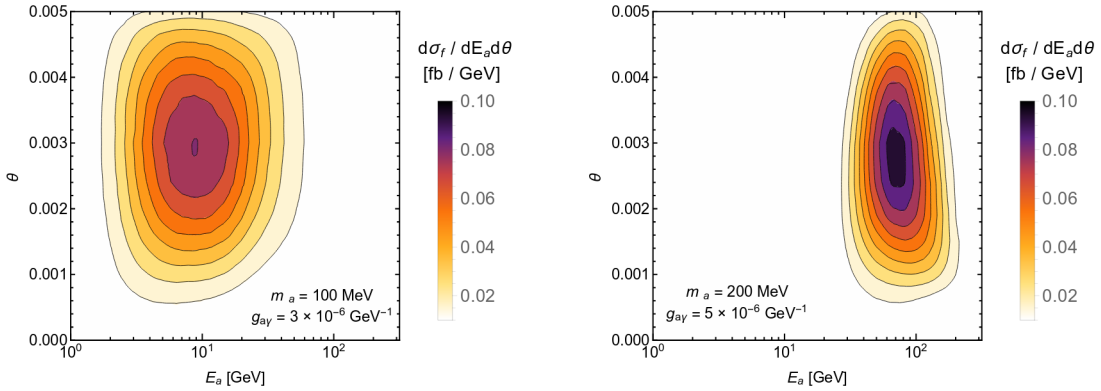

Figure 7.2: Predicted fiducial cross-section for deposited energy and opening angle for fixed values of axion mass and coupling [55].

see figure 7.2, which shows the first estimates of the signal regions for given axion masses and photon couplings.

These estimates are considering a faultless detection, i.e. 100% efficiency of the trigger and the readout logic but a real response of the hardware has to be checked. Luckily the beam-dump data are rich on charged events and hence one can cross-check the response of different systems as these events are both physics-triggered and control-triggered. The corresponding analysis will be performed in the following chapter 8.

To check the data-quality of neutral events in the beam-dump mode would be more challenging as the statistics is much lower. Nevertheless, as one expects a similar data quality of the beam-dump run with the preceding (or succeeding) standard run (T0 run marked in the table 7.1), the detector response can be checked for known decays with two photons in the final state in these runs. Luckily, kaon runs are rich on the production of π^0, which will be studied in the chapter 9.

8. Trigger efficiency study

According to MC simulations, muons are the most common background in the beam-dump mode [74]. They, however, trigger Q1 and also depose only little energy in the LKr[1] and hence cannot be directly used for the study of the Control trigger, which is defined by two 'non-MIP' LKr clusters (see table 7.1 with trigger definitions in BD). Nevertheless, these muons can easily produce in the material of the detector e^+e^- pairs, which trigger both Physics(Q2) and Control trigger.

In this chapter the e^+e^- pairs will be selected primarily for the study of the trigger efficiency. However, it proves useful also for the determination of interactions of the muon halo with the detector material as for charged events the source can be tracked and a coincidence between data and MC can be tested. Such procedure is much more challenging for neutral events.

The analysis is performed on runs 8762-8774 (v1.0.4) as they represent a high statistics with stable data-taking conditions. Both LKrClusterCorrections and SpectrometerTrackCorrections preanalyzers are used.

8.1 Event selection

The e^+e^- selection conditions and performed cuts will be listed further together with the corresponding plots. It is required that:

- at least two charged tracks downstream are present;

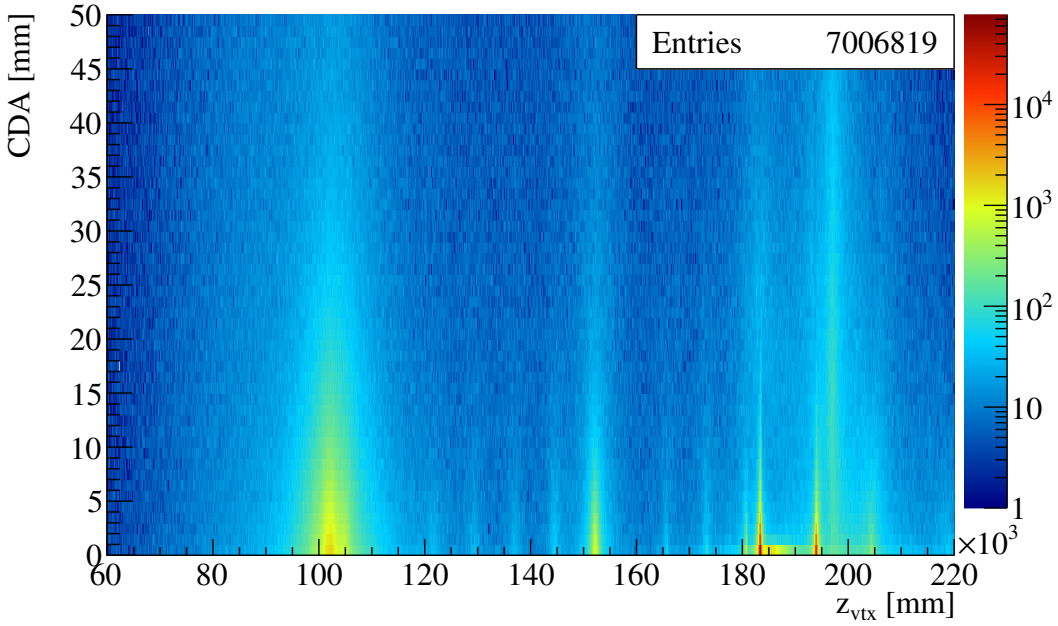

Figure 8.1: Z position of vertex and corresponding CDA of matched tracks.

- exactly two charged tracks have a common vertex (CDA < 15 mm);

[1]Muon presents so-called minimum ionizing particle (MIP).

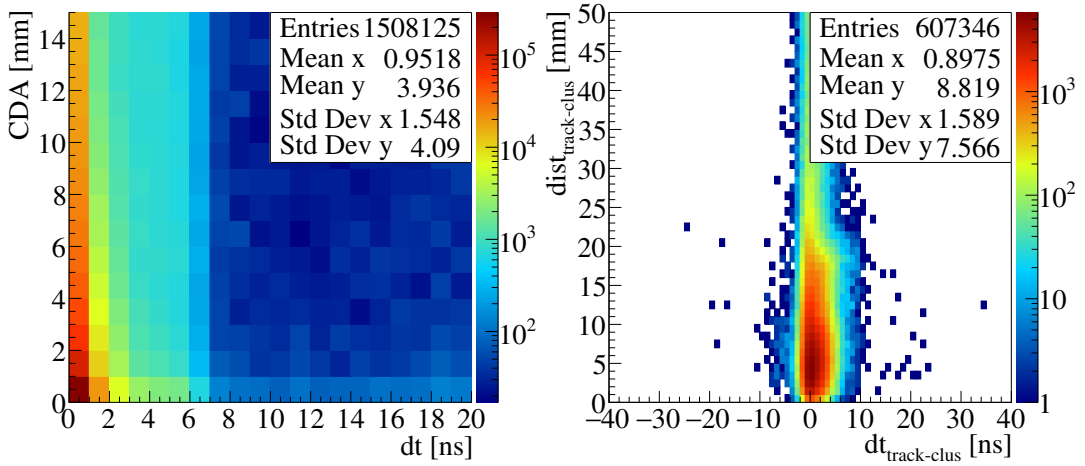

Figure 8.2: Left: Time difference and corresponding CDA of matched tracks; Right: Distance of the track projection from the associated cluster with respect to the time difference.

- charged tracks with a common vertex are in time within 3 ns and have opposite charges;
- LKr clusters have to be geometrically associated to these tracks (a maximum distance 50 mm from the track projection);
- associated LKr clusters must have at least 1 GeV;

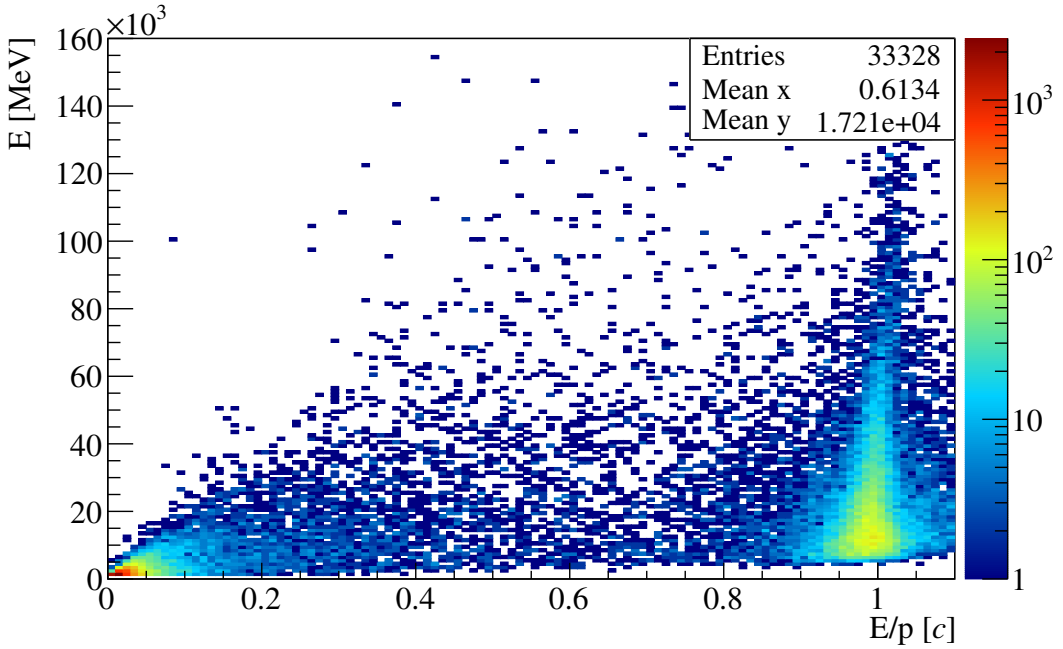

Figure 8.3: EoP for selected tracks with respect to the deposited energy.

- E/p (EoP) of the tracks is above 0.85[2].

[2]EoP presents the most efficient selection criterion for the identification of a high-energetic electron as it is the lightest charged particle and unlike μ and π it leaves all its energy in LKr.

8.1.1 Vertex position

By comparison of figures 8.1 and 4.2 one can distinguish the detector components, where the products of muon halo interactions could origin. The dominant source is typically the region between the final collimator and CHANTI. Next, one can see individual LAV stations with the dominant LAV5, the spectrometer magnet and sharp peaks at spectrometer chambers[3]. A cut through the x-y plane of vertex position for the collimator/CHANTI region and for LAV5 is projected in following figures.

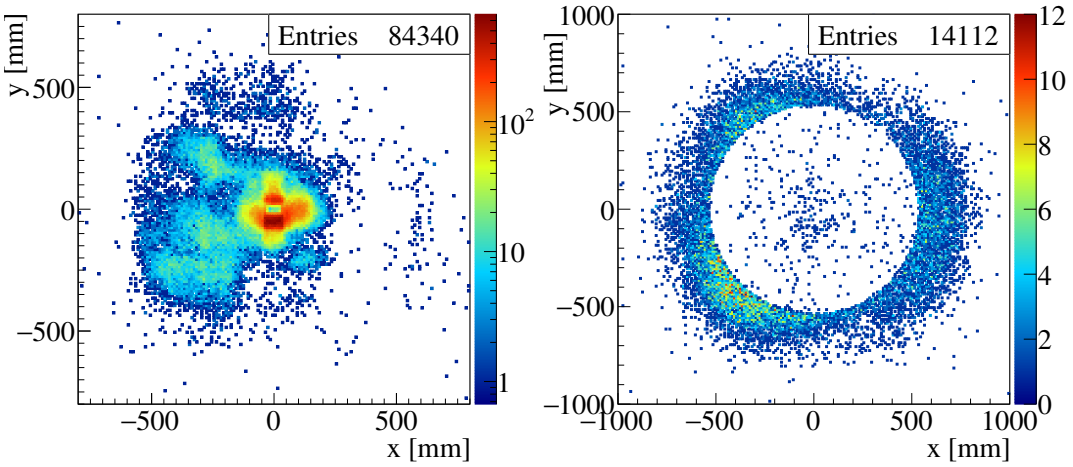

Figure 8.4: Vertex x-y position in CHANTI (left) and LAV station 5 (right).

8.2 Trigger efficiency

The trigger efficiency ε is defined for the e^+e^- selected sample (as described in the previous section) as follows

$$\varepsilon = \frac{\text{Physics(Q2)} \wedge \text{Control}}{\text{Physics(Q2)}}. \tag{8.1}$$

By asking for the corresponding trigger word and mask from the L0TPData, the resulting efficiency with respect to the total energy is poor (see figure 8.5). Nevertheless, if trigger primitives of L0Calo and L0NewCHOD are asked for instead[4], the resulting efficiency distribution seems correct (see figure 8.6).

Different results for the primitives and the trigger could be indicating a misbehaviour of L0TP during the trigger decision. This phenomenon has been recently independently validated by comparison of the primitives stored within triggered

[3]Tracks originating in the spectrometer could be fake tracks (fake signal) [75], but are usually automatically vetoed during analysis (e.g. $K_{2\pi}$ in next chapter) by choosing the allowed decay region.

[4]A configuration, where L0NewCHOD Q2 is allowed in the 25 ns ($\pm$12.5 ns) wide trigger slot only and L0Calo is allowed also in adjacent time slots (together $\pm$37.5 ns), is chosen.

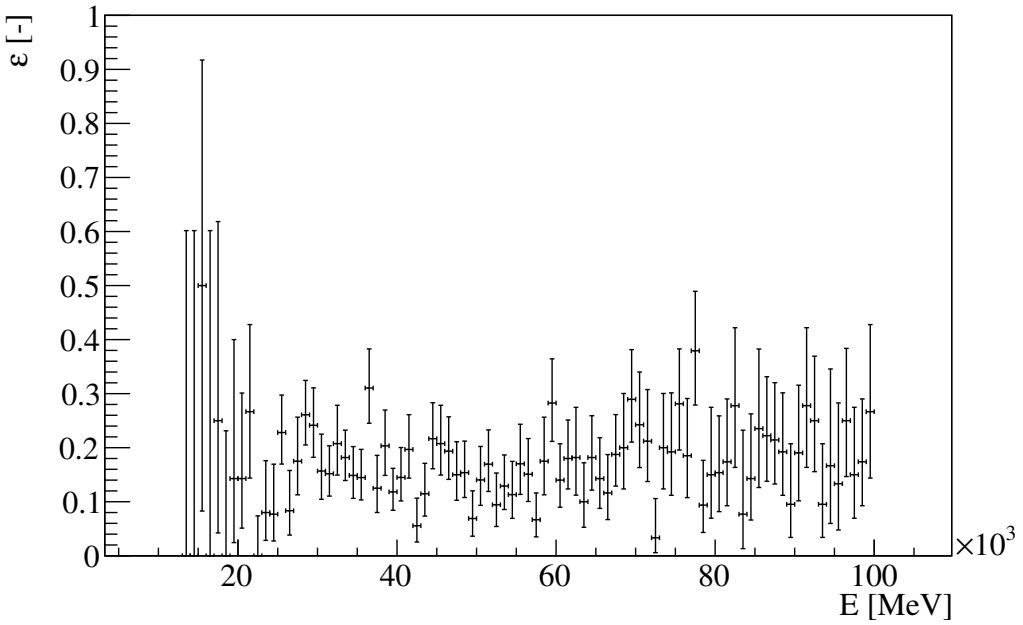

Figure 8.5: e^+e^- trigger efficiency when asking for trigger masks.

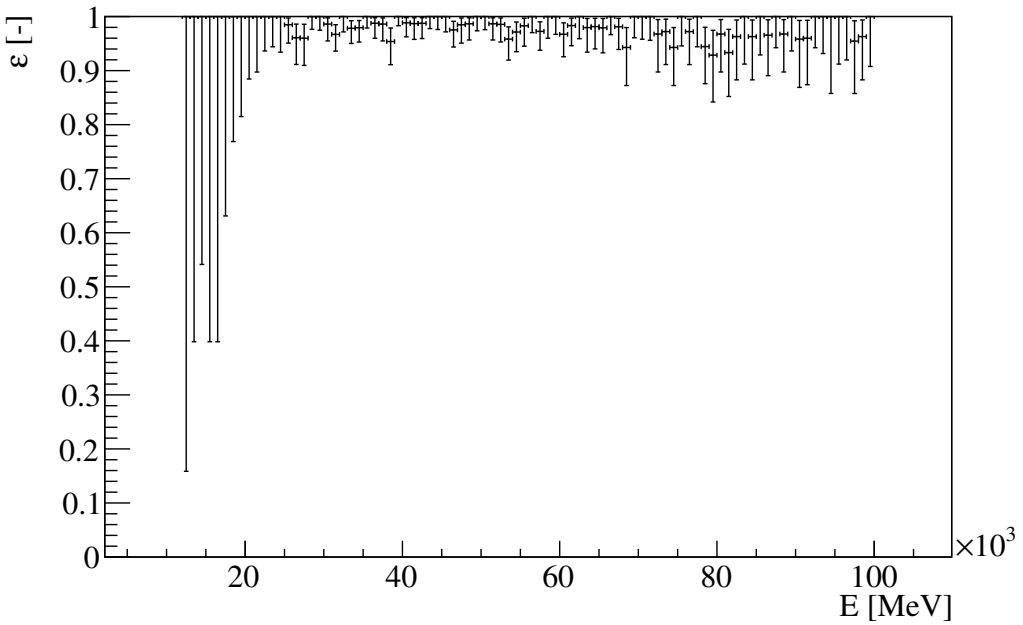

Figure 8.6: e^+e^- trigger efficiency when asking for trigger primitives.

data and the primitives stored separately in so-called *primitive dump*[5]. Appreciable losses of data, which should have been triggered, were observed [76].

[5]The primitive dump serves as a storage of all L0 primitives, which are saved irrespective to the trigger decision for each tenth burst for control reasons.

8.2.1 L0TP misbehaviour

The described phenomenon has been found as a consequence of a defect in the L0TP firmware, which escaped observation in kaon runs due to higher primitive rates but were fully revealed in the beam-dump mode. The defect itself was localized in the merging process of *reference_FIFO* and *control_FIFO* of MMU described in the section 5.2.3. The defect description can be summarized as: the first FIFO reaching the end of the frame does not send the last primitive to the *merged_FIFO* [77]. This behaviour results in a loss of the corresponding trigger and hence if there is no other condition triggering the event, it will not be stored. In the case that the event is triggered with more primitives independently (case of charged events), the written trigger mask has wrong values but the primitives themselves are untouched, which explains the difference between figures 8.5 and 8.6.

While the code of the L0TP has been corrected for future runs (starting in 2021), the amount of data gathered during 2016-2018 has been inevitably affected. Due to the high rate of primitives in the standard data-taking the overall number of lost events is almost undetectable. However, in the beam-dump mode are $N \sim 10^3$ Control trigger primitives and $N \sim 10^6$ Physics trigger primitives per $t_{burst} = 4.6$ s long burst. This means that if one looks for the Control triggered ones, there is effectively at maximum one LKr primitive in the $t_{frame} = 6.4$ μs long frame, while for the NewCHOD one gets for each frame an average $\mu = N \cdot t_{frame}/t_{burst} \approx 1.4$ prim/frame. Thus, the probability given by the exponential distribution $f(t, \mu) = \mu e^{-\mu t}$ that the Physics primitive is earlier in a frame than the Control one (and hence the Control mask is correct and the corresponding event is stored) will be

$$P(\mu \approx 1.8) = \int_0^1 dT(1 - \int_T^\infty dt \mu e^{-\mu t}) = \int_0^1 dT e^{-\mu T} = \frac{1 - e^{-\mu}}{\mu} \approx 50\%. \quad (8.2)$$

8.3 Intensity dependence

The hypothesis uttered in the previous section also implies that with a higher beam intensity (and thus higher rate of NewCHOD primitives) the losses of data in BD mode should be higher as well. Hence, the gathered beam-dump runs (summarized in table 7.2) will be revised in the following by comparison of beam-dump data and the primitive dump together with an evaluation of the impact of the L0TP defect and the possible intensity dependence. The intensity is expressed as usual in the number of protons on target (PoT), while by the efficiency in this section will be meant the portion of purely neutral events passing the L0TP defect[6].

Run 8769, which was not very stable in terms of intensity has, however, proven the hypothesis of the scaling of the efficiency with the intensity (see figure 8.7) as well as it proves a relative stability of the efficiency.

[6]Charged events are usually stored even if the trigger mask is wrong as they produce both Control and Physics primitives.

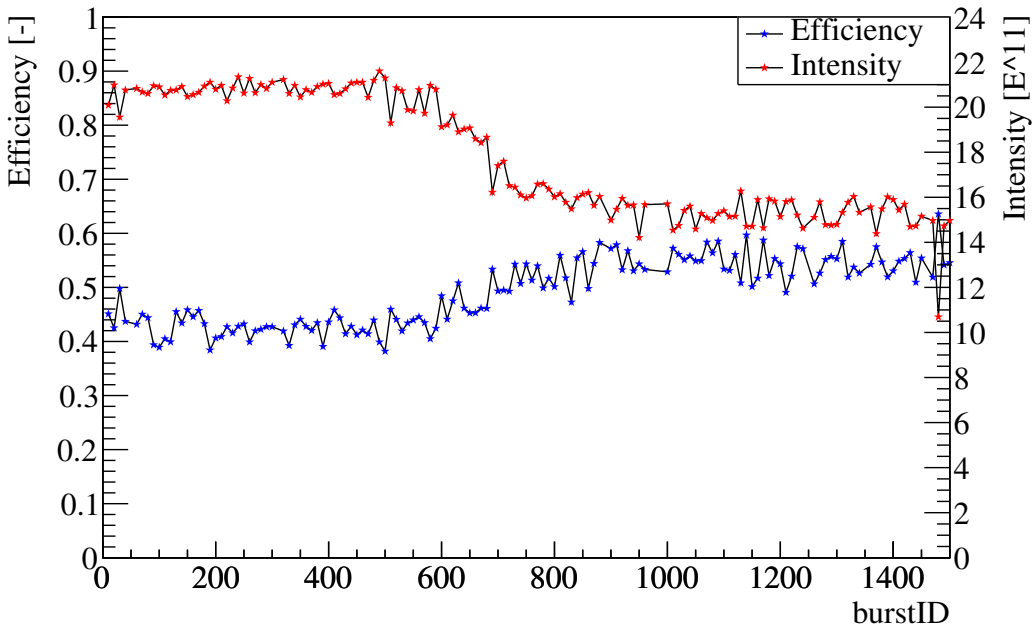

Figure 8.7: Beam intensity and efficiency for neutral events during the run 8769.

Since runs 8762-8774 were taken during the same period under the same data-taking conditions the scaling of efficiency with respect to the intensity follows continuously the same trend, see figure 8.8.

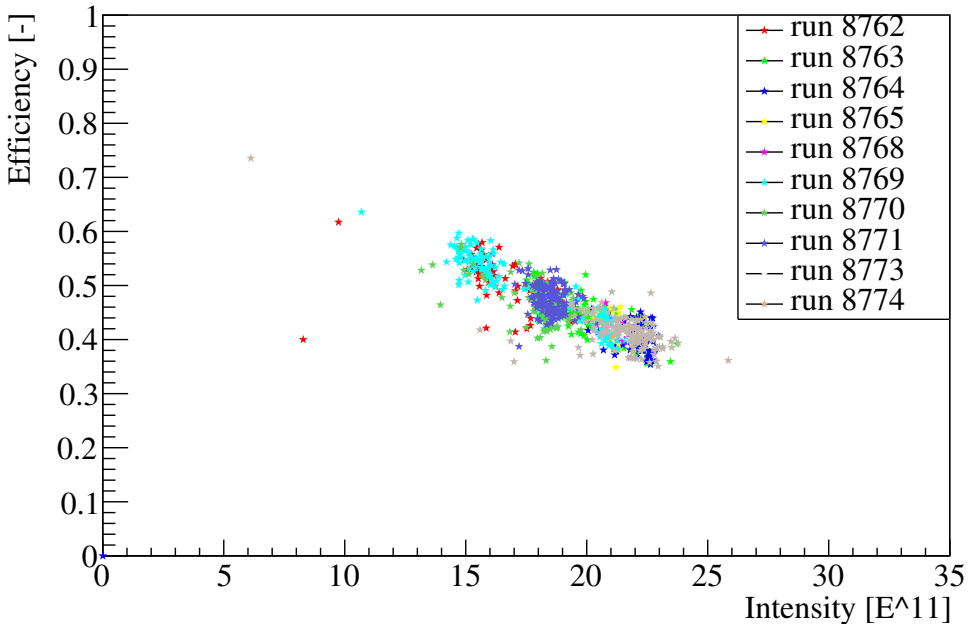

Figure 8.8: The intensity dependence of the efficiency for runs 8762-8774.

Finding of such stability of the efficiency for runs 8762-8774 presents a favourable result as these runs represent a majority of the statistics. In comparison, the 2017 data do not follow the same trend, but one has to take into consideration that they were taken during various data-taking periods. In summary, they evince lower efficiency for the same intensities but they still present a stable

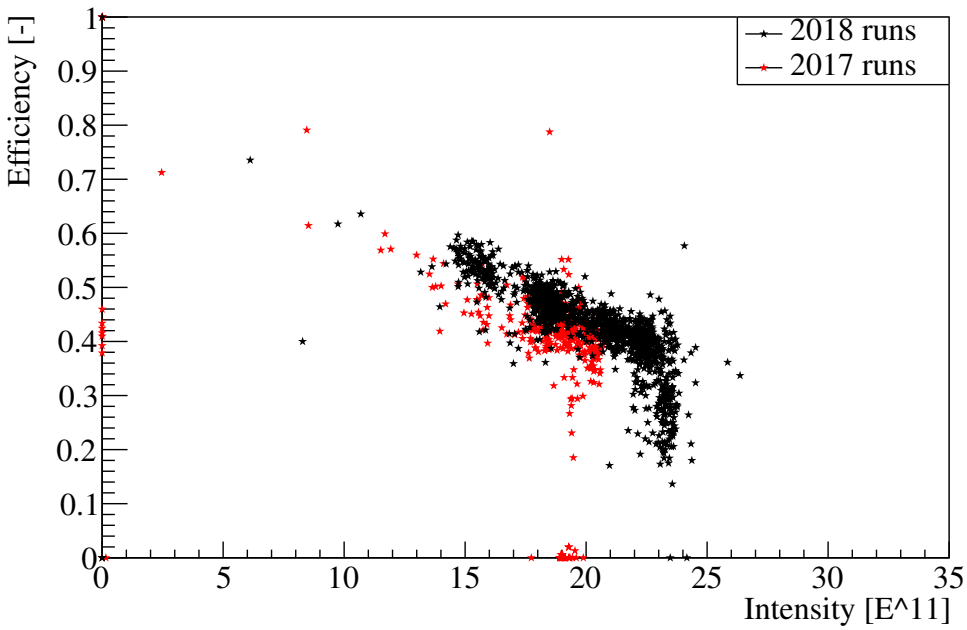

Figure 8.9: The intensity dependence of the efficiency for all 2017 and 2018 runs.

sample (see figure 8.9) with values roughly corresponding to the predicted 50% by the equation (8.2).

The 'tail' in 2018 sample in figure 8.9 is due to the remaining 2018 runs 8477 and 8478. The situation for these runs, which also represent a significant statistics, seems to be quite different and while the intensity was very stable the efficiency was not (see figure 8.10).

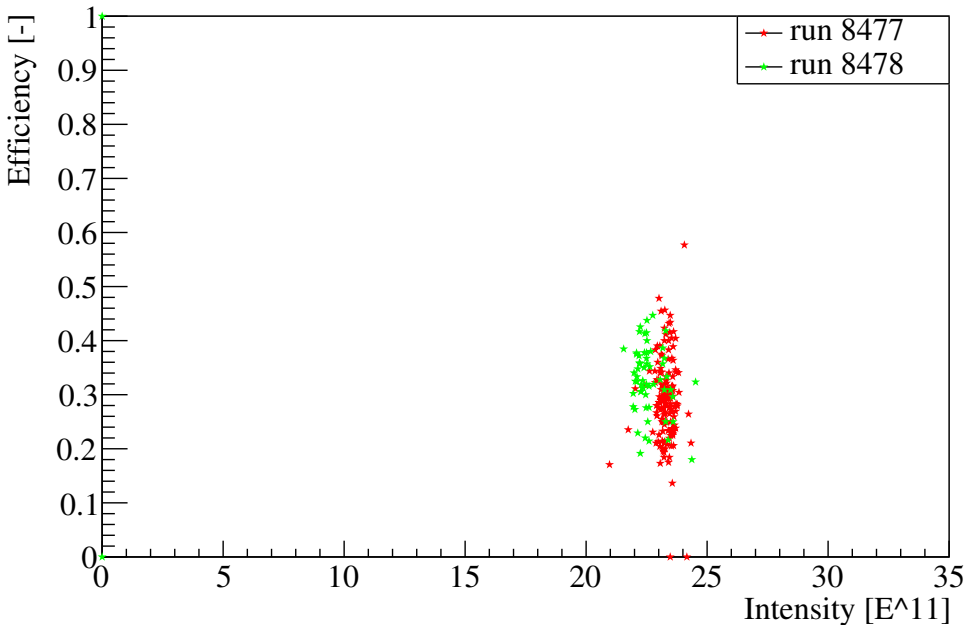

Figure 8.10: The intensity dependence of the efficiency for runs 8477 and 8478.

Similar tail is present in 2017 data and corresponds to the run 8280 with very low statistics. Almost zero efficiency evinces the run 8278.

This indicates that other factors could internally influence the stability of data-taking via the L0TP defect. It can be anticipated that similar factors could influence the data quality of kaon runs from the same data-taking period, which will be confirmed in the following chapter in the context of 'T0 runs'.

8.4 Results of primitive dump study

By summarizing the efficiency for all beam-dump runs as studied in the previous section (see the following table 8.1), one gets the overall number $\approx 43.3\%$. Thus, from the number of $2.6 \cdot 10^{16}$ PoT for neutral runs $\approx 1.13 \cdot 10^{16}$ PoT were effectively measured.

The efficiency error in the table 8.1 was evaluated with respect to the corresponding statistics as a binomial error

$$\sigma_\varepsilon = \frac{\sqrt{\varepsilon(1-\varepsilon)N_{passed}}}{N_{passed}}, \tag{8.3}$$

where N_{passed} is the number of events, which passed the defect.

Run number	N_{POT} (10^{15})	**efficiency (%)**	**occasion**	**T0 run**
7858 (2017)	2.4	$(42.6 \pm 0.3)\%$	GTK off	7847
7859 (2017)	1.1	$(38.4 \pm 0.5)\%$	GTK off	7847
7980 (2017)	0.2	$(42 \pm 1)\%$	MNP33 unstable	7978
7981 (2017)	1.3	$(44.7 \pm 0.4)\%$	MNP33 unstable	7978
8179 (2017)	0.1	$(45 \pm 3)\%$	GTK off	8177
8278 (2017)	0.3	$(0.3 \pm 1.9)\%$	in/close	8274
8279 (2017)	0.3	$(40 \pm 4)\%$	out/close	8274
8280 (2017)	0.11	$(29.2 \pm 0.5)\%$	out/open	8274
8477 (2018)	2.7	$(30 \pm 1)\%$	HASC off	8470
8478 (2018)	1.15	$(33 \pm 2)\%$	HASC off	8470
8762 (2018)	1.2	$(49.3 \pm 0.4)\%$	GTK off	8778
8763 (2018)	1.8	$(43.3 \pm 0.3)\%$	GTK off	8778
8764 (2018)	2.4	$(40.4 \pm 0.3)\%$	GTK off	8778
8765 (2018)	0.8	$(42.3 \pm 0.5)\%$	GTK off	8778
8768 (2018)	0.1	$(42 \pm 1)\%$	GTK chip 8	8778
8769 (2018)	2.3	$(48.3 \pm 0.2)\%$	GTK chip 8	8778
⋮	⋮	⋮	⋮	⋮

Run number	N_{POT} (10^{15})	**efficiency (%)**	**occasion**	**T0 run**
⋮	⋮	⋮	⋮	⋮
8770 (2018)	2.3	$(46.6 \pm 0.3)\%$	GTK chip 8	8778
8771 (2018)	2.0	$(47.5 \pm 0.3)\%$	GTK chip 8	8778
8773 (2018)	0.7	$(39.3 \pm 0.5)\%$	GTK chip 8	8778
8774 (2018)	2.7	$(41.3 \pm 0.3)\%$	GTK chip 8	8778

Table 8.1: An updated table 7.2 for neutral runs with assessed efficiency.

By run-by-run comparison the small contribution of runs 8278 and 8280 to the final efficiency can be seen, but also these runs should be investigated more in the future.

9. T0 runs data quality

As $BR(K^+ \to \pi^+\pi^0) = (20.67 \pm 0.08)\%$ and $BR(\pi^0 \to 2\gamma) = (98.823 \pm 0.034)\%$ [14], kaon runs close (in time) to the beam-dump ones, are a good opportunity to cross-check the detector behaviour for events with 2γ in final state. As most of the statistics, as well as the whole statistics from 2018, is covered by means of T0 and correction parameters by runs 8470 (129 bursts) and 8778 (913 bursts), currently reconstructed with version v1.0.5 - see table 7.1, a simple $K_{2\pi}$ analysis will be performed for these two runs.

For this study the Control trigger, which is defined for these runs as a signal in CHOD downscaled by 400, will be selected. The LKrClusterCorrections and the SpectrometerTrackCorrections will not be applied as the necessary coefficients were not provided yet for these newly reconstructed runs.

9.1 Event selection (run 8778)

Unlike in the case of previous chapter, strictly one charged track downstream will be required here, by which following decay modes are predominantly selected: $\mu^+\nu_\nu$, $\pi^+\pi^0$, $\pi^0e^+\nu_e$ (K^+_{e3}), $\pi^0\mu^+\nu_\mu$ ($K^+_{\mu3}$) and $\pi^+\pi^0\pi^0$ [14]. In order to distinguish π^+ from leptons a more sophisticated particle identification (PID) method (than e.g. EoP ratio used before for electrons) will be required.

9.1.1 Particle identification

From the track direction projection onto RICH PMTs, one is able to measure the radius of a circle cast by Cherenkov light and by comparison with the momentum determine the likelihood that the track belongs to π^+ (see figure 9.1).

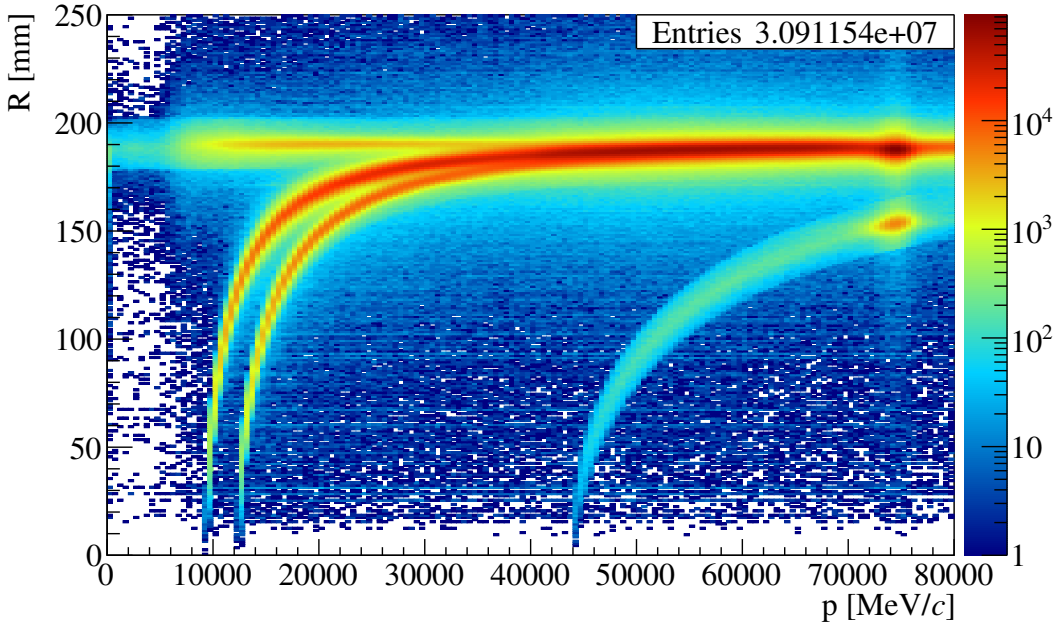

Figure 9.1: RICH ring radius of the track with respect to its momentum.

As already discussed in section 4.8 and as is apparent from the figure above, it is possible to distinguish μ^+ and π^+ at RICH only for momenta from 15 GeV/c to 35 GeV/c. Thus, RICH will be used only for a selection in this region and other steps for PID in the whole momentum spectrum will take place. Thanks to a very good time resolution of RICH, its time will be used as a referential one for the downstream track in the rest of the analysis.

To cut off the μ component, track will be projected further onto MUV3 and matched with the signal from the geometrically closest tile (see figure 9.2). A cut is performed on matched tiles with the signal time within 5 ns from the track referential one.

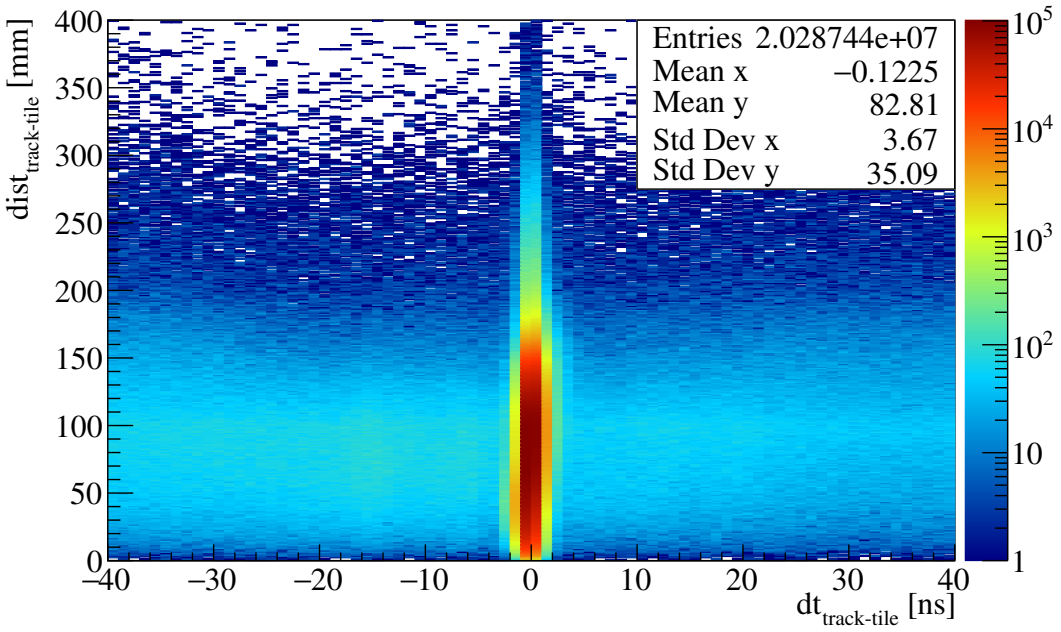

Figure 9.2: Time difference between the track and the associated MUV3 tile with respect to the distance of the track projection from the tile.

In order to clean the remaining sample, a PID using calorimeters can be performed as each particle type leaves a specific shape of the shower and can vary in a number of parameters. For this purpose will be used the SpectrometerCalorimetersAssociation tool of NA62FW [3], which employs Boosted Decision Trees (BDT) as an MVA technique provided by the TMVA of ROOT [4].

Parameters from associated LKr, MUV1 and MUV2 clusters as the total energy, number of cells, energy of the seed and energy deposited in each of the calorimeters are used to determine probabilities that the particle is e, μ or π. Specifically, for our case $P(\pi) > 90\%$ (see figure 9.3) is required, which suppresses the μ component to the order of 10^{-4} and the electron component to about $5 \cdot 10^{-3}$, but even bigger suppresion is reached thanks to the MUV3 veto condition [78].

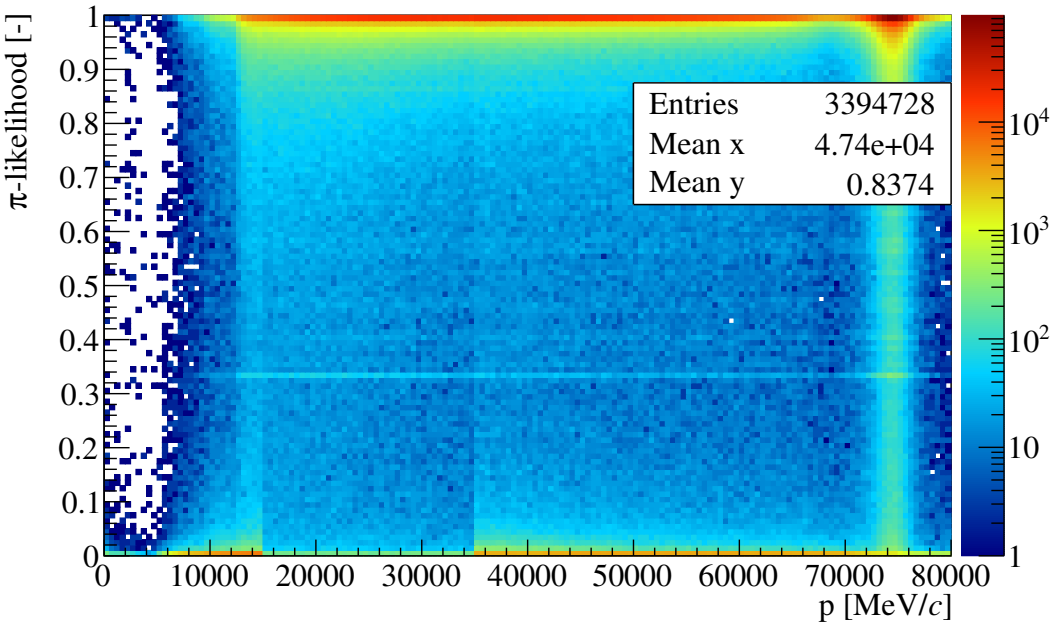

Figure 9.3: Probability that the track is π with respect to its momentum.

9.1.2 Matching with K^+

The GTK candidates first need to be matched with KTAG candidates[1], which is based on a time cut $|dt| < 0.6$ ns (for the time distribution between GTK and kaon tagged KTAG candidates see figure 9.4).

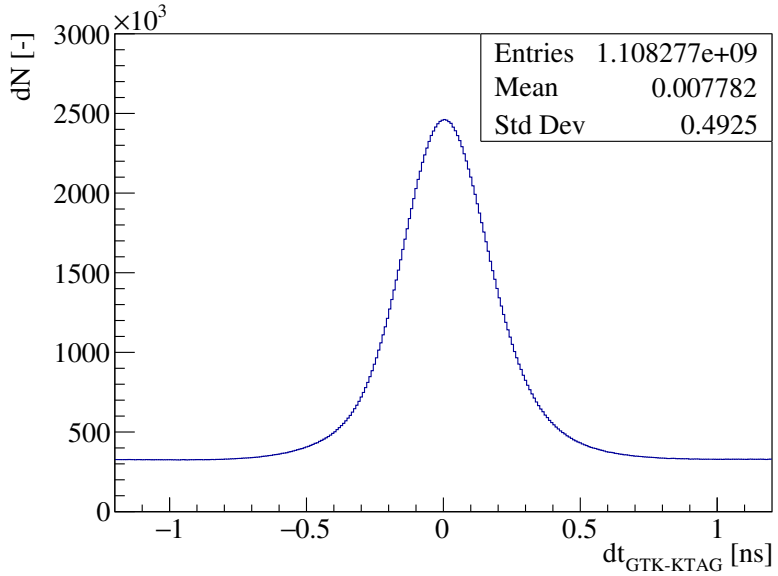

Figure 9.4: Time difference between GTK and KTAG candidates.

In the next step, the selected upstream kaons are matched with the downstream track and the track with the minimum combined value of CDA and mutual

[1]KTAG candidate is considered to be kaon if there is a coincidence of at least 6 sectors.

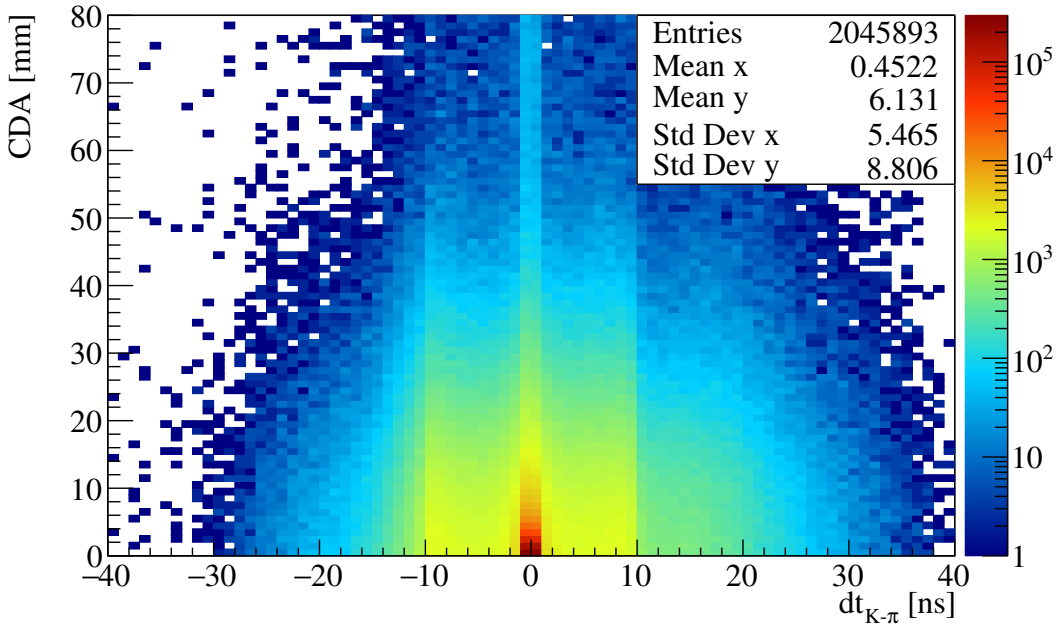

Figure 9.5: CDA and mutual time difference of matched upstream candidates with our selected π^+ downstream track.

time difference is selected. See the following figure 9.5 for the results of the matching. A cut for $|dt_{K-\pi}| < 1$ ns of matched K^+ and π^+ is further performed.

From the reconstructed set the events with K^+ decays in the fiducial region $105000 < z_{vtx} < 165000$ mm and $CDA < 15$ mm are selected.

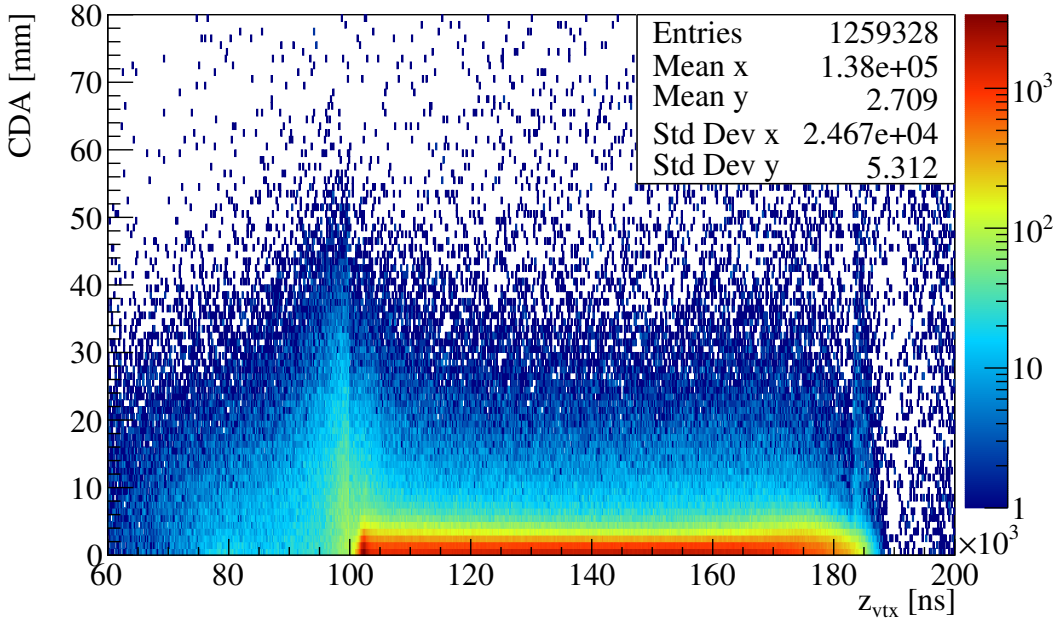

Figure 9.6: Z position of vertex and CDA of selected π^+ track for matched upstream K^+.

9.1.3 π^0 kinematic selection

From the four momenta of both K^+ and π^+, the missing invariant mass can be constructed as $(P_{K^+} - P_{\pi^+})^2 = m^2_{miss}$. As $m^2_{\pi^0} = (134.977)^2$ MeV$^2/c^4$, one can select the decay mode $K^+ \to \pi^+\pi^0$ by choosing $16000 < m^2_{miss} < 21000$ MeV$^2/c^4$, see figure 9.7.

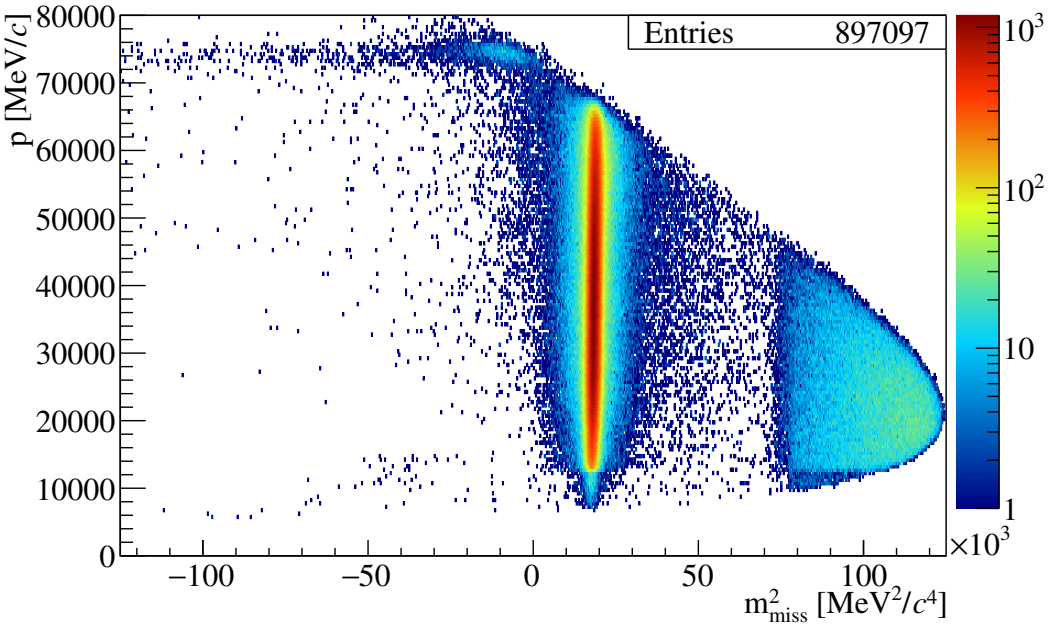

Figure 9.7: The missing invariant mass for π^0 of predicted momentum.

As can be seen in the figure 9.7, by this selection also the 75 GeV/c remnants of the beam as well as the products of the three-particle $K^+ \to \pi^+\pi^0\pi^0$ decay are cut off.

9.2 Study of photon clusters (run 8778)

The aim of this study is to cross-check the reconstruction of 2 photon clusters with a common vertex by reconstructing $\pi^0 \to \gamma\gamma$ decay from the known four-momenta $P_{\pi^0} = P_{\gamma 1} + P_{\gamma 2}$. Thus, at least three LKr clusters, where one belongs to the π^+ track, are required. A loop is performed over the rest, where maximum ± 1 ns time difference from π^+ is allowed, in order to select the photons.

By selecting one photon cluster and assigning its four-momentum $P_{\gamma 1}$, the 4-momentum of the searched second γ cluster $P_{\gamma 2} = P_{K^+} - P_{\pi^+} - P_{\gamma 1}$ can be constructed. As additional photons can be radiated in the decay via an internal bremsstrahlung, a selection of the corresponding clusters can occur instead of the $\pi^0 \to \gamma\gamma$ ones. But as $P^2_{\gamma 2} = m^2_{\gamma 2} = 0$ is expected, one can kinematically distinguish the correct photon cluster from the internal bremsstrahlung one, see figure 9.8.

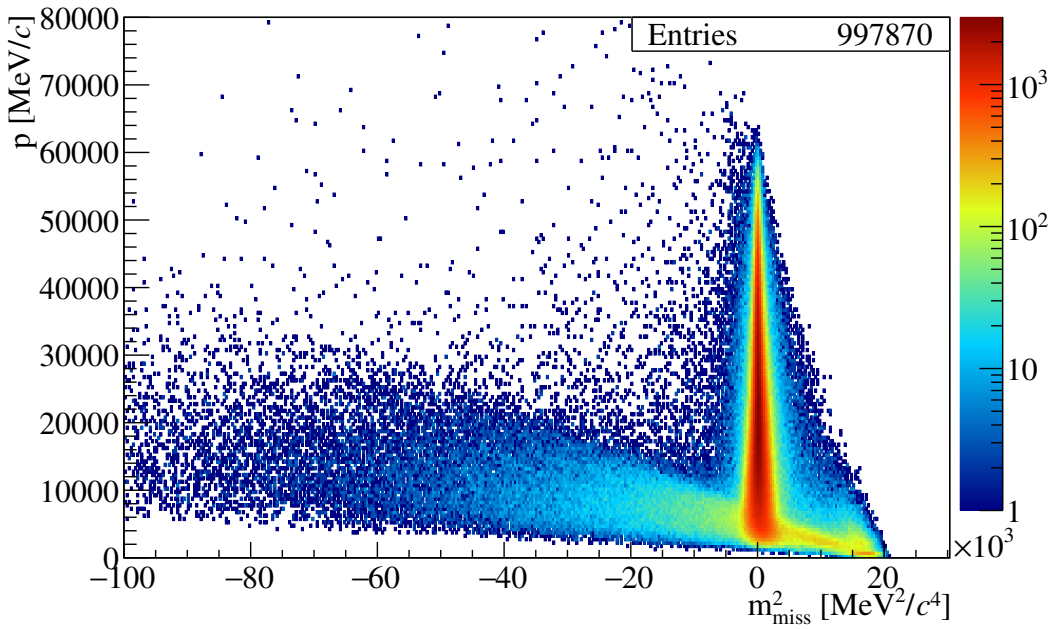

Figure 9.8: The missing invariant mass for searched photon of predicted momentum.

The low energy tail in the figure 9.8 can be further cleansed by a restriction on the distance of the second γ cluster from an expected position $d_{exp-clus} < 100$ mm, see figure 9.9.

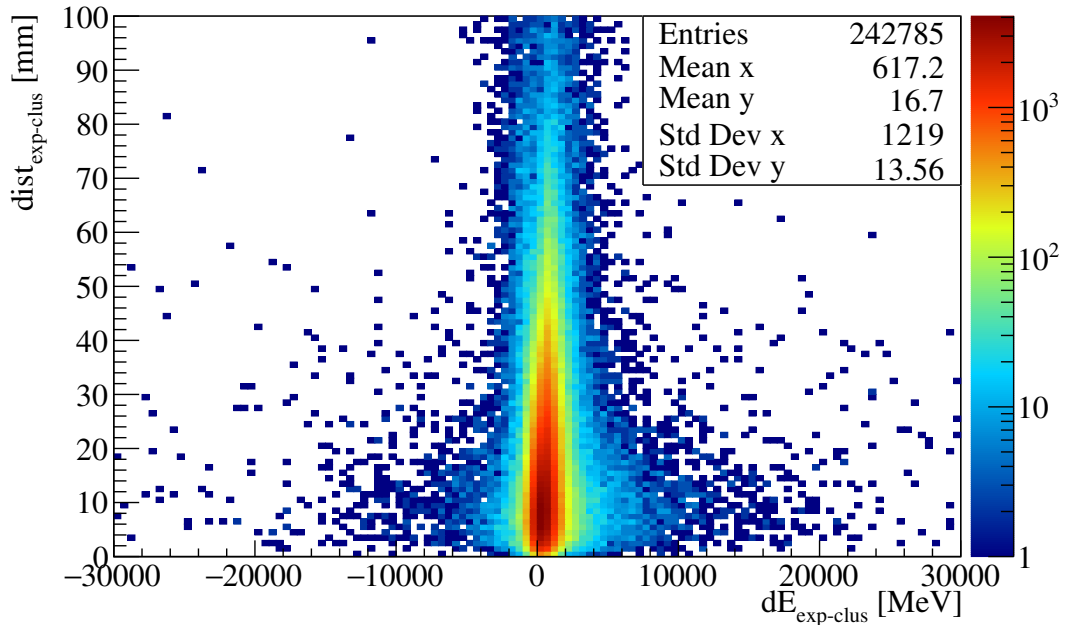

Figure 9.9: The difference between expected and reconstructed energy of the associated second photon cluster with respect to its distance from expected position.

The correctness of the reconstruction of photon energy is apparent from the x-axis of the figure 9.9 and the result is satisfactory if one takes into consideration

that the expected value was determined purely kinematically. Even if the cases $|dE| > 2$ GeV are suppressed by the order 10^{-3} with respect to the correct ones (see z-axis values for different x-axis ones in figure 9.9), a possibility of a systematic error has to be excluded. Thus, it has to be checked if the 'incorrect' energies are not fixed to some location at LKr. The position of the seed of the searched γ cluster weighted by the value $dE_{exp-clus}$ and normalized to the number of occurrences is depicted in the following figure 9.10.

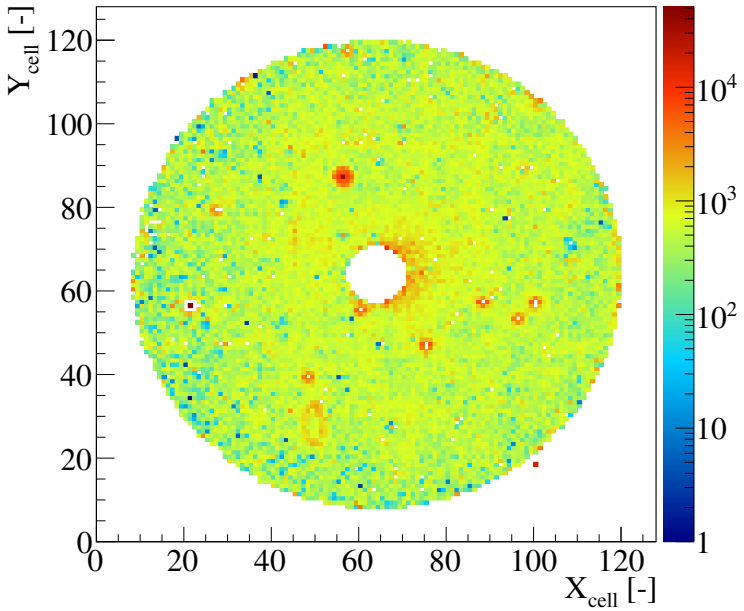

Figure 9.10: Position of the seed of the associated second photon cluster weighted by the difference of the reconstructed energy from the expected one (the z-axis of this figure corresponds to the x-axis of figure 9.9).

One can see a uniform distribution over the whole LKr, excluding some 'miscalibration' of specific channels with the only exception of seeds adjacent to the dead cells, which is due to an improper reconstruction of the cluster. Hence, a minimum distance of the seed of selected clusters of 20 mm will be required in the $ALP \to \gamma\gamma$ analysis discussed in the following chapter 10.

9.3 Event selection (run 8470)

The event selection for run 8470 follows the same prescription as is described for 8778 with the only difference of about nine times lower statistics. While the PID and upstream-downstream matching figures evince the expected behaviour consistent with 8778, the missing invariant mass figure 9.11 shows an incorrect π^0 reconstruction (splitting of the π^0 peak) and reveals some possible miscalibration of one of the detectors involved. This result together with a suspicious behaviour of runs 8477 and 8478 found in the previous chapter may indicate some deeper systematic error in the given data-taking period and demands a more thorough study.

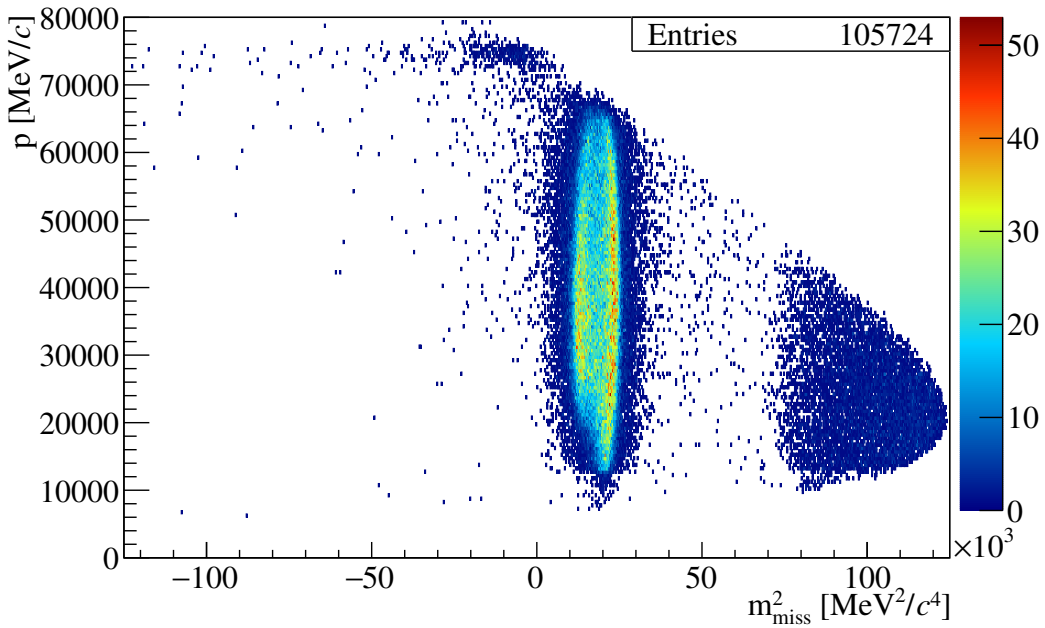

Figure 9.11: The missing invariant mass for π^0 of predicted momentum in run 8470.

10. Data analysis procedure

A strategy for the $ALP \to \gamma\gamma$ analysis will be outlined in this chapter with a discussion in the section 10.1 and a sample selection based on the findings from the previous chapters performed in the section 10.2.

10.1 Single event sensitivity

To avoid the observer bias a blind analysis technique is used for the study, where the signal region in the selected sample is kept blinded until the analysis of the selected sample and the background estimation are finished. In our specific case, the signal region is set by comparison of MC simulations of the $ALP \to \gamma\gamma$ mode and the background. As we are 'scanning' some region of the $(g_{a\gamma\gamma}, m_a)$ parameter space, we have to evaluate the signal with some fixed parameter and hence the position of the signal region depends on the parameter's value. The background on the other hand has a fixed shape given by known phenomena.

In the case of beam-dump mode, the background does not originate from some specific decay but as already discussed in chapter 8 it is generated by interactions of the muon halo in the material of the detector. This in our case means a continuous spectrum of photons mostly generated by bremsstrahlung. For this reason the background estimation in the beam-dump mode becomes quite challenging as one has to consider all possible targets for the muon halo. The MC simulations were beyond the reach of this thesis[1] but examples of dominant targets were shown in the figure 8.4 from the study of e^+e^- pairs.

The position of the signal region is limited by the signal acceptance on one side and by the background contamination on the other side, which determines the region where the apparatus is sensitive towards the searched decay. The single event sensitivity (SES) can be evaluated as

$$SES = \frac{1}{N_{POT} \cdot A_{signal} \cdot \epsilon_{RV} \cdot \epsilon_{trigger}}, \tag{10.1}$$

where N_{POT} is the number of protons on target, $\epsilon_{trigger}$ is the already discussed trigger efficiency, A_{signal} is the signal acceptance as given by the MC simulation for the selected signal region and ϵ_{RV} is the random veto efficiency[2].

10.2 (Inverted) sample selection

Keeping in mind the possible corruption of the trigger information rendered by the L0TP, L0 trigger primitives will be asked for instead of the trigger word to reach the full possible trigger efficiency. To select a neutral event, we require

[1] Preliminary MC simulations for given set of parameters fixing the signal region were presented in section 7.2 proceeding from [55], while background MC simulations are ongoing.

[2] By random veto efficiency we mean the probability that the searched event is not lost due to an accompanying background (e.g. signal in LAV from a passing muon). The value has to be independently measured on the data as it is not easy to be simulated on MC.

the Control primitive in any trigger slot and no Physics primitive. The following selection conditions for the sample were established:

- no charged tracks downstream;
- exactly two LKr clusters;
- minimum distance of clusters from the beampipe and the edge (cluster location d_{clus} within 150 mm $< d_{clus} <$ 1130 mm);
- distance from dead cells $>$ 20 mm;
- no in-time association of clusters with signals in MUV1, MUV3, SAV, CHOD, RICH and 'downstream' LAV stations (LAVID $>$ 8);
- mutual distance of clusters $>$ 100 mm to avoid overlap of showers;
- no in-time association of clusters with CHANTI and 'upstream' LAVs (1-8).

These conditions eliminate almost all statistics and hence are not suitable for the background estimation and comparison with MC. However, due to the L0TP defect, no charged particle can be allowed in the acceptance of downstream detectors as one would risk the loss of accompanying neutral event. A compromise between these two is an inversion of the last condition from the list. By allowing a signal in the CHANTI or upstream LAVs, one increases the background statistics and yet cuts off the charged particles entering the 'downstream' area. Such selected sample will be referred as an *inverted sample*.

As a relative stability of runs 8762-8774 was validated in previous chapters, the 'inverted sample' will be selected from these by applying the above conditions following the same order of cuts. The full statistics can be seen in the figure 10.1 as well as the values entering the first cut condition requiring 0 charged tracks.

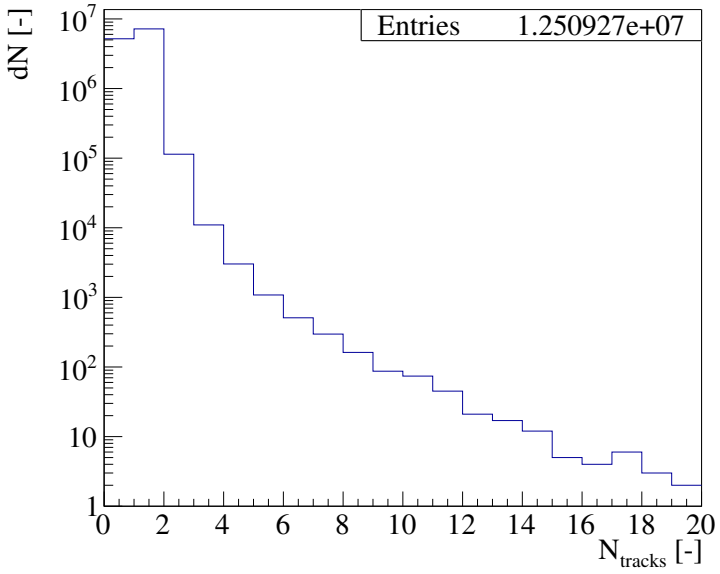

Figure 10.1: Number of charged tracks in the 'Control triggered' sample.

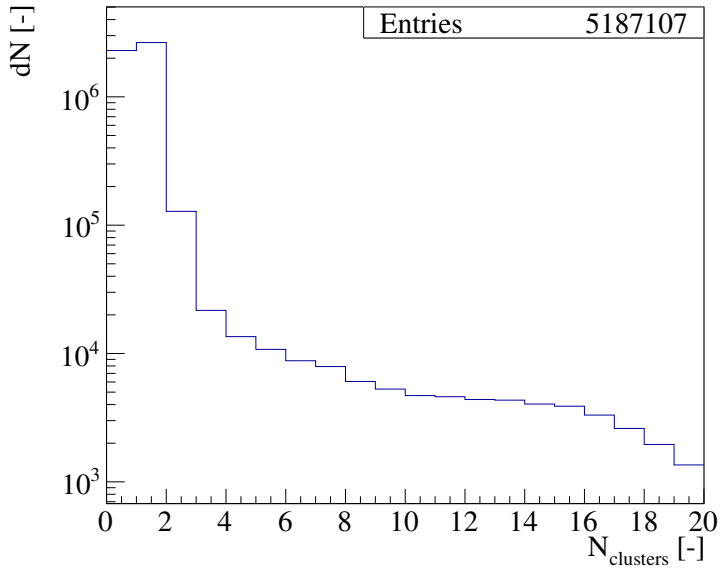

Figure 10.2: Number of LKr clusters for events with no reconstructed charged tracks.

Next, strictly two LKr clusters are asked for, which reduces the statistics about five times (compare figures 10.2 and 10.3) and cuts on the distance of clusters from the beampipe, the edges and dead cells are performed (compare figures 10.3 and 10.4). The geometry cut results in another reduction of factor 5 due to a noisy channel at the edge of LKr (10.3).

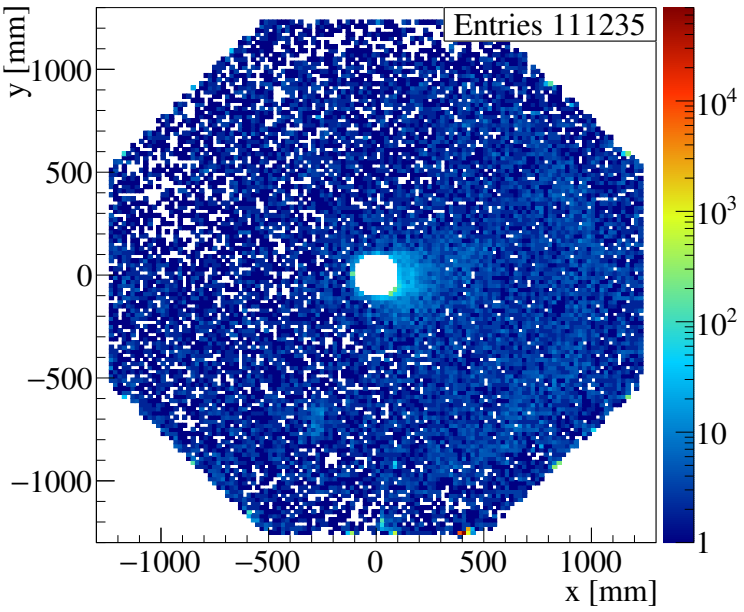

Figure 10.3: Position of LKr clusters for events with exaclty two clusters.

A series of time cuts on the association with a signal from detectors used as a veto reduces the statistics significantly (compare figures 10.4 and 10.8). Cut on signals within 10 ns in CHOD and MUV1 is applied, 5 ns in MUV3,

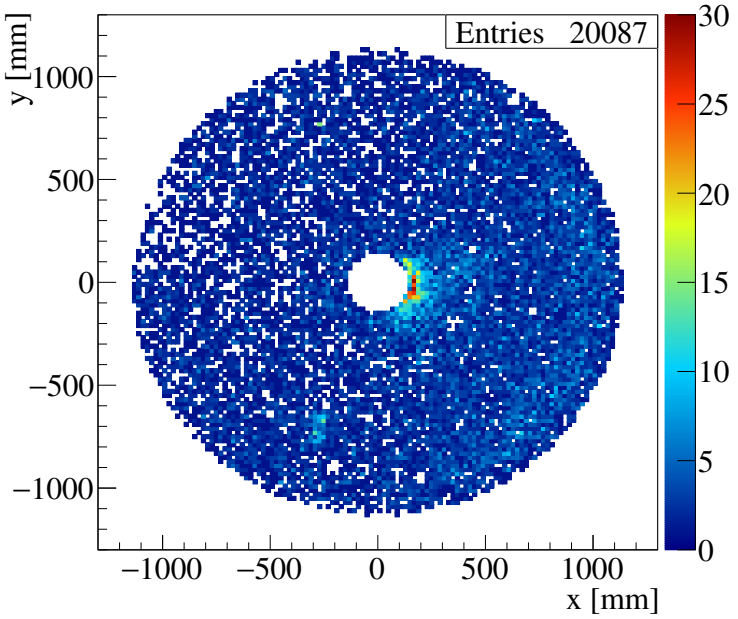

Figure 10.4: Position of LKr clusters after applying 'position cuts'.

SAV and downstream LAVs and 2 ns cut for RICH, see figures 10.5 10.6 for the corresponding distributions. The cut values were estimated from the shapes of these distributions but a more efficient selection might be achieved by using MVA techniques instead, which is worthy to be tested in the future on MC samples.

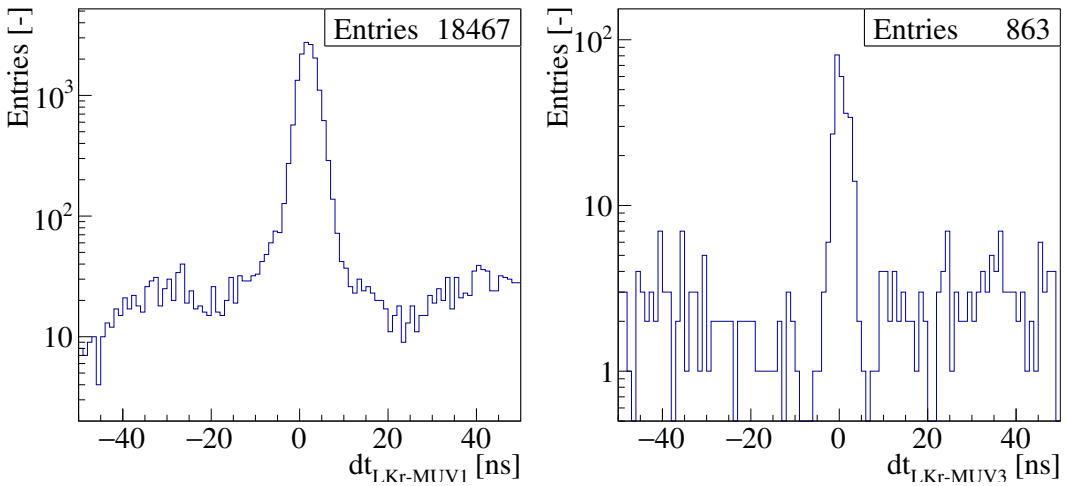

Figure 10.5: Mutual time difference between LKr and MUV1 (left) and LKr and MUV3 (right) with respect to the number of candidates in given detector.

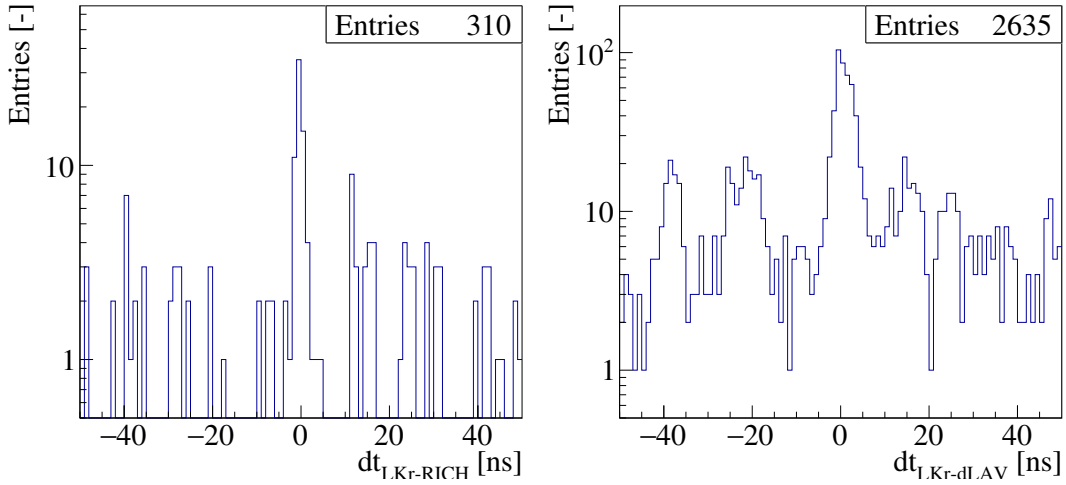

Figure 10.6: Mutual time difference between LKr and RICH (left) and LKr and downstream LAV stations (right) with respect to the number of candidates in given detector.

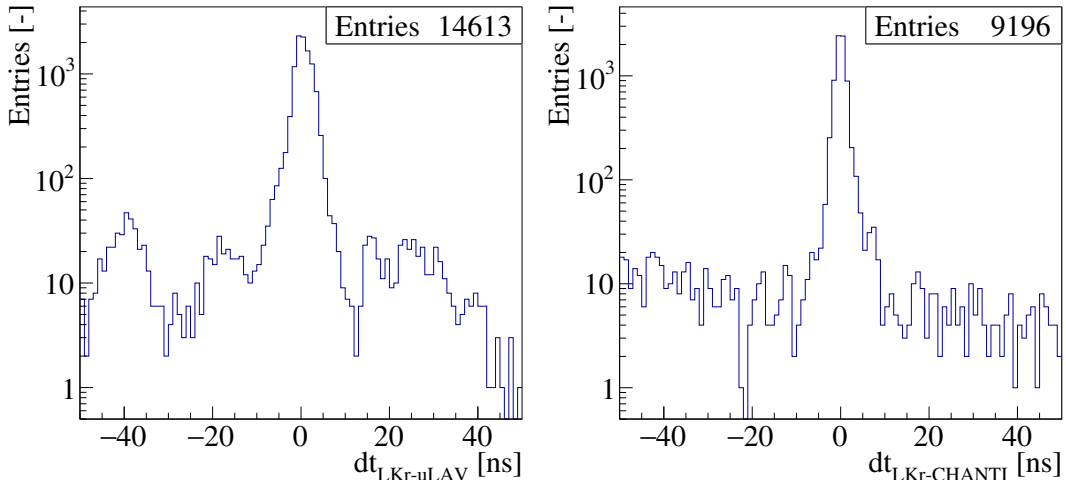

Figure 10.7: Mutual time difference between LKr and upstream LAV stations (left) and LKr and CHANTI (right) with respect to the number of candidates in given detector used for in-time selection (condition inversion).

The last inverted condition is applied as an in-time candidate ($|dt| < 10$ ns) in CHANTI or any upstream LAV station (see figure 10.7).

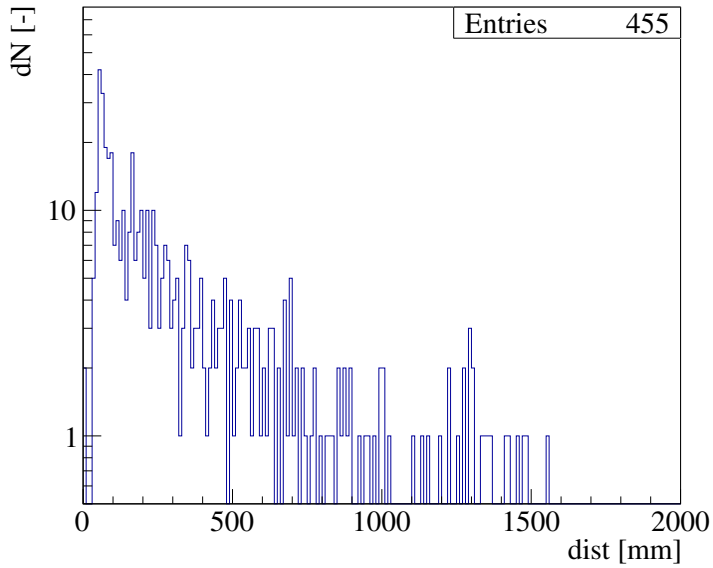

Figure 10.8: Mutual distance of two selected clusters.

The last cut performed is for the mutual distance of both clusters d_{12}. For the resulting final energy distribution of the inverted sample, see figure 10.9.

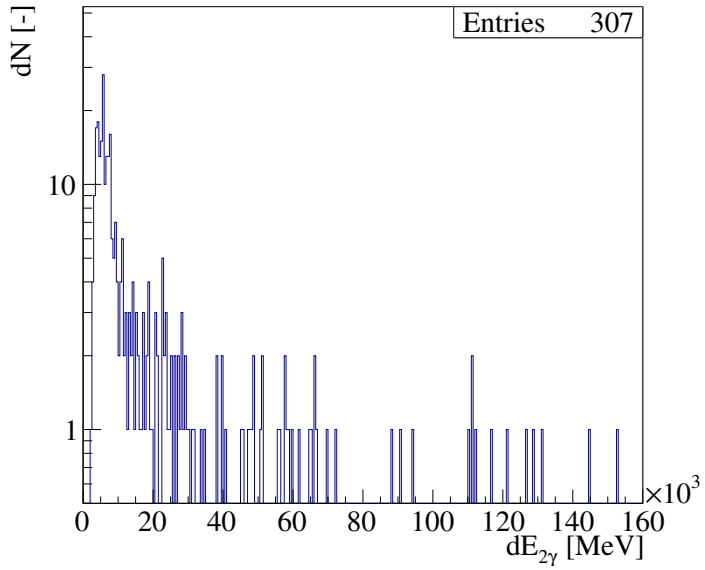

Figure 10.9: The combined energy ($E = E_{\gamma 1} + E_{\gamma 2}$) distribution in the inverted sample.

From the reconstructed photon cluster energies, the invariant mass of the original decaying particle can be simply derived from the angle θ under which the photons are radiated. For given position of the vertex z_{vtx} (or distance L of the vertex from the detector $z_{vtx} = z_{LKr} - L$), we get

$$m_a = \sqrt{2E_{\gamma 1}E_{\gamma 2}(1-\cos\theta)} = 2\sqrt{E_{\gamma 1}E_{\gamma 2}}\sin\frac{\theta}{2} \approx \frac{\sqrt{E_{\gamma 1}E_{\gamma 2}}d_{12}}{L}. \qquad (10.2)$$

Conclusion

In the course of the study of the trigger efficiency for beam-dump data gathered during 2016-2018 data-taking period using e^+e^- pairs, a significant inefficiency was observed. Performed comparison of gathered data with the primitive dump has pointed to a malfunction of the level zero trigger processor firmware. With better understanding of the issue, we were able to map the consequences, among which is a loss of data, which was determined to be around 57.7%, effectively reducing the number of gathered data for $ALP \to \gamma\gamma$ analysis to $1.13 \cdot 10^{16}$ PoT.

Apart from the data loss, the trigger efficiency was proven to be standard (reaching 100% within the standard deviation) when different trigger variables are used. The trigger efficiency study has also revealed a different behaviour (with respect to the expected effect of the L0TP defect) of two statistically significant runs 8477 and 8478 (together statistics of $3.85 \cdot 10^{15}$ PoT) and runs 8278 and 8280 with lower statistics (together $0.41 \cdot 10^{15}$ PoT).

Further, a $K^+ \to \pi^+\pi^0$ analysis was performed on 'kaon runs' 8778 (resp. 8470), which are close in time to a beam-dump sample 8762-8774 (resp. 8477-8478), in order to test the data quality of runs from given time periods. By selecting the $\pi^0 \to \gamma\gamma$ mode, we were able to test the detector behaviour with a high intense flux of photon pairs, which is useful for $ALP \to \gamma\gamma$ studies performed in a mode with much lower statistics. The study of the run 8778 has manifest a correct reconstruction of photon clusters, which supports the idea that runs 8762-8774 were stable, as was observed during the trigger efficiency study. The study of the run 8470, on the other hand, has proven some miscalibration during the corresponding data-taking period and has to be investigated further.

Following the facts revealed in the preceding, a strategy for the search for $ALP \to \gamma\gamma$ has been determined. An analysis on the 'stable' sample 8762-8774 was performed with inverted conditions on the upstream veto detectors in order to see the 'background sample', which is to be compared with the MC simulations in the future.

Bibliography

[1] J. Jerhot. Study of rare decays at NA62 experiment in CERN. *Bachelor thesis*, 2017.

[2] R. Brun and F. Rademakers. ROOT: An object oriented data analysis framework. *Nuclear Instruments and Methods in Physics Research Section A*, 389(1-2), 11 April 1997. Available from: `https://doi.org/10.1016/S0168-9002(97)00048-X`.

[3] NA62 Collaboration. NA62 Framework. Available from: `https://na62-sw.web.cern.ch/doxygen`.

[4] A. Hoecker, P. Speckmayer, J. Stelzer, J. Therhaag, E. von Toerne, and H. Voss. TMVA: Toolkit for Multivariate Data Analysis. *Proceedings of Science*, Advanced Computing and Analysis Techniques, 4 May 2007. Available from: arXiv:physics/0703039[physics.data-an].

[5] H. Georgi. *Lie Algebras In Particle Physics: from Isospin To Unified Theories*. 2nd edition. Westview Press, 1999. ISBN: 978-0738202334.

[6] J. Hořejší. *Fundamentals of Electroweak Theory*. Karolinum, 2003. ISBN: 978-8024606392.

[7] M.D. Schwartz. *Quantum Field Theory and the Standard Model*. 1st edition. Cambridge University Press, 2013. ISBN: 978-1107034730.

[8] S. Pokorski. *Gauge Field Theories*. 2nd edition. Cambridge University Press, 2000. ISBN: 978-0521478168.

[9] J. Novotný. Lectures on *Theory of Gauge Fields*, 2018. Charles University in Prague.

[10] V.I. Arnold. *Mathematical Methods of Classical Mechanics*. 2nd edition. Springer, 1997. ISBN: 978-0387968902.

[11] A. Das. *Lectures on Quantum Field Theory*. 1st edition. World Scientific, 2008. ISBN: 978-9812832856.

[12] J. Hořejší. Lectures on *Quantum Field Theory III*, 2018. Charles University in Prague.

[13] C. Stover. Wolfram Mathworld: *Gell-Mann Matrix*. Available from: `http://mathworld.wolfram.com/Gell-MannMatrix.html`.

[14] M. Tanabashi, *et al.* (Particle Data Group). Review of particle physics. *Phys. Rev. D*, 98, 2018. Available from: arXiv:hep-ph/0607268.

[15] A. Deur, S. J. Brodsky, and G. F. de Teramond. The QCD Running Coupling. *Prog.Part.Nucl.Phys.*, 90, 2016. Available from: arXiv:1604.08082[hep-ph].

[16] S. Scherer and M. R. Schindler. *A Primer for Chiral Perturbation Theory.* 1st edition. Springer, 2012. ISBN: 978-3642192531.

[17] J. Goldstone, A. Salam, and S. Weinberg. Broken Symmetries. *Physical Review*, 127(3), 1 August 1962. Available from: https://doi.org/10.1103/PhysRev.127.965.

[18] T. Schäfer and E. V. Shuryak. Instantons in QCD. *Reviews of Modern Physics*, 70(2), 1 April 1998. Available from: arXiv:hep-ph/9610451.

[19] R. D. Peccei. The Strong ***CP*** problem and axions. *Lect. Notes Phys.*, 741:3–17, July 2006. Available from: arXiv:hep-ph/0607268.

[20] R. D. Peccei and Helen R. Quinn. ***CP*** Conservation in the Presence of Pseudoparticles. *Phys. Rev. Lett.*, 38(25):1440–1443, June 1977. Available from: https://link.aps.org/doi/10.1103/PhysRevLett.38.1440.

[21] S. Weinberg. A new light boson? *Phys. Rev. Lett.*, 40(4), 1978. Available from: https://journals.aps.org/prl/abstract/10.1103/PhysRevLett.40.223.

[22] F. Wilczek. Problem of Strong ***P*** and ***T*** Invariance in the Presence of Instantons. *Phys. Rev. Lett.*, 40(5), 1978. Available from: https://journals.aps.org/prl/abstract/10.1103/PhysRevLett.40.279.

[23] M. Kuster, G. Raffelt, and B. Beltrán. *Axions.* Springer, 2008. ISBN: 978-3540735175.

[24] C. Vafa and E. Witten. Restrictions on symmetry breaking in vector-like gauge theories. *Nuclear Physics B*, 234(1), 1984. Available from: https://doi.org/10.1016/0550-3213(84)90230-X.

[25] G.G. di Cortona, E. Hardy, J.P. Vega, and G. Villadoro. The QCD axion, precisely. *Journal of High Energy Physics*, 1601(34), 2016. Available from: arXiv:1511.02867[hep-ph].

[26] S. Borsanyi, Z. Fodor, J. Guenther, K.-H. Kampert, S. D. Katz, T. Kawanai, T. G. Kovacs, S. W. Mages, A. Pasztor, F. Pittler, J. Redondo, A. Ringwald, and K. K. Szabo. Calculation of the axion mass based on high-temperature lattice quantum chromodynamics. *Nature*, 539(7627), 2016. Available from: https://www.nature.com/articles/nature20115.

[27] R. D. Peccei and Helen R. Quinn. Constraints imposed by ***CP*** conservation in the presence of pseudoparticles. *Phys. Rev. D*, 16(6), September 1977. Available from: https://journals.aps.org/prd/abstract/10.1103/PhysRevD.16.1791.

[28] J. E. Kim. Weak-Interaction Singlet and Strong ***CP*** Invariance. *Physical Review Letters*, 43(2), 9 July 1979. Available from: https://doi.org/10.1103/PhysRevLett.43.103.

[29] M. A. Shifman, A. I. Vainschtein, and V. I. Zakharov. Can confinement ensure natural ***CP*** invariance of strong interactions? *Nuclear Physics B*, 166(3), 28 April 1980. Available from: https://doi.org/10.1016/0550-3213(80)90209-6.

[30] M. Dine, W. Fischler, and M. Srednicki. A simple solution to the strong ***CP*** problem with a harmless axion. *Physics Letters B*, 104(3), 27 August 1981. Available from: https://doi.org/10.1016/0370-2693(81)90590-6.

[31] A. R. Zhitnitsky. On Possible Suppression of the Axion Hadron Interactions. *Soviet Journal of Nuclear Physics*, 31(260), 1980.

[32] Y. Chikashige, R. N. Mohapatra, and R. D. Peccei. Are there real goldstone bosons associated with broken lepton number? *Physics Letters B*, 98(4), 1981. Available from: https://doi.org/10.1016/0370-2693(81)90011-3.

[33] F. Wilczek. Axions and Family Symmetry Breaking. *Physical Review Letters*, 49(21), 1982. Available from: https://doi.org/10.1103/PhysRevLett.49.1549.

[34] R. Coquereaux and G. Esposito-Farese. The theory of Kaluza-Klein-Jordan-Thiry revisited. *Annales de l'I.H.P. Physique théorique*, 52(2), 1990. Available from: http://www.numdam.org/item/?id=AIHPA_1990__52_2_113_0.

[35] N. Arkani-Hamed, S. Dimopoulos, and G. Dvali. The hierarchy problem and new dimensions at a millimeter. *Physics Letters B*, 429(3-4), 18 June 1998. Available from: arXiv:hep-ph/9803315.

[36] K. R. Dienes, E. Dudas, and T. Tony Gherghetta. Invisible axions and large-radius compactifications. *Physical Review D*, 62(10), 15 November 2000. Available from: arXiv:hep-ph/9912455.

[37] E. Witten. Search for a realistic Kaluza-Klein theory. *Nuclear Physics B*, 186(3), 10 August 1981. Available from: https://doi.org/10.1016/0550-3213(81)90021-3.

[38] Edward Witten Peter Svrcek. Axions In String Theory. *Journal of High Energy Physics*, 2006(6), 26 June 2006. Available from: arXiv:hep-th/0605206.

[39] A. Arvanitaki, S. Dimopoulos, S. Dubovsky, N. Kaloper, and J. March-Russell. String axiverse. *Physical Review D*, 81(12), 28 June 2010. Available from: arXiv:0905.4720[hep-th].

[40] D. J. E. Marsh. Axion Cosmology. *Physics Reports*, 643, 1 July 2016. Available from: arXiv:1510.07633[astro-ph.CO].

[41] M. Kawasaki and K. Nakayama. Axions: Theory and Cosmological Role. *Annual Review of Nuclear and Particle Science*, 63(1), 2013. Available from: arXiv:1301.1123[hep-th].

[42] I. G. Irastorza and J. Redondo. New experimental approaches in the search for axion-like particles. *Progress in Particle and Nuclear Physics*, 102, 19 June 2018. Available from: arXiv:1801.08127[hep-ex].

[43] J. I. Read. The local dark matter density. *Journal of Physics G: Nuclear and Particle Physics*, 41, 12 May 2014. Available from: arXiv:1404.1938[astro-ph.GA].

[44] P. Sikivie. Experimental Tests of the "Invisible" Axion. *Physical Review Letters*, 51(16), 17 October 1983. Available from: `https://doi.org/10.1103/PhysRevLett.51.1415`.

[45] G. Rybka, *et al.* (ADMX Collaboration). Direct detection searches for axion dark matter. *Physics of the Dark Universe*, 4, 2014. Available from: `https://www.sciencedirect.com/science/article/pii/S2212686414000156?via%3Dihub`.

[46] S. Andriamonje, *et al.* (CAST Collaboration). An improved limit on the axion–photon coupling from the CAST experiment. *Journal of Cosmology and Astroparticle Physics*, 2007, 2007. Available from: arXiv:hep-ex/0702006.

[47] M. Arik, *et al.* (CAST Collaboration). Search for Solar Axions by the CERN Axion Solar Telescope with ^{3}**He** Buffer Gas: Closing the Hot Dark Matter Gap. *Physical Review Letters*, 112(9), 4 March 2014. Available from: arXiv:1307.1985[hep-ex].

[48] V. Anastassopoulos, *et al.* (CAST Collaboration). New experimental approaches in the search for axion-like particles. *Nature Physics*, 13, 2017. Available from: arXiv:1705.02290[hep-ex].

[49] E. Armengaud, *et al.* (IAXO Collaboration). Conceptual design of the International Axion Observatory (IAXO). *Journal of Instrumentation*, 9(T05002), 12 May 2014. Available from: arXiv:1401.3233[physics.ins-det].

[50] G. Mueller, P. Sikivie, D.B. Tanner, and K van Bibber. Detailed design of a resonantly-enhanced axion-photon regeneration experiment. *Physical Review D*, 80(7), 15 October 2009. Available from: arXiv:0907.5387[hep-ex].

[51] R. Ballou, *et al.* (OSQAR Collaboration). New exclusion limits on scalar and pseudoscalar axionlike particles from light shining through a wall. *Physical Review D*, 92(9), 1 November 2015. Available from: arXiv:1506.08082[hep-ex].

[52] R. Bähre, B. Döbrich, J. Dreyling-Eschweiler, S. Ghazaryan, R. Hodajerdi, D. Horns, F. Januschek, E. Knabbe, E.-A. Lindner, D. Notz, A. Ringwald, J. E. von Seggern, R. Stromhagen, D. Trines, and B. Willke. Any Light Particle Search II - Technical Design Report. *Journal of Instrumentation*, 8(T09001), 5 September 2013. Available from: arXiv:1302.5647[physics.ins-det].

[53] M. Bregant, *et al.* (PVLAS Collaboration). New PVLAS results and limits on magnetically induced optical rotation and ellipticity in vacuum. *Physical Review D*, 77(3), 1 February 2008. Available from: arXiv:0706.3419[hep-ex].

[54] A. A. Geraci, *et al.* (ARIADNE Collaboration). Progress on the ARIADNE Axion Experiment. *Springer Proceedings in Physics*, 211, 2018. Available from: arXiv:1710.05413[astro-ph.IM].

[55] B. Döbrich, J. Jaeckel, F. Kahlhoefer, A. Ringwald, and K. Schmidt-Hoberg. ALPtraum: ALP production in proton beam dump experiments. *Journal of High Energy Physics*, 2016(2), 2 February 2016. Available from: arXiv:1512.03069[hep-ph].

[56] H Primakoff. Photo-Production of Neutral Mesons in Nuclear Electric Fields and the Mean Life of the Neutral Meson. *Physical Review*, 81(5), 1 March 1951. Available from: https://doi.org/10.1103/PhysRev.81.899.

[57] S., *et al.* (SHiP Collaboration) Alekhin. A facility to Search for Hidden Particles at the CERN SPS: the SHiP physics case. *Reports on Progress in Physics*, 79(12), 24 October 2016. Available from: arXiv:1504.04855[hep-ph].

[58] B. Döbrich, J. Jaeckel, and T. Spadaro. Light in the beam dump - ALP production from decay photons in proton beam-dumps. 3 April 2019. Available from: arXiv:1904.02091[hep-ph].

[59] CERN. The accelerator complex, [Accessed 1 March 2019]. Available from: https://home.cern/science/accelerators/accelerator-complex.

[60] B. Bloch-Devaux, *et al.* (NA62 Collaboration). The Beam and detector of the NA62 experiment at CERN. 2017. Available from: arXiv:1703.08501[physics.ins-det].

[61] E. Cortina Gil, *et al.* (NA62 Collaboration). First search for $K^+ \to \pi^+\nu\bar{\nu}$ using the decay-in-flight technique. *Physics Letters B*, 23 February 2019. Available from: arXiv:1811.08508[hep-ex].

[62] NA62 Collaboration. *GTK - Technical design*, December 2010. Available from: https://na62.web.cern.ch/na62/Documents/Chapter_GTK_extract_full_doc_v10.pdf.

[63] NA62 Collaboration. *CHANTI - Technical design*, December 2010. Available from: https://na62.web.cern.ch/na62/Documents/Chapter_Chanti_extract_full_doc_v10.pdf.

[64] NA62 Collaboration. *Photon veto - Technical design*, December 2010. Available from: https://na62.web.cern.ch/na62/Documents/Chapter_PhotonVeto_extract_full_doc_v10.pdf.

[65] NA62 Collaboration. *Straw Tracker - Technical design*, December 2010. Available from: https://na62.web.cern.ch/na62/Documents/Chapter_StrawTracker_extract_full_doc_v10t.pdf.

[66] NA62 Collaboration. *The RICH - Technical design*, December 2010. Available from: https://na62.web.cern.ch/na62/Documents/Chapter_RICH_extract_full_doc_v10.pdf.

[67] S. Kholodenko. NA62 Charged Particle Hodoscope. Design and performance in 2016 run. *Journal of Instrumentation*, 12, 27 June 2017. Available from: arXiv:1705.05093[physics.ins-det].

[68] S. Chiozzi and D. Soldi. Level Zero Trigger Processor for the NA62 experiment. *Journal of Instrumentation*, 13, 2 May 2018. Available from: arXiv:1802.06548[physics.ins-det].

[69] D. Soldi. The FPGA-based first level trigger for the NA62 Experiment at CERN SPS. *Dissertation thesis*, 2017.

[70] G. Unal. Reconstruction program for the LKr. *NA62 Internal Note*, (NA62-15-02).

[71] A. Sturgess. Tracking optimisation and the measurement of $K^+ \to \pi^+\mu^+\mu^-$ at NA62. *Dissertation thesis*, 2018.

[72] M. Zamkovsky. private communication, April 2019.

[73] T. Spadaro and B. Döbrich. private communication, March 2019.

[74] B. Döbrich. private communication, September 2018.

[75] M. Koval. private communication, September 2018.

[76] T. Spadaro. private communication, December 2018.

[77] D. Soldi. private communication, January 2019.

[78] R. Aliberti. Particle Identification with Calorimeters for the Measurement of the Rare Decay $K^+ \to \pi^+\nu\bar{\nu}$ at NA62. *Dissertation thesis*, 2019.

List of Abbreviations

QCD - Quantum chromodynamics
ALP - Axion-like particle
SM - Standard Model
BD - Beam-dump
MC - Monte Carlo
CERN - Conseil Européen pour la Recherche Nucléaire
NA62FW - NA62 Framework
TMVA - Toolkit for Multivariate Data Analysis
SSB - Spontaneous symmetry breaking
QED - Quantum electrodynamics
BRST - Becchi-Rouet-Stora-Tyutin
MS - Minimal subtraction
PQ - Peccei-Quinn
χPT - Chiral perturbation theory
PQWW - Peccei-Quinn-Weinberg-Wilczek
DM - Dark matter
KSVZ - Kim-Shifman-Vainshtein-Zakharov
DFSZ - Dine-Fischler-Srednicki-Zhitnisky
KK - Kaluza-Klein
BBN - Big Bang Nucleosynthesis
CMB - Cosmic Microwave Background
EBL - Extragalactic Background Light
CAST - CERN Axion Solar Telescope
LSW - Light-shining through wall
PSB - Proton Synchrotron Booster
PS - Proton Synchrotron
SPS - Super Proton Synchrotron
LHC - Large Hadron Collider
TAX - Target Attenuator eXperimental areas
KTAG - Kaon tagger
GTK - GigaTracker
TDC - Time-to-Digital Converter
CHANTI - The Charged Anti-Coincidence Detector
LAV - Large Angle Veto
RICH - Ring Imaging Cherenkov Counter
CHOD - Charged Hodoscope
WLS - Wavelength Shifting
LKr - Liquid Krypton
MUV - Muon Veto
SAV - Small Angle Veto
SAC - Small Angle Calorimeter
IRC - Intermediate Ring Calorimeter
HASC - Hadronic Sampling Calorimeter
PoT - Protons on Target
TDAQ - Trigger and Data Acquisition
L0TP - Level Zero Trigger Processor

CDR - Central Data Recording
TTC - Timing, Trigger and Control
SOB - Start of Burst
EOB - End of Burst
FADC - Flash Analog-to-Digital Converter
FPGA - Field-Programmable Gate Array
HPTDC - High-Performance Time-to-Digital Converter
GTK-RO - GTK off-detector Readout
SRB - Straw Readout Board
CREAM - Calorimeter Readout Module
MMU - Memory Management Unit
FIFO - First-In-First-Out
CDA - Closest Distance-of-Approach
MIP - Minimum Ionizing Particle
PID - Particle Identification
BDT - Boosted Decision Trees
SES - Single Event Sensitivity